TECHNICAL REPORT STANDARD TITLE PAGE

1. Report No.	2. Government Accession No.	3. Recipient's Catalog No.
FHWA/TX-91+1123-6		

4. Title and Subtitle
EFFECT OF FINITE WIDTH ON DYNAMIC DEFLECTIONS OF PAVEMENTS

5. Report Date
January 1991

6. Performing Organization Code

7. Author(s)
Yumin Vincent Kang, Jose M. Roesset, and Kenneth H. Stokoe, II

8. Performing Organization Report No.
Research Report 1123-6

9. Performing Organization Name and Address
Center for Transportation Research
The University of Texas at Austin
Austin, Texas 78712-1075

10. Work Unit No.

11. Contract or Grant No.
Rsch. Study 2/3-18-87/9-1123

13. Type of Report and Period Covered
Interim

12. Sponsoring Agency Name and Address
Texas State Department of Highways and Public Transportation; Transportation Planning Division
P. O. Box 5051
Austin, Texas 78763-5051

14. Sponsoring Agency Code

15. Supplementary Notes
Study conducted in cooperation with the U. S. Department of Transportation, Federal Highway Administration. Research Study Title: "Non-Destructive Test Procedures for Analyzing the Structural Conditions of Pavements"

16. Abstract

A highway has a finite width in its transverse direction, and the existence of variation in material properties between the road and the surrounding soil is not uncommon. A three-dimensional elastodynamic solution is presented to take into account the variation of material properties in the soil-pavement system by using the Fourier superposition technique. The pavement, base and subgrade are represented by a finite-element core region. An expansion technique is used to simulate the infinite lateral soil region. A viscous boundary is implemented for a half space condition. The stiffness matrices and point load and disk load vectors are obtained in the frequency-wavenumber domain. Parametric studies of the soil-pavement formulation are conducted to assess the accuracy of the results. An investigation of the effects of the lateral boundary on the pavement deflections measured by various nondestructive testing techniques is presented. The Dynaflect, the Falling Weight Deflectometer (FWD), and the Spectral-Analysis-of-Surface-Waves (SASW) methods are simulated on three typical in-service pavement sections. The results of the Dynaflect tests indicate that the effects of the lateral boundary on the measured deflections are directly related to: (a) the loading position with respect to the edge of the pavement; (b) the thickness of the surface layer; (c) the lateral stiffness contrast between the road and the surrounding soil; (d) the height of the ramp, if the test is performed on a ramp. A closer loading position, a larger value of the thickness, a higher contrast, and a larger value of the ramp height will result in a larger influence on the deflections. The lateral boundary also has a differential influence on different stations which will, in turn, change the shape of the deflection basins. The existence of retaining walls is important, especially for the "high" ramp. Similar conclusions are reached for the FWD test simulations. The results of the SASW tests indicate that some fluctuations may occur in the dispersion curve because of the reflected body waves due to the abrupt change in the stiffness at the horizontal interfaces between layers. The existence of the lateral boundary causes additional fluctuations, particularly for long wavelengths.

17. Key Words	18. Distribution Statement
finite width pavements, Dynaflect, Falling Weight Deflectometer, Spectral Analysis of Surface Waves, finite elements, Fourier decomposition	No restrictions. This document is available to the public through the National Technical Information Service, Springfield, Virginia 22161.

19. Security Classif. (of this report)	20. Security Classif. (of this page)	21. No. of Pages	22. Price
Unclassified	Unclassified	128	

Form DOT F 1700.7 (8-88)

EFFECT OF FINITE WIDTH ON DYNAMIC DEFLECTIONS OF PAVEMENTS

by

Yumin Vincent Kang
Jose M. Roesset
Kenneth H. Stokoe, II

Research Report Number 1123-6

Research Project 2/3-18-87/0-1123

Non-Destructive Test Procedures for Analyzing
the Structural Conditions of Pavements

conducted for

**Texas State Department of Highways
and Public Transportation**

in cooperation with the

**U. S. Department of Transportation
Federal Highway Administration**

by the

CENTER FOR TRANSPORTATION RESEARCH

Bureau of Engineering Research

THE UNIVERSITY OF TEXAS AT AUSTIN

January 1991

NOT INTENDED FOR CONSTRUCTION, BIDDING, OR PERMIT PURPOSES

Jose M. Roesset, P.E.
Kenneth H. Stokoe, II, P.E. (Texas No. 49095)
Study Supervisors

The contents of this report reflect the views of the authors, who are responsible for the facts and the accuracy of the data presented herein. The contents do not necessarily reflect the official views or policies of the Federal Highway Administration or the Texas Department of Transportation. This report does not constitute a standard, specification, or regulation.

PREFACE

Project 1123 is a joint project between the Center for Transportation Research at The University of Texas and the Texas Transportation Institute at Texas A&M University. The project deals with the development of experimental and analytical techniques for the nondestructive testing of pavements. This report is the second of three reports from the Center for Transportation Research. The report presents the results of numerical parametric studies to assess the effect of the position of the Dynaflect or Falling Weight Deflectometer loads with respect to the edge of the pavement or the predicted deflection basins. A general formulation to obtain the dynamic response of a body with a two dimensional geometry to a three dimensional load has been developed and implemented in a computer program. This program was then used to conduct the parametric studies. The report presents the formulation, validation of the computer code, and the results of the studies.

LIST OF REPORTS

(Note: Report Nos. 1123-1, 1123-2, 1123-3 and 1123-4F have been submitted through Texas Transportation Institute of Texas A&M University on their part of the joint Project 1123. The reports listed below are the reports submitted through the Center for Transportation Research at The University of Texas at Austin.)

Report No. 1123-5, "Experimental Study of Factors Affecting the Spectral-Analysis-of-Surface-Waves Method," by Glenn J. Rix, Kenneth H. Stokoe, II, and Jose M. Roesset presents the results of field studies of source types, and source-receiver configurations, and the distribution of surface wave motion on SASW measurements.

Report No. 1123-6, "Effect of Finite Width on Dynamic Deflections of Pavements," by Yumin Vincent Kang, Jose M. Roesset and Kenneth H. Stokoe, II, presents the results of analytical studies of the effects of the finite width of the pavement and the relative location of nondestructive testing devices on predicted dynamic deflections.

Report No. 1123-7F, "The Falling Weight Deflectometer and Spectral Analysis of Surface Waves for Characterizing Pavement Moduli: A Case Study," by R. F. Miner, K.H. Stokoe, II and W.R. Hudson, presents the results of a comprehensive field and laboratory study conducted during the construction of an overpass ramp in Austin, Texas.

ABSTRACT

A highway has a finite width in its transverse direction, and the existence of variation in material properties between the road and the surrounding soil is not uncommon. A three-dimensional elastodynamic solution is presented to take into account the variation of material properties in the soil-pavement system by using the Fourier superposition technique. The pavement, base and subgrade are represented by a finite-element core region. An expansion technique is used to simulate the infinite lateral soil region. A viscous boundary is implemented for a half space condition. The stiffness matrices and point load and disk load vectors are obtained in the frequency-wavenumber domain. Parametric studies of the soil-pavement formulation are conducted to assess the accuracy of the results.

An investigation of the effects of the lateral boundary on the pavement deflections measured by various nondestructive testing techniques is presented. The Dynaflect, the Falling Weight Deflectometer (FWD), and the Spectral-Analysis-of-Surface-Waves (SASW) methods are simulated on three typical in-service pavement sections. The results of the Dynaflect tests indicate that the effects of the lateral boundary on the measured deflections are directly related to: (a) the loading position with respect to the edge of the pavement; (b) the thickness of the surface layer; (c) the lateral stiffness contrast between the road and the surrounding soil; (d) the height of the ramp, if the test is performed on a ramp. A closer loading position, a larger value of the thickness, a higher contrast, and a larger value of the ramp height will result in a larger influence on the deflections. The lateral boundary also has a differential influence on different stations which will, in turn, change the shape of the deflection basins. The existence of retaining walls is important, especially for the "high" ramp. Similar conclusions are reached for the FWD test simulations. The results of the SASW tests indicate that some fluctuations may occur in the dispersion curve because of the reflected body waves due to the abrupt change in the stiffness at the horizontal interfaces between layers. The existence of the lateral boundary causes additional fluctuations, particularly for long wavelengths.

KEY WORDS: Finite width pavements, Dynaflect, Falling Weight Deflectometer, Spectral Analysis of Surface Waves, Finite Elements, Fourier decomposition

SUMMARY

The Dynaflect, the Falling Weight Deflectometer and the Spectral Analysis of Surface Waves are three procedures commonly used for non-destructive testing of pavements. The first two provide the deflections at a number of stations along the pavement caused by a steady state dynamic load or an impact. The elastic moduli of the pavement, base and subgrade are then estimated by comparing the measured deflections to those resulting from analyses changing the layer properties and iterating until a reasonable match between experimental and numerical results is found. The analyses are normally performed assuming static conditions and ignoring therefore any possible dynamic effects. This is a problem that has been investigated in other reports. In addition all analysis programs, whether static or dynamic, assume that the pavement system extends to infinity in the two horizontal direc-

tions and that the deflections are independent of the position of the load with respect to the edge of the pavement. In this work the effects of the finite width of a pavement and the position of the load are investigated. The formulation and mathematical model to determine the dynamic response of a body with a two dimensional geometry to a three dimensional load are presented and the results of the computer program are validated by comparing them to those of other established codes when the pavement extends to infinity. Parametric studies are then conducted for four different pavement profiles in order to assess under what conditions the effect of the finite pavement width may influence significantly the deflection basins.

IMPLEMENTATION STATEMENT

The results of the parametric studies conducted indicate that the effect of the finite pavement width will be negligible generally when dealing with flexible pavements. It may be more important however for stiff pavements depending on the contrast in properties with the surrounding soil. It can be significant when dealing with a pavement or an embankment with or without retaining walls. Although experimental verification of these studies is needed before providing final recommendations and the number of cases considered is limited, it would appear from the results that the Dynaflect or Falling Weight Deflectometer loads should be placed at least 4 ft from the pavement edge and that this distance should increase when dealing with an embankment. Otherwise the values of the moduli predicted using the standard backcalculation procedures may be unreliable.

TABLE OF CONTENTS

CHAPTER 1. INTRODUCTION

1.1 Background

The determination of the structural capacity of pavements has always been a problem of major concern in highway management. A knowledge of the structural condition of the pavement provides valuable information for (1) determination of structural adequacy, which permits the estimation of the remaining life of the pavement and when rehabilitation should be accomplished; and (2) selection of feasible rehabilitation and/or reconstruction strategies. The importance of this evaluation in the decision making of many highway and airfield agencies has increased recently, as many major highways and airport runways are approaching the end of their serviceable lives.

In practice, the structural evaluation can be performed through two types of testing techniques. One is called destructive testing and the other nondestructive testing. Destructive testing is often accomplished through coring, test pits and sampling followed by field and laboratory tests. It can provide detailed profiling, the extent of deterioration, and the material properties including elastic moduli, water content, density, gradation, etc. Four main problems associated with destructive testing are (1) the representation of the samples over the whole section; (2) the disturbance of the materials caused by the coring and sampling; (3) the interruption of normal traffic; and (4) the inability to conduct periodic monitoring over a particular section.

On the other hand, nondestructive testing techniques, in which the structure of the pavement is not altered by the testing, can be employed at the same location as often as necessary. Figure 1.1 illustrates schematically a nondestructive test. The test is usually performed along the longitudinal direction of the pavement (i.e., the direction of traffic). The response of a pavement due to a quasi-static or dynamic load is generally measured in terms of surface deflections. The measured deflections are then analyzed through an inversion process to determine the structural adequacy of the pavement. Many methods of structural evaluation were originally based on limiting deflection criteria by empirically correlating pavement performance with the measured deflections. Increased research efforts, however, are under way to develop a more rational and mechanistic approach for structural evaluation by the application of multilayered elastic theory to back-calculate the in-

situ elastic moduli of the pavement from the measured deflections. The estimated in-situ moduli can then be used as input in a forward model to calculate the critical stresses and strains of the pavement under a given design load configuration. From this, the fatigue life and the remaining life of the pavement can also be estimated.

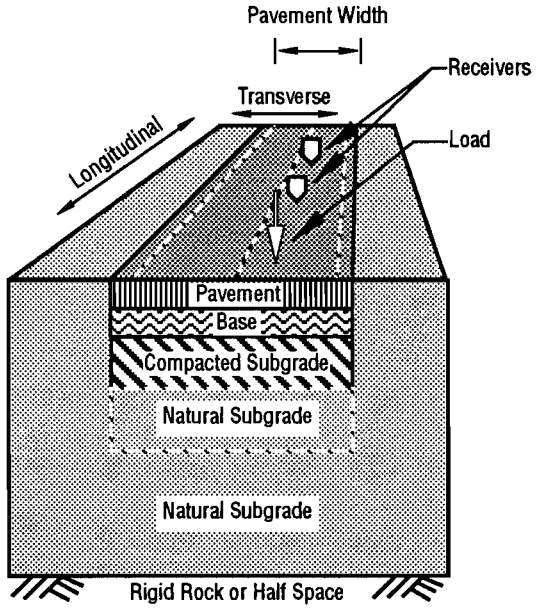

Figure 1.1 Illustration of nondestructive testing on pavement system

With today's technology of high speed computers and data acquisition devices, nondestructive testing techniques have become more and more promising. A number of procedures and associated equipment [e.g. Dynaflect, Falling Weight Deflectometer (FWD), and Spectral Analysis of Surface Waves (SASW)] have been developed in recent years. However, there are still some problems which have not yet been fully resolved, especially in the inversion process. Because of the complexity of the inversion process, efforts have been made to understand its feasibility and limitations through the use of forward modelling. An appropriate forward model can be used not only as a research tool to study the important variables and their associated limitation in the inversion process, but also as a design tool to determine the structural adequacy of pavements.

There are several forward models or theories available for calculating behavior or response within a pavement structure due to a given load condition. The elastic multilayered theory developed by Burmister (1945) is mainly used for the analysis of flexible pavements, while the most frequently used model for rigid pavements is based on Westergaard's theory (1926) (to perform analysis of thick elastic plates on a Winkler-type soil).

A potential problem with these formulations is that they are all based on static loading while most of the nondestructive tests are of a dynamic nature. A three-dimensional elastodynamic solution obtained by Kausel (1974) was recently applied to nondestructive testing of pavements by Roesset and Shao (1986). It was demonstrated that under certain

conditions, a static interpretation of dynamic deflections may result in substantial errors. The use of Kausel's formulation allows one to obtain dynamic deflections under axisymmetric conditions. This is the formulation that has been used until now in the dynamic testing of pavements. It assumes therefore that the pavement has infinite dimension in the horizontal plane, as shown in Figure 1.2. In other words, it does not allow material variation in the horizontal directions.

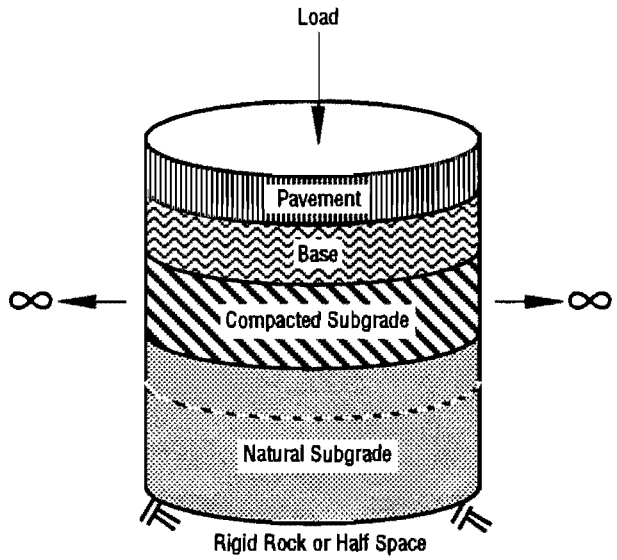

Figure 1.2 Schematic diagram of a three-dimensional layered system under axisymmetric condition

In reality, however, a highway pavement has a finite width in the transverse direction, as shown in Figure 1.1. More importantly, most of the nondestructive testing procedures (The Asphalt Institute, 1977; ERES Consultants Inc., 1983) require that on multiple lane facilities, the test be performed at least on the outer lane, because it is the heaviest travelled truck lane. As a result, it is important to quantify the effect of the lateral boundary on the measured deflections in order to provide recommendations for a more effective use of nondestructive testing techniques.

1.2 Objectives and Organization

The principal goal of this report was to develop a mathematical model of soil-pavement systems, which can account not only for the dynamic nature of the loading, but also for the existing lateral boundary conditions. Studies of the effect of test loading position should help to understand the importance of accurate placement of a deflection device.

An overview of the commonly used nondestructive testing techniques is presented in Chapter 2. Emphasis is placed on the key characteristics of each testing technique in order to give a firm background of the principles involved. The relative advantages and disadvantages of each method are also addressed.

In Chapter 3, a new formulation for soil-pavement systems is presented. The soil-pavement structure is modeled as a layered stratum resting on a rigid rock or half space. The material is assumed to be isotropic, homogeneous, and linearly viscoelastic. Fourier superposition analysis is applied to the time variable as well as the spatial variable. The stiffness matrices and load vector are obtained in the frequency-wavenumber domain. A special technique is used to obtain the stiffness matrix for the infinite lateral region.

Chapter 4 includes validation of the soil-pavement formulation with Kausel's formulation. Parametric studies of key variables are performed to assess the accuracy of the results. The sensitivity of the results to various parameters is addressed.

The application of the soil-pavement formulation to simulate the nondestructive test methods is presented in Chapter 5. The potential problems in each testing technique due to neglecting the existing lateral boundary conditions and the relation of loading position with respect to the pavement edge are discussed.

Finally, the major findings are summarized in Chapter 6. Conclusions and recommendations are also included.

CHAPTER 2. OVERVIEW OF NONDESTRUCTIVE TESTING METHODS USED FOR STRUCTURAL EVALUATION OF PAVEMENT SYSTEMS

2.1 Introduction

In nondestructive testing, the equipment in current use generally provides measures of the surface deflections due to an applied load. Because of inherent differences in the loading mechanisms, these devices will produce different deflections and hence lead to different data interpretations. Based on the type of applied load, nondestructive testing devices can be categorized into three groups: slowly moving load, vibratory load and impulse load. Table 2.1 gives examples of several devices and their loading characteristics. Detailed information on many of these devices can be found in Moore (1978) and Epps, *et al* (1986).

This chapter will discuss the general principles involved in each group as well as specific equipment and procedures that are commonly in use. The relative advantages and disadvantages of each device will be addressed.

Table 2.1 List of Nondestructive Testing Devices

Category	Device
Slowly Moving Load	Benkelman Beam Traveling Deflectometer
Vibratory Load	Dynaflect Road Rater
Impulse Load	Falling Weight Deflectometer Spectral Analysis of Surface Waves

2.2 Benkelman Beam Test

The Benkelman beam is the most common equipment used to measure the response of pavements due to a slow-moving load. A schematic of the device is shown in Figure 2.1. It consists of a simple lever arm attached to a lightweight frame. The probe of the beam is placed between the dual wheel of a vehicle axle ballasted to the desired load. The motion of the beam is observed on a deflection dial gauge.

This equipment has been used for many years. It is commercially available and relatively inexpensive. However, a serious problem with this type of measurement is the difficulty in obtaining an immovable reference point for making the deflection measurements. Because of this problem, the absolute accuracy of this method is questionable. Moreover, it is difficult to correlate the nearly static results to the response of pavements to high-speed traffic loads. Therefore, no further attention will be paid to this method.

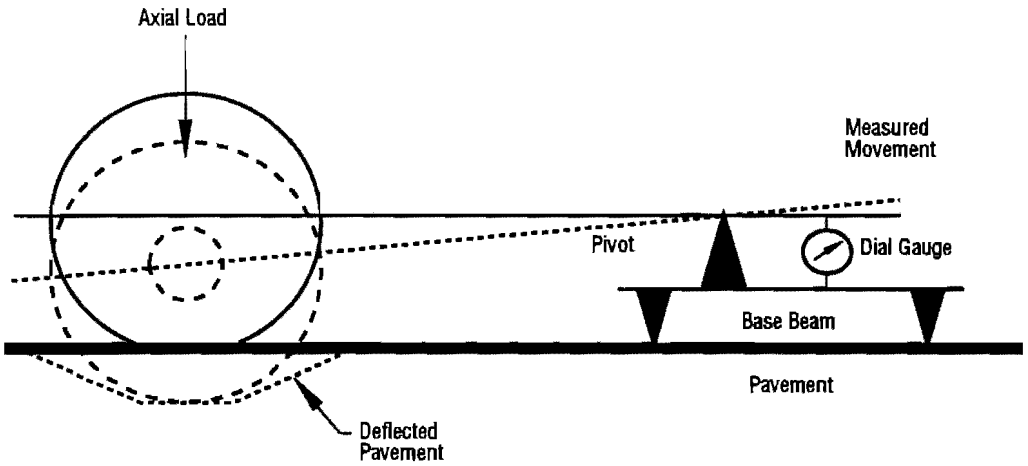

Figure 2.1 Schematic of the Benkelman Beam Device (after Lay, 1986).

2.3 Dynaflect Test

Although there are different types of vibratory load equipment being used, they all share many of the same characteristics. Basically they apply a steady-state sinusoidal force to the pavement system.

Deflections are then measured with inertial motion sensors (either accelerometers or velocity transducers, also called geophones).

One commonly used device is the Dynaflect, as illustrated in Figure 2.2. It employs two counter-rotating eccentric masses operating at a fixed frequency of 8 Hz, which results in steady-state vibrations that are a sinusoidal function of time. A typical forcing function of the Dynaflect is shown in Figure 2.3, where a 1,000-pound peak-to-peak magnitude of dynamic force is super-imposed upon a static load of 1,800-pounds. This steady-state vibratory force is applied to the pavement through two 4-in. wide,16-in. diameter rubber-coated steel wheels which are spaced 20 in. center-to-center (Figure 2.4). Five equally spaced geophones at one-foot intervals are used to measure the vertical velocities of the pavement system. The signals are then integrated electronically to obtain deflections.

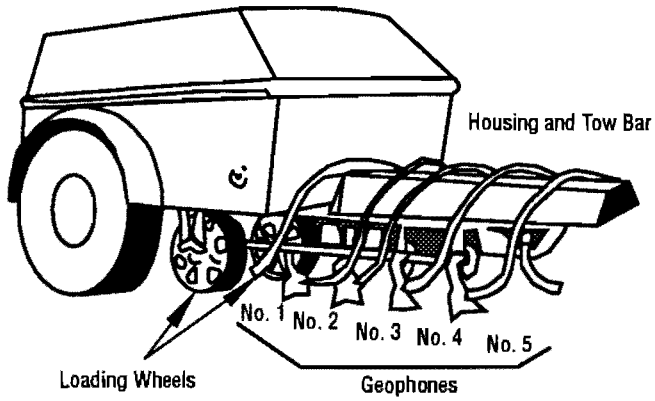

Figure 2.2 The Dynaflect device (from Uddin *et al*, 1983)

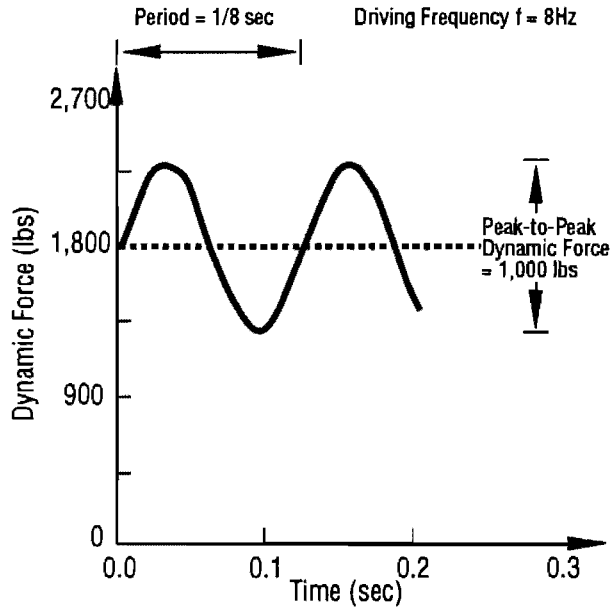

Figure 2.3 Forcing function of the Dynaflect device

Peak-to-peak dynamic deflections obtained from the array of five geophones form half of the deflection basin as illustrated in Figure 2.5. Several basin parameters have been used for rating the structural condition of a pavement, such as maximum Dynaflect deflection, surface curvature index, basin slope, etc.

The major advantage of the Dynaflect test compared with the Benkelman beam test is that accurate deflection basin measurements can be made with respect to an inertial reference frame. In addition, it is very rapid and simple to operate. The total time required for making a set of five deflection measurements is about two minutes.

The major disadvantage associated with the Dynaflect is that only the deflection response due to an excitation of 8 Hz is measured. It does not accurately reflect the traffic load in terms of its frequency content. However, from the theoretical point of view it is much less expensive to simulate the Dynaflect since only one frequency is needed. In addition to the limitation of its frequency content, the results of the Dynaflect represent only the global

response of the entire structure. It does not provide direct information for separation of the effects of various layers in the pavement system, and back-calculation of Young's moduli for various layers remains problematic.

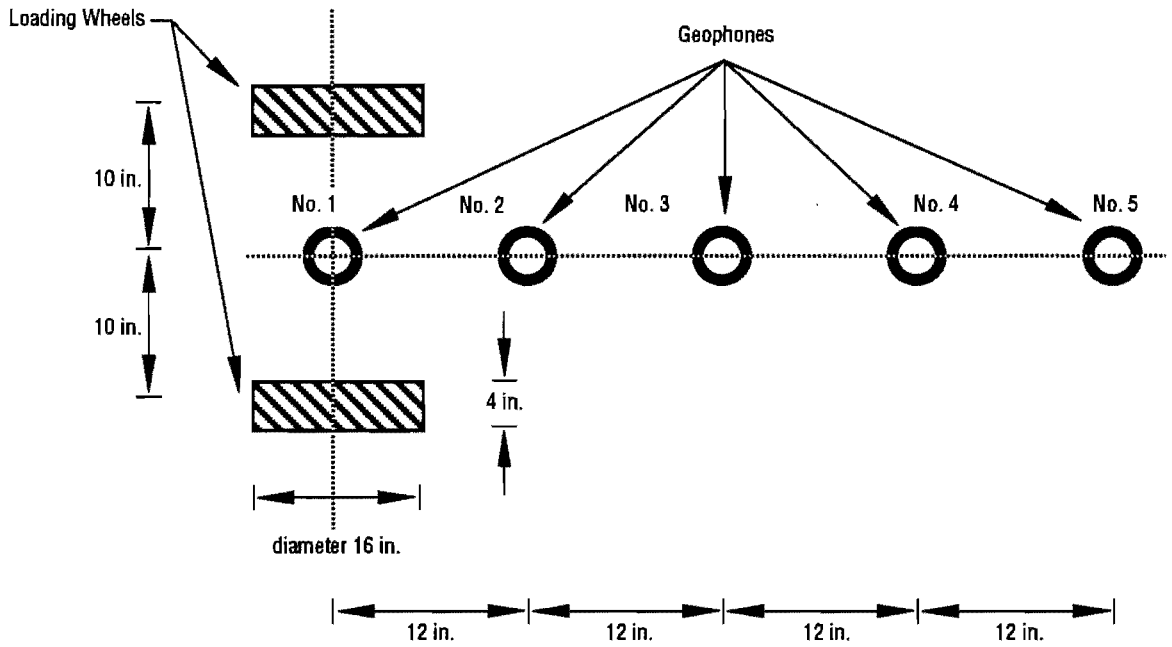

Figure 2.4 Top view of Dynaflect loading wheels and geophones (after Uddin *et al*, 1985)

2.4 Falling Weight Deflectometer

In principle, all impact load testing methods generate some type of transient load applied to the pavement surface and measure its transient response. The Falling Weight Deflectometer (FWD) is the one which is believed to more closely simulate the deflections produced by moving traffic wheels. Figure 2.6 shows a schematic diagram of the FWD device. Basically it applies an impulse load by dropping a known mass (ranging from 110 to 660 lbs) from a predetermined height (ranging from 0 to 16 inches). The mass falls on an 11.8-inch-diameter loading plate which is resting on a 0.22-inch-thick rubber buffer. The resulting force forms approximately a half-sine wave with a peak magnitude ranging from 1,500 to 24,000 lbs and a duration of about 25 to 30 msec (Figure 2.7). A properly designed mass configuration and buffer characteristics are very important to achieve the desired peak stress, the shape and the duration of the FWD force signals.

The resulting velocity histories v(t) due to the impact load are measured by velocity transducers located at 0, 1, 2, 3, 4, 5, 6 ft from the center of the loading plate (Figure 2.6). The surface deflection history x(t) at each station is then obtained by integrating the corresponding velocity along the time axis. The maximum deflection is selected from each deflection trace. By connecting the maximum deflection of each station, a deflection basin is obtained.

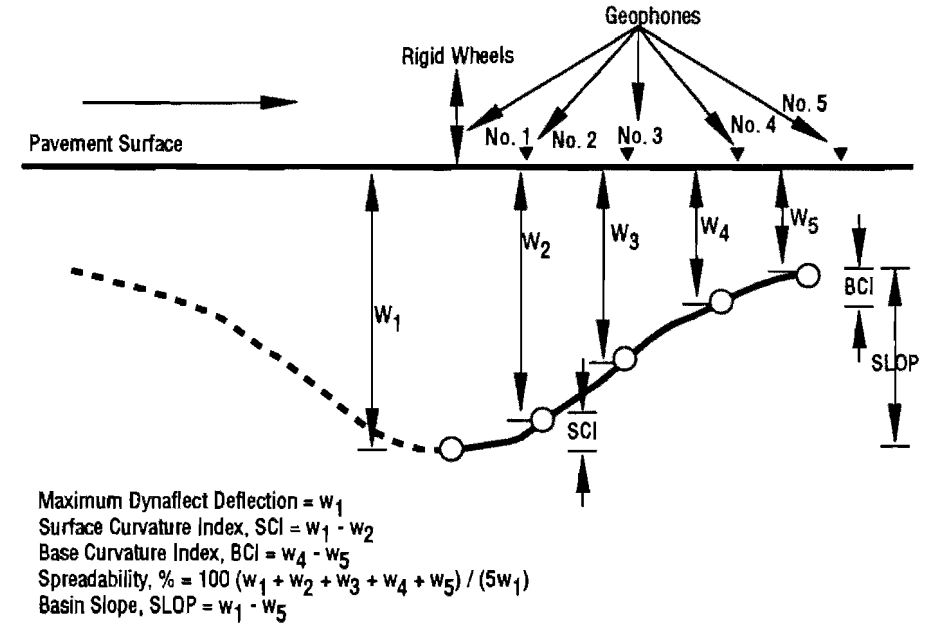

Figure 2.5 Typical Dynaflect deflection basin (from Uddin *et al*, 1985)

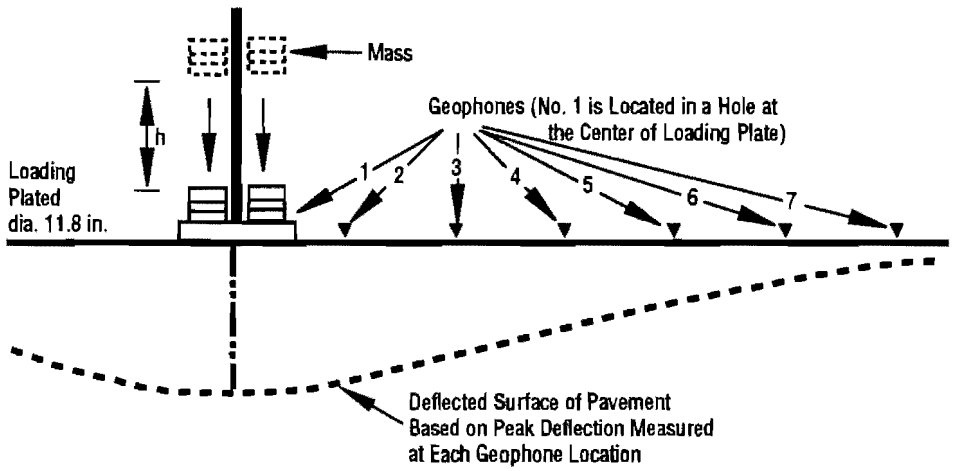

Figure 2.6 Schematic of the FWD device (from Uddin *et al*, 1985)

Since the load applied in the FWD method is transient in nature, it effectively contains sinusoidal waves over an extended range of frequencies. Likewise, the deflection measured at each station contains all frequencies. Using the Fourier transform, one can decompose the time history of the deflection x(t) into its frequency components $\overline{X}(f)$. That is

$$\overline{X}(f) = \int_{-\infty}^{+\infty} x(t)\ e^{-i 2\pi f t}\ dt \qquad (2.1)$$

Each frequency component will then represent the steady-state deflection at that frequency. Therefore, with only one impact load one can obtain the same information as in a number of steady-state deflection tests. This is the main advantage of the FWD over the

steady-state deflection tests. In addition, because of its good correlation with the deflections induced by traffic loads, this method is widely used nowadays in engineering practice.

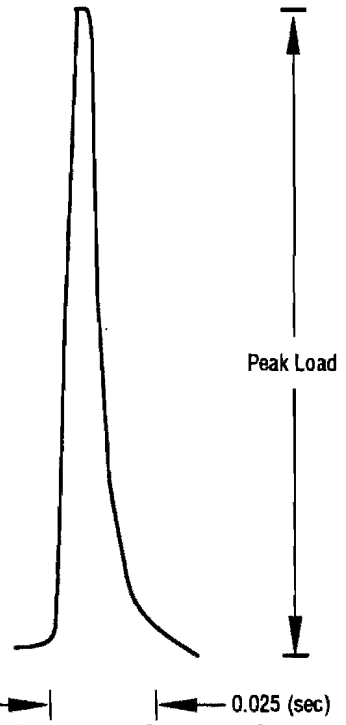

Figure 2.7 Time history of the FWD forcing function of pavement surface (from Uddin *et al*, 1985)

However, since only the maximum deflection basin of the FWD is being used in practice, the FWD technique is like any other type of deflection testing in that the results represent a global characterization of the entire structure and do not provide information that can readily be used to separate the effects of various layers in the pavement system. In addition, for computer simulation it needs essentially either time integration for a time-domain solution or all of the frequency components for a frequency-domain solution. Therefore, it is more expensive to simulate the FWD than the Dynaflect.

2.5 Spectral Analysis of Surface Waves Method

The Spectral-Analysis-of-Surface-Waves (SASW) method is a relatively new method of dynamic testing developed to determine shear wave velocities and shear modulus profiles at soil sites (e.g. Stokoe and Rix, 1988) and Young's modulus profiles at pavement sites (e.g. Nazarian *et al*, 1983). Like the FWD method, the SASW method applies a transient impact on the pavement surface. However, the SASW method makes use of the theory of surface waves in a layered system to interpret the results and differs from other deflection testing techniques in many aspects. A brief overview of the SASW method is presented here. For more detailed information, the reader is referred to Nazarian and Stokoe (1985a and 1985b).

The general configuration of the SASW test is shown in Figure 2.8. The source is simply a transient vertical impact on the pavement surface. Two vertical receivers are placed on the

surface to measure the time records of the surface motions. The output of the receivers is simultaneously recorded on a dynamic signal analyzer for future data reduction. The test is repeated for different source-receivers spacings. The most common type of geometrical arrangements for the source and receivers is called the common receiver midpoint geometry, as illustrated in Figure 2.9.

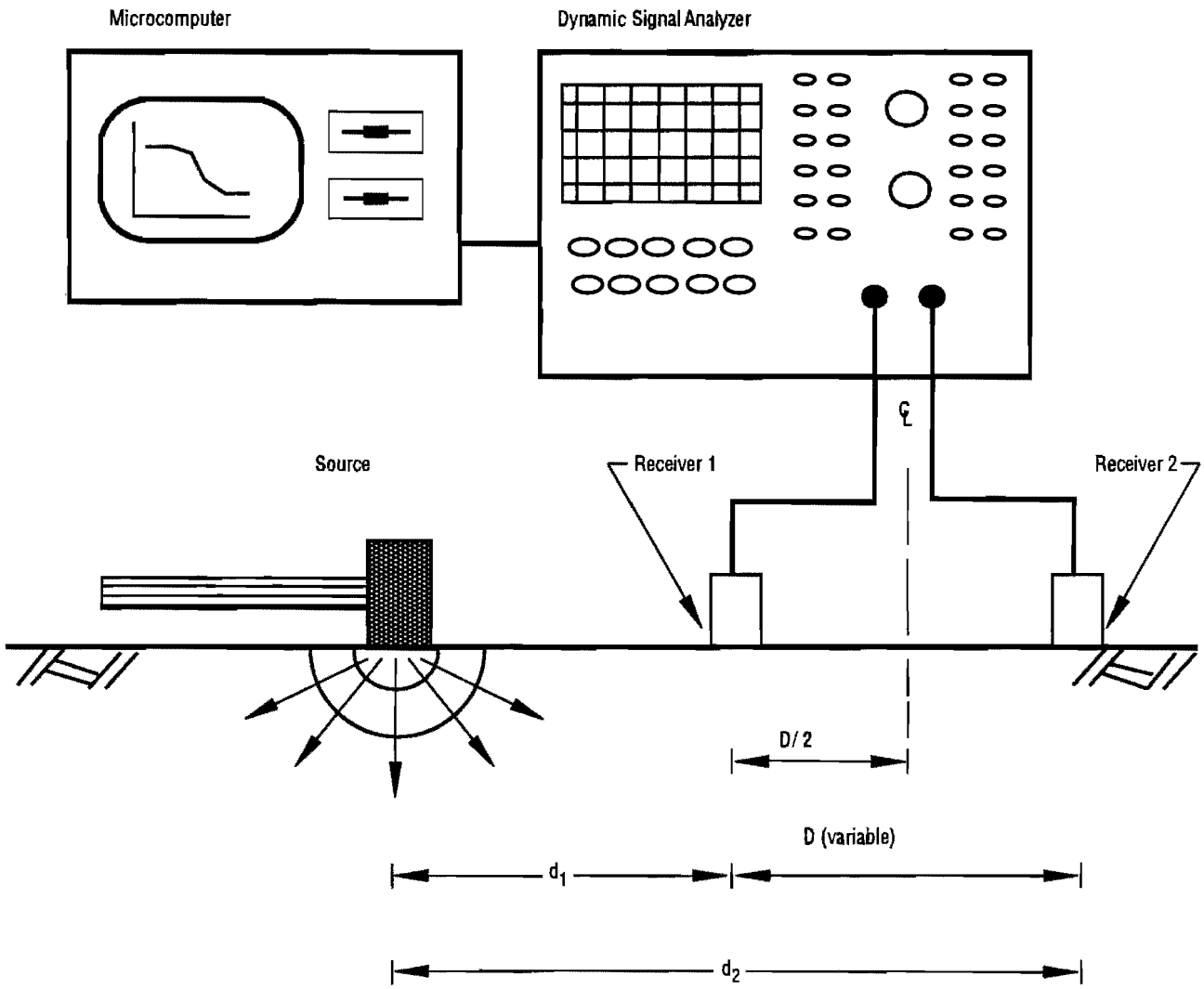

Figure 2.8 General configuration of the SASW test

The basis of the SASW method is the dispersion of surface waves in a layered medium. A plot of phase velocity versus frequency or wavelength is called a dispersion curve.

The dispersion of surface waves can be easily understood in terms of wavelength. It is well known that surface waves decay rapidly with depth below the surface, as shown in Figure 2.10. Notice that the vertical axis is the vertical depth normalized with respect to wavelength. In a practical sense, this means that waves with short wavelengths (high

frequencies) propagate only in the upper layers. They are therefore influenced most by the properties of these layers. Waves with long wavelengths (low frequencies), on the other hand, travel through deeper layers as well as the near-surface layers. Thus they are influenced

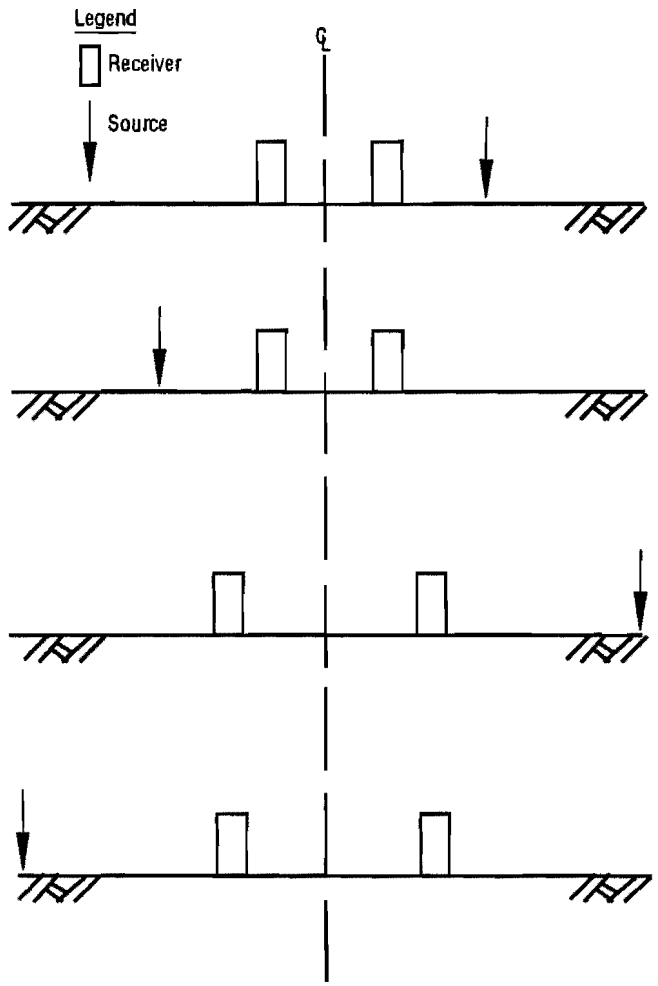

Figure 2.9 Common receiver midpoint geometry

to a large extent by the properties of the deeper layers. Two examples are presented to illustrate the dispersive nature of the surface waves. In Figure 2.11a, the shear wave velocities of the layers increase with depth, which is very common for many soil or rock sites. The same trend can be found in the dispersive curve (Figure 2.11b), where the shear wave phase velocities increase as the wavelength increases. For a pavement profile, shear wave velocities (Figure 2.12a) decrease usually with depth and the dispersion curve will also decrease with depth (Figure 2.12b).

In data reduction of SASW testing, the time records obtained from the two receivers are decomposed into their frequency components, usually by means of an FFT (Fast Fourier Transform). The results in the frequency domain are complex functions of frequency, which consist of a real and an imaginary part. The results can also be expressed in terms of magnitude and phase angle. It is the phase angle spectrum that is used for the dispersion analysis.

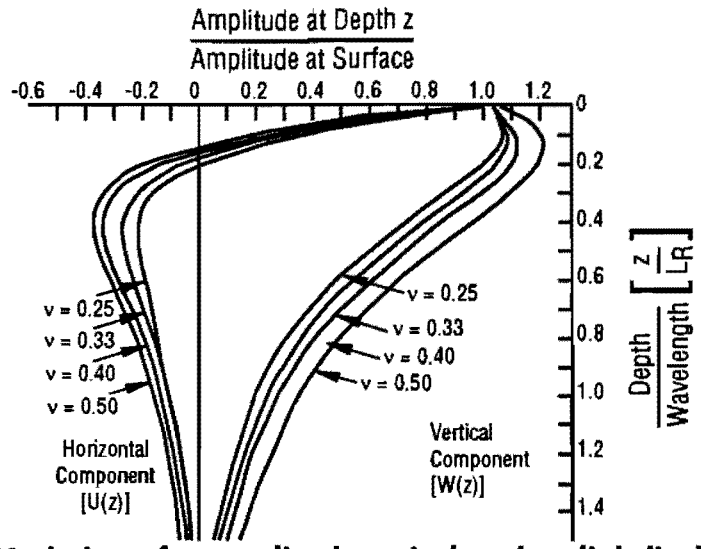

Figure 2.10 Variation of normalized vertical and radial displacements with normalized depth for a surface (Rayleigh) wave propagation in a uniform half space (from Richart *et al*, 1970)

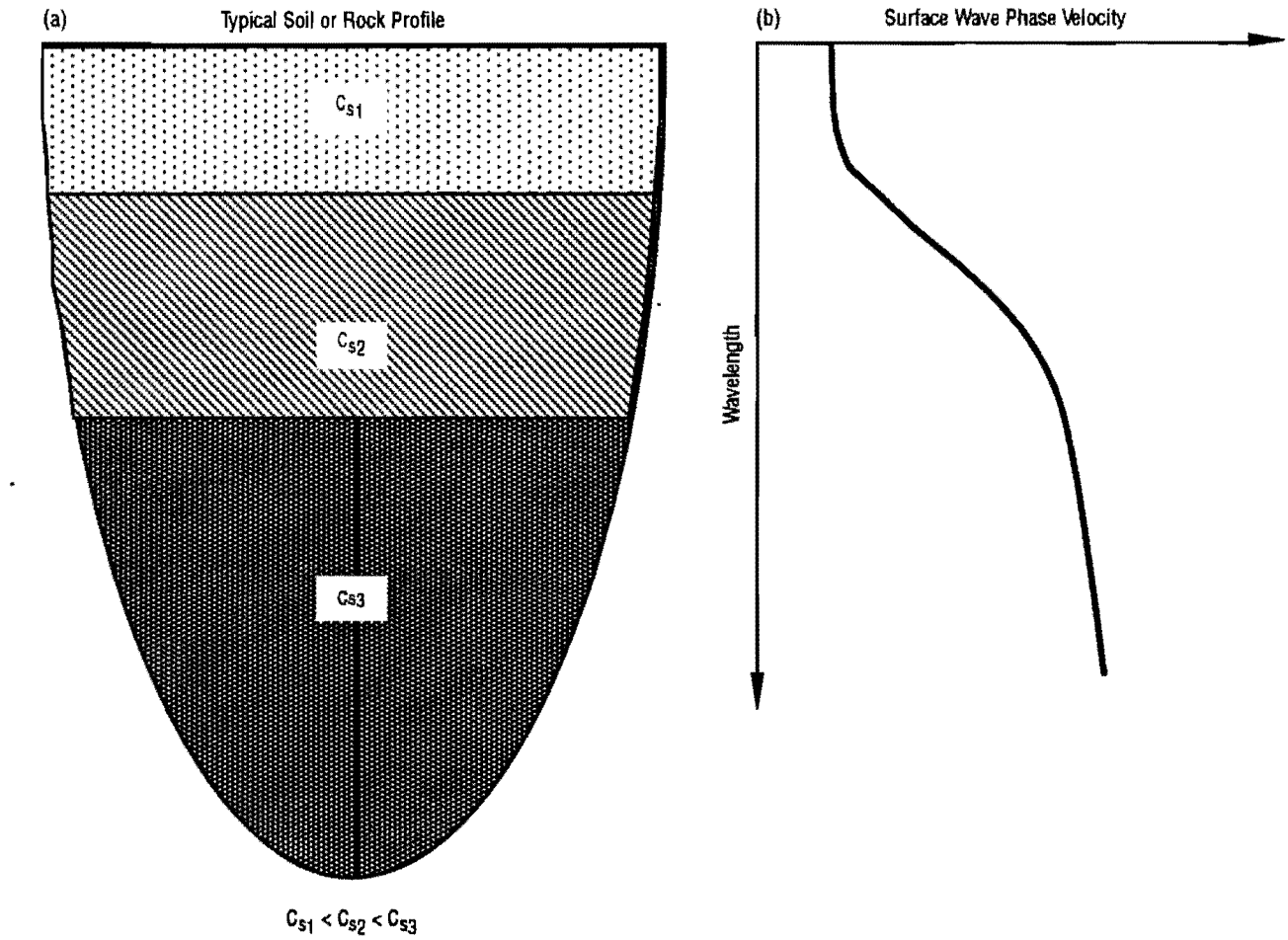

Figure 2.11 Surface wave dispersion in a layered half space for a typical soil or rock site

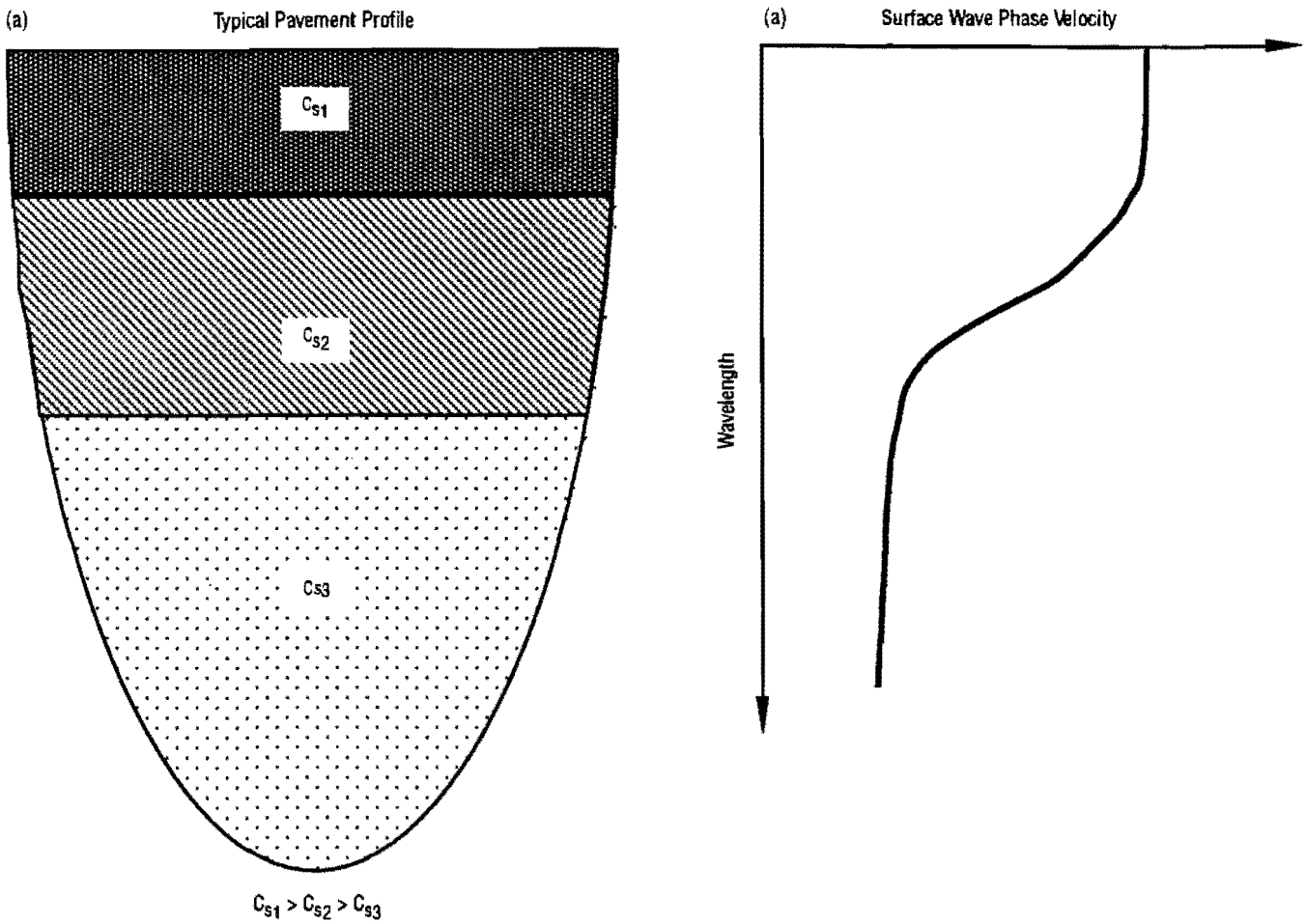

Figure 2.12 Surface wave dispersion in a layered half space for a typical pavement site

For a given frequency, f, the time delay, t, between receivers can be calculated using:

$$t = \frac{\phi}{360 \bullet f} \tag{2.2}$$

where ϕ is the phase difference between receivers, expressed in degrees. The surface wave phase velocity, C_R , is then determined using:

$$C_R = \frac{d_2 - d_1}{t} \tag{2.3}$$

in which d_1 is the distance from the source to the first (near) receiver and d_2 is the distance from the source to the second (far) receiver, as shown in Figure 2.8. The final step in calculating the dispersion curve is to determine the corresponding wavelength using :

$$\lambda_R = \frac{C_R}{f} \tag{2.4}$$

It can be seen that if phase difference and frequency are known, phase velocity and wavelength can be easily determined using Eqs. (2.3) and (2.4). By repeating this process for other frequencies on each record, a number of data points are obtained, from which the dispersion curve can be constructed.

The final task in SASW testing is to determine the shear wave velocity profile from the dispersion curve. This process is called inversion of the dispersion curve or simply inversion. There is a crude type of inversion that has been used for many years in which it is assumed that the sampling depth is equal to one-half to one-third of the wavelength and that the shear wave velocity is equal to 1.1 times the surface wave velocity (Heisey *et al*, 1982; Richart *et al*, 1970). In other words, the shear wave velocity profile can be obtained simply by multiplying the scale of the wavelength axis by one-half or one-third and the scale of phase velocity axis by a value of 1.1. Once the shear wave velocity profile is constructed, the shear modulus and Young's modulus profiles can be obtained, provided that Poisson's ratios and mass densities are determined by other means.

An increasing research effort has been devoted to improving the SASW method. A plane Rayleigh wave inversion process was introduced to determine more accurate shear wave velocity profiles (Nazarian, 1984). Sánchez-Salinero (1987) performed a theoretical study of the appropriateness of assuming plane Rayleigh waves in surface wave testing and the effects of different source-receivers configurations. Rix (1988) conducted an extensive experimental investigation of factors which affect surface wave testing such as the types of source, and the assumption of a fundamental mode in the theoretical displacement calculation. In many aspects, the SASW method is still in research and development stages. Nevertheless, it is a method which offers a great deal of promise. It provides a tool having a rigorous basis for separating the effects of various layers, so that a unique profile and layer thickness can be determined with great accuracy. However, the method itself is more involved than other testing techniques. It needs more attention to details on how to perform the test, and correctness of the phase information both from the theoretical and field study. It is hoped that once the system is fully automated, it will be just as fast to perform a SASW test as any other nondestructive testing method.

2.6 Summary

The general principles of four types of nondestructive testings have been discussed in this chapter. They are the Benkelman beam, the Dynaflect, the FWD and the SASW tests. The Benkelman beam test has been widely used in practice due to its simplicity and ease of testing, in spite of the fact that it is difficult to obtain an immovable reference frame for deflection measurements and that static deflections are not well correlated to those induced by dynamic traffic loads.

The Dynaflect test uses inertial sensors so that accurate deflections can be measured. However, only one frequency is being used. The correlation of test results to traffic loads is questionable.

The FWD device generates essentially all frequency components. It has gained widespread popularity among highway agencies because of its good correlation with moving traffic loads. However, like the Benkelman beam and the Dynaflect tests, the FWD characterizes only the entire pavement structure. It does not provide direct information to separate the effects of various layers.

The SASW testing is a relatively new method. Based on the dispersive nature of surface waves in a layered medium, it provides direct evaluation of individual layers so that a unique profile can be determined.

Finally, it should be recognized that each testing technique has its own merits, especially when considering the integrity of the entire procedure from the field testing to the data reduction. It is hoped that with today's technology, the results of nondestructive tests can be properly interpreted by analyzing extensive field data and synthetic results and that this will, in turn, result in a more rational and mechanistic approach for structural evaluation of pavement.

CHAPTER 3. MATHEMATICAL FORMULATION OF SOIL-PAVEMENT SYSTEM

3.1 Introduction

Many problems in the fields of soil-structure interaction, nondestructive testing and soil dynamics can be schematically depicted as in Figure 3.1. This system consists of an irregular core region and two semi-infinite layered regions. Normally the dimensions of the core region are finite. It is therefore rather straightforward to model it with a finite number of degrees of freedom. Many well developed discretization procedures like the Finite Element or the Finite Difference methods are readily available for this purpose. A more difficult question is how to model and analyze the surrounding soil which is essentially an infinite medium. For static loading, one simple way is to introduce a fictitious boundary at a distance from the core region, where the response is expected to have died out. However, for dynamic loading the fictitious boundary will reflect the waves back into the core region instead of letting them pass through the interface and propagate toward infinity. One way to tackle this problem for solutions in the time domain is to locate the fictitious boundary at a distance such that the time of arrival of reflected waves exceeds the time span of interest. In many cases this requires the use of a very large mesh which will result in large computer memory and execution time. It is therefore desirable to seek some means to reduce the number of degrees of freedom necessary to model the whole system without loss of accuracy.

In the literature, special boundaries which can prevent the "false" wave reflections at the edges of the core region are normally referred to as nonreflecting, transmitting or absorbing boundaries. If the solutions are exact, in the finite-element sense, the boundaries are said to be consistent. A number of typical examples can be found in the literature. Lysmer and Waas (1972) presented a consistent lateral boundary for time-harmonic waves in plane strain or antiplane shear as well as axisymmetric waves in a layered stratum. The method was expanded by Kausel (1974) to nonaxisymmetric waves in axisymmetric regions of a layered stratum. More general consistent boundaries can also be developed using Green's functions in connection with the boundary integral method (Kausel and Peek, 1982). There are also some other types of approximate transmitting boundaries, such as Lysmer-

Kuhlemeyer, Engquist-Majda, Ang-Newmark, Smith-Cundall, and Liao-Wong boundaries. A comprehensive discussion of these boundaries can be found in Kausel (1988).

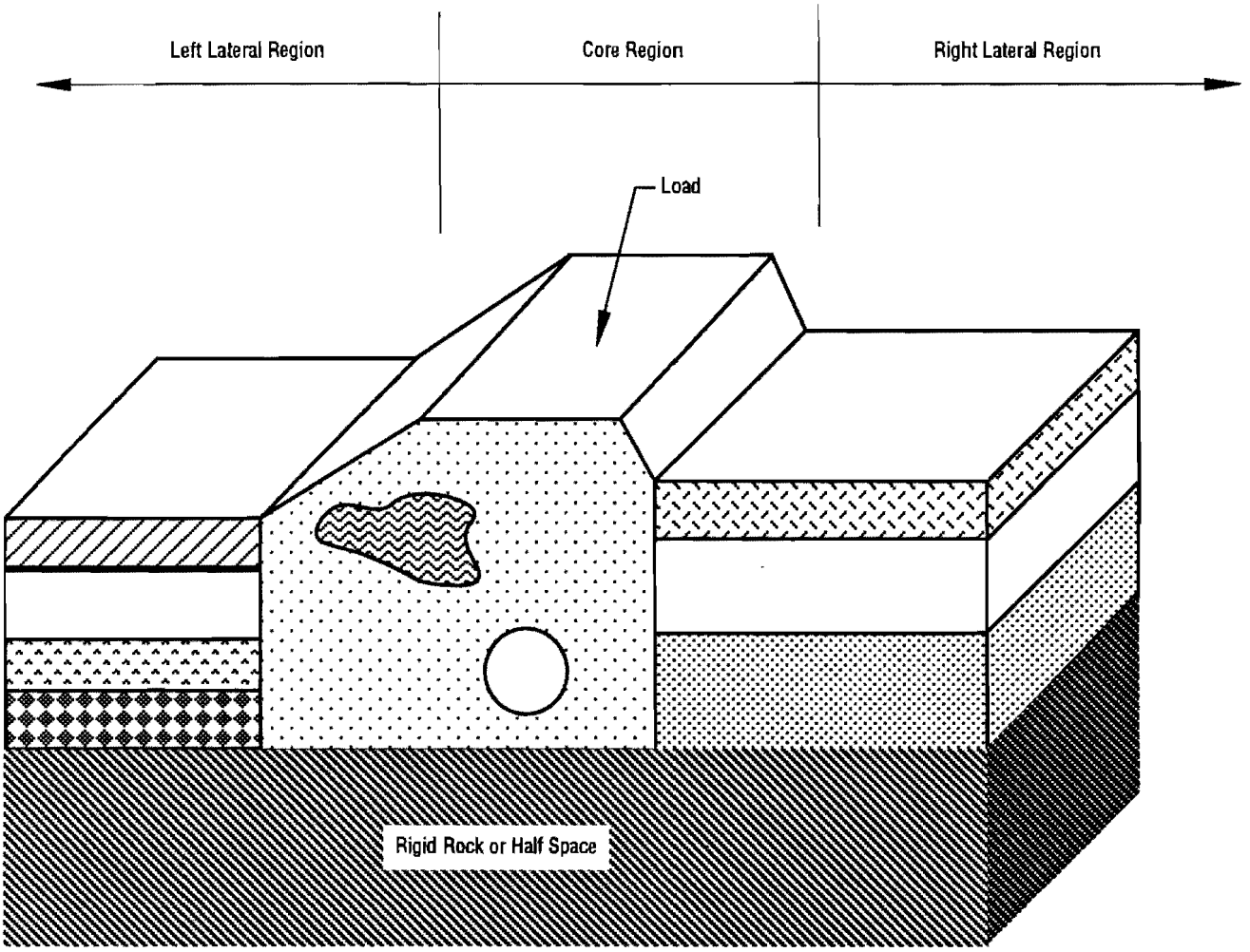

Figure 3.1 Typical three-dimensional structure

Using the consistent boundary of Waas (1972) for a problem with a two dimensional geometry and an inplane or antiplane line load, one can determine the displacements in the plane as a function of frequency or time. For problems where the geometry is axisymmetric, the use of Kausel's (1974) consistent boundary allows one to obtain displacements due to point, disk or ring loads. This is the formulation that has been used until now in the dynamic analysis of pavements, either for the Dynaflect, the Falling Weight Deflectometer or the Spectral-Analysis-of-Surface-Waves. It assumes that the pavement has infinite dimension in the horizontal plane.

In reality, however, a pavement has a finite width in the transverse direction (i.e. the x-direction) as shown in Figure 3.2. In the longitudinal direction (i.e., the direction of traffic, also the y-direction), one can consider the pavement to have infinite dimension. By assuming no structural (material or geometrical) variations in the y-direction, a soil-pavement system can be treated as a two-dimensional structure. For a vertical line load uniform in the

y-direction, the problem will be a two-dimensional one. The solution can be obtained by using Waas' consistent boundary. However, the assumption of a line load is not realistic in nondestructive testing for pavements, since it is the variation of deflections along the direction of traffic (the deflection basin along the y-direction) which must be modeled, as discussed in Chapter Two. For this reason, the load should be modeled as either a point load or a disk load in a three-dimensional space. The purpose of the present formulation is to derive a solution for the case of a two-dimensional structure subjected to a three-dimensional load. Most of the concern will be placed on the formulation and investigation of

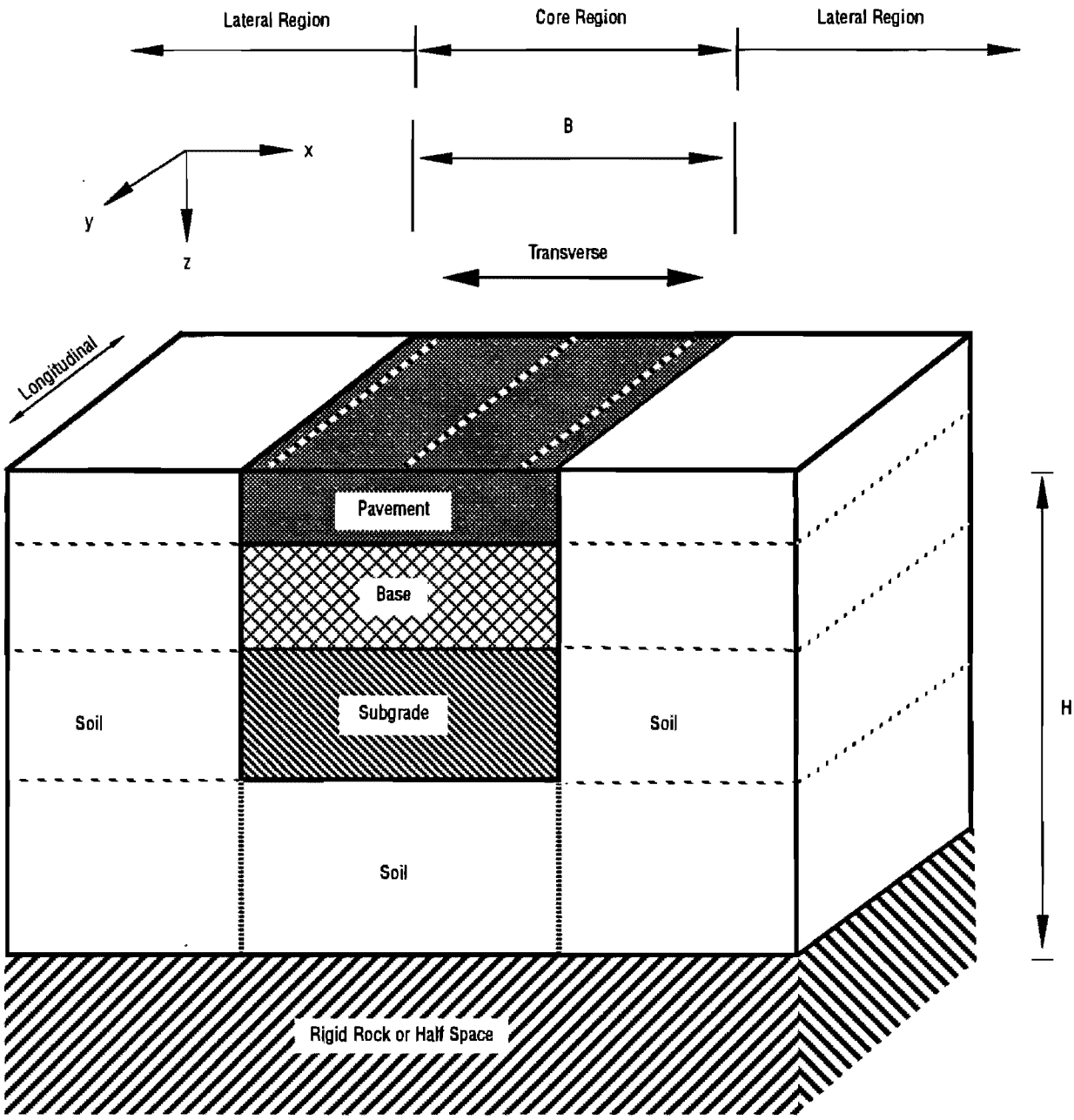

Figure 3.2 Idealized soil-pavement system

soil-pavement systems, although the formulation can be applied equally well to many other practical problems which share the same kinds of features, such as tunnel detection, material characterization of dams, etc.

The formulation described in this chapter starts with the layout of the problem and the assumptions of material properties in Section 3.2. The soil-pavement structure is modeled as a layered system. Each layer is considered to be isotropic, homogeneous and linearly viscoelastic. Fourier superposition technique is discussed in Section 3.3. It can be applied to both the time variable t and the spatial coordinate y so that a time- and space-dependent problem can be transformed into a domain which is independent of time t and coordinate y. The formulation of the stiffness matrices for core region, lateral regions, and bottom boundary are described in Sections 3.4, 3.5, and 3.6, respectively. Section 3.7 discusses the formulation for point and disk loads. The computer implementation is outlined in Section 3.8. Finally, a summary is included in Section 3.9.

3.2 Layout of the Problem

In a system of rectangular Cartesian coordinates (x, y, z), Figure 3.2 depicts an idealized pavement system which is surrounded by soil. The soil-pavement system is considered to be a horizontally layered stratum of depth H resting over a rigid rock or a half space. The core region has finite width B in the x-direction (transverse direction) while it extends to infinity in the y-direction (longitudinal direction). It is assumed that the lateral regions extend to infinity in both the x- and y-directions. In all the regions, each layer is considered isotropic, homogeneous, and linearly viscoelastic. Thus, for a dynamic problem, four parameters are needed to characterize the material properties: the mass density ρ, the Lamé moduli λ and G, and the damping ratio D. Some other material constants can be derived from these four basic parameters as follows:

$$\nu = \frac{\lambda}{2(\lambda + G)} \tag{3.1}$$

$$E = \frac{G(3\lambda + 2G)}{\lambda + G} \tag{3.2}$$

$$M = \lambda + 2G \tag{3.3}$$

$$Cs = \sqrt{\frac{G}{\rho}} \tag{3.4}$$

$$Cp = \sqrt{\frac{\lambda + 2G}{\rho}} \tag{3.5}$$

in which

ν = Poisson's ratio,

E = Young's modulus,

M = the constrained modulus,

Cs = the shear wave velocity, and

Cp = the compression wave velocity.

It should be noted that the Lamé moduli λ and G are real numbers for a linearly elastic solid. However, for a linearly viscoelastic solid, they are specified as complex-valued functions of the frequency ω, which depend on the type of internal dissipation of energy in the material. For a linear viscous material, the energy loss per cycle increases linearly with frequency. Hysteretic damping, on the other hand, produces an energy loss per cycle that is frequency independent, but depends on amplitude of the strains. For low-strain amplitudes, damping can be considered to be independent of strain (Hardin and Drnevich, 1972; Johnston *et al*, 1979; Toksöz *et al*, 1979). In order to maintain the linearity of the solution, the amplitude dependence is dropped, using what is normally called linear hysteretic damping. In this case, the complex Lamé moduli are given by

$$\lambda^c = \lambda\,(1 + i2D), \qquad G^c = G\,(1 + i2D) \tag{3.6}$$

where λ and G are the moduli of the corresponding linearly elastic solid and $i = \sqrt{-1}$. Since the differential equations which must be satisfied by a time-harmonic displacement field in a linearly elastic solid are formally the same as those in a linear viscoelastic material, derivations are made for linear viscoelastic solids only. If the results are desired for a linearly elastic material, the damping ratio D is set equal to zero. For the reason cited above, the superscript "c" will be dropped in what follows, since no confusion should occur.

3.3 Fourier Superposition Analysis

One of several methods to study wave propagation phenomena in a linear viscoelastic medium is by the superposition of the response to steady-state harmonic excitations. The method, known as Fourier superposition, provides an easy way to study complicated transient events when the solution to the steady-state problem is known. It should be noted that the use of superposition techniques is limited to linear systems.

Consider a medium with an arbitrary shape as shown in Figure 3.3a. The objective of the analysis is to obtain the time history of particle displacement u(t) that would be recorded by a receiver at a point B due to an arbitrary excitation p(t) applied at a point A.. As a first step in the Fourier superposition method, the excitation p(t) is decomposed into its different frequency components $P(\omega)$by means of a forward Fourier transform (Figure 3.3b) :

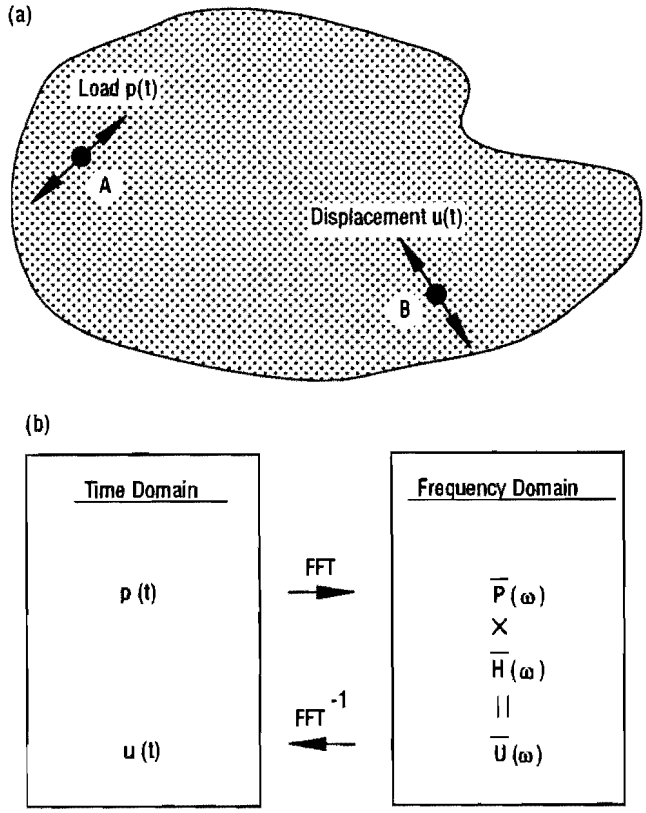

Figure 3.3 Illustration of the use of Fourier Superposition Analysis

$$\bar{P}(\omega) = \int_{-\infty}^{+\infty} p(t)\, e^{-i\omega t}\, dt \tag{3.7}$$

This also implies that

$$p(t) = \frac{1}{2\pi} \int_{-\infty}^{+\infty} \bar{P}(\omega)\, e^{i\omega t}\, d\omega \tag{3.8}$$

In these expressions, the symbol t is the time variable in seconds, ω is the angular frequency in rad/sec, and e is the base of natural logarithms. The two integrals in Eqs. (3.7) and (3.8) are known as a Fourier transform pair.

The second step is to obtain the transfer function $H(\omega)$ defined as the response of the medium due to a unit disturbance. Both the response and disturbance can be any quantity of interest, such as displacement, stress, strain, etc. In our case, $H(\omega)$ is the displacement of point B due to a harmonic unit load at point A. (In this case, it can be called also a flexibility function.)

The third step is to obtain the Fourier transform of the displacement, $U(\omega)$, by multiplying the Fourier transform of the force by the transfer function. That is,

$$\bar{U}(\omega) = \bar{H}(\omega) \times \bar{P}(\omega) \tag{3.9}$$

Finally, the time history of particle motion u(t) can be recovered through an inverse Fourier transform

$$u(t) = \frac{1}{2\pi} \int_{-\infty}^{+\infty} \bar{U}(\omega)\, e^{i\omega t}\, d\omega \tag{3.10}$$

To make practical use of the frequency domain method described above, it is necessary to formulate the Fourier transform pair Eqs. (3.7) and (3.8) so that they can be calculated numerically. A discrete Fourier transform (DFT) expression is therefore derived with the assumption that the input function is periodic with period T_p in order to replace the infinite time integral with a finite sum. Therefore Eqs. (3.7) and (3.8) become

$$\bar{P}(\omega_n) = \Delta t \sum_{j=0}^{N-1} p(t_j)\, e^{-(2\pi i \frac{n_j}{N})}, \quad n = 0, 1, \cdots, N-1 \tag{3.11}$$

$$p(t_j) = \frac{\Delta\omega}{2\pi} \sum_{n=0}^{N-1} \bar{P}(\omega_n)\, e^{(2\pi i \frac{n_j}{N})}, \quad j = 0, 1, \cdots, N-1 \tag{3.12}$$

in which

N = number of sampling points,

$t_j = j\,\Delta t$,

$\Delta t = \frac{T_p}{N}$,

$\omega_n = n\,\Delta\omega$,

$\Delta\omega = \frac{2\pi}{T_p}$.

The Fast Fourier transform (FFT) is an efficient method for evaluating DFT based on the numerical algorithm proposed by Cooley and Tukey (1965). Details on Fourier transform theory and FFT algorithms can be found in Bracewell (1965) and Brigham (1974). In using DFT or FFT, the values of the basic parameters involved (e. g., number of sampling points N, time increment Δt and period T_p) have to be properly selected such that a compromise can be reached between the accuracy of results and the cost of computation.

Before proceeding, it is useful to mention that the Fourier transform technique is not restricted to time-dependent functions only. It applies equally well to many other problems as long as the system is linear. For time functions, the unit of (temporal) frequency is Hertz (cycles per second) and the common symbol is f. Related quantities are the period T_p (= 1/f), and the angular frequency ω (= $2\pi f$). If the primary variable for transformation is a spatial coordinate, that is a distance, then the frequency will be in units of cycles per distance, and is called spatial frequency as opposed to temporal frequency. The parallel quantity to angular frequency is the wavenumber, often indicated by the symbol k or m. Thus, a space-dependent problem can be transformed to its corresponding wavenumber domain. After the solution for each wavenumber is obtained, the spatial response can be recovered by performing an inverse Fourier transform. Finally, for a time- and space-dependent problem such as the one considered in this study, the transform pair can be represented by

$$\hat{P}(x, z, m, \omega) = \int_{-\infty}^{+\infty}\int_{-\infty}^{+\infty} p(x, z, y, t)\ e^{-i(\omega t - my)}\, dt\, dy \tag{3.13}$$

$$p(x, z, y, t) = \frac{1}{4\pi^2}\int_{-\infty}^{+\infty}\int_{-\infty}^{+\infty} \hat{P}(x, z, m, \omega)\, e^{i(\omega t - my)}\, d\omega\, dm \tag{3.14}$$

where the Fourier transform is applied to the time variable t as well as the spatial variable y.

The time history of displacement u (x, z, y, t) at any point (x, y, z) can then be written as

$$u(x, z, y, t) = \frac{1}{4\pi^2}\int_{-\infty}^{+\infty}\int_{-\infty}^{+\infty} \hat{U}(x, z, m, \omega)\, e^{i(\omega t - my)}\, d\omega\, dm \tag{3.15}$$

in which the displacement $U(x,z,m,\omega)$ can be obtained by

$$\hat{U}(x, z, m, \omega) = \hat{H}(x, z, m, \omega) \times \hat{P}(x, z, m, \omega) \tag{3.16}$$

In this expression, $H(x,z,m,\omega)$ is the transfer function in the frequency-wavenumber domain. Instead of keeping the term $H(x,z,m,\omega)$ in the right-hand side, Eq. (3.16) can be rewritten as

$$\hat{S}(x, z, m, \omega) \times \hat{U}(x, z, m, \omega) = \hat{P}(x, z, m, \omega) \tag{3.17}$$

where the function $S(x,z,m,\omega)$ is the inverse of $H(x,z,m,\omega)$ and can be called the stiffness function. Similarly, in a discrete system, the nodal displacements and nodal forces can be related as follows:

$$\hat{S}\,\hat{U} = \hat{P} \tag{3.18}$$

where $\boldsymbol{S}$ is the dynamic stiffness matrix and $\boldsymbol{P}$ is the load vector. In the Fourier analysis, one may find that most of the difficulty lies in the determination of the stiffness matrices (or functions). Once the stiffness matrices are obtained, the rest of the analysis is rather straightforward. Therefore, in the following sections, emphasis will be placed on the derivation of the stiffness matrices. The formulation of the load vector will be described in Section 3.7.

3.4 Formulation of Core Region

In this section, the formulation of the stiffness matrix for the core region is presented. It starts with the discretization of the core region by finite elements, as shown in Figure 3.4. Various types of solid elements in a three-dimensional space can be used. Consider a generic finite element herein. The element is characterized by its dimensions Δx, Δy, and Δz and n nodes. Each node has three degrees of freedom: U_i, V_i, and W_i. By assuming the displacement shape functions, the relationships between generic displacements and nodal displacements can be written as follows

$$\begin{aligned} u(x,z,y,t) &= \sum_{i}^{n} f_i\ U_i \\ v(x,z,y,t) &= \sum_{i}^{n} f_i\ V_i \\ w(x,z,y,t) &= \sum_{i}^{n} f_i\ W_i \end{aligned} \tag{3.19}$$

where u, v, w are the generic displacements at any point of the element in the x-, y-, z-directions and f_i is the shape function for node i. In matrix notation, it can be written as

$$\boldsymbol{u}(x,z,y,t) = \boldsymbol{N}\ \boldsymbol{U} \tag{3.20}$$

where the matrix $\boldsymbol{N}$ of dimension (3x3n) contains the shape functions and the vector $\boldsymbol{U}$ contains nodal displacements in the element. By applying the principle of virtual work (see Appendix A for more details), it is possible to write the equilibrium equation for a harmonic motion at frequency ω as

$$\bar{\boldsymbol{s}}\ \bar{\boldsymbol{U}} = \bar{\boldsymbol{P}} \tag{3.21}$$

where $\boldsymbol{s}$ denotes the dynamic stiffness matrix of the element and $\boldsymbol{P}$ represents the nodal forces.

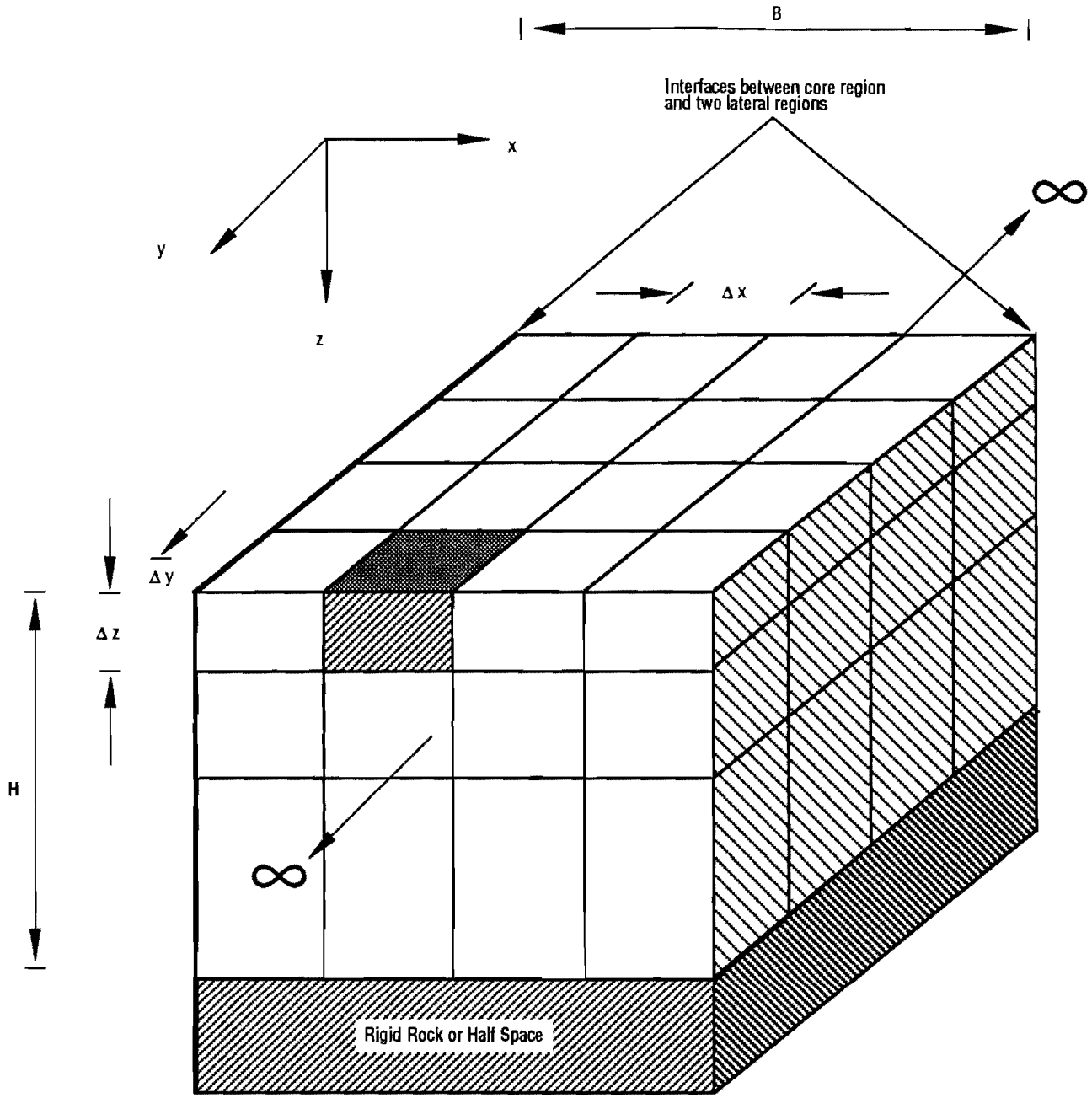

Figure 3.4 Discretization of the core region

For the purpose of performing Fourier transform in the y-direction, it is convenient to partition the dynamic stiffness matrix $\boldsymbol{s}$ into four submatrices. Thus, the matrix $\boldsymbol{s}$ is written as

$$\bar{\boldsymbol{s}} = \begin{bmatrix} \bar{\boldsymbol{s}}_{11} & \bar{\boldsymbol{s}}_{12} \\ \bar{\boldsymbol{s}}_{21} & \bar{\boldsymbol{s}}_{22} \end{bmatrix} \tag{3.22}$$

in which the subscripts "1" and "2" denote the degrees of freedom on the positive face and on the negative face in the y-direction, respectively (Figure 3.5a). Assembling the dynamic

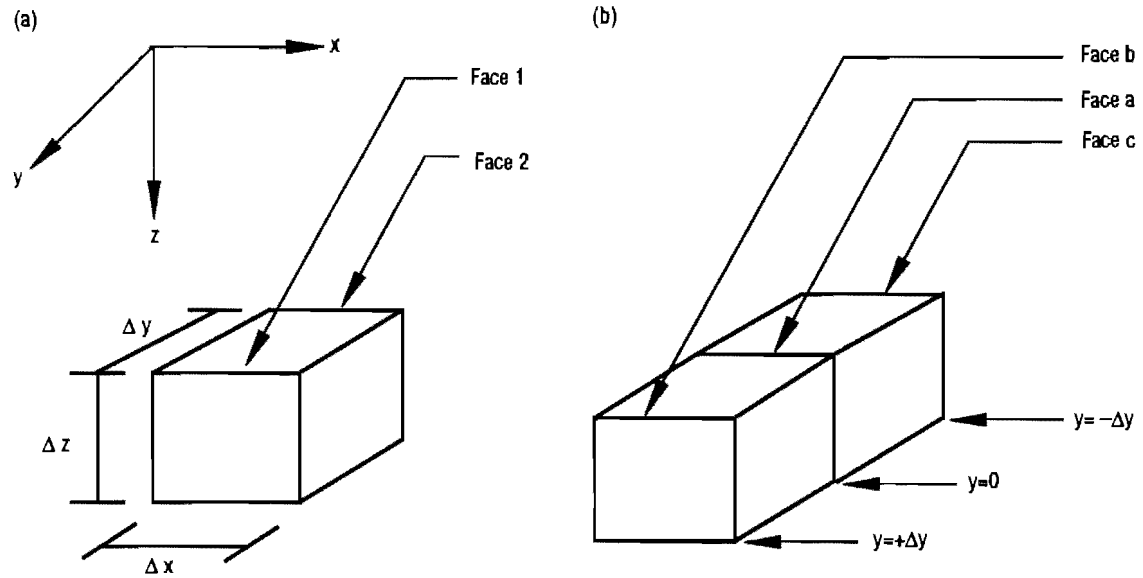

Figure 3.5 Assembly in the element level

stiffness matrices of two adjacent finite elements in the y-direction (Figure 3.5b), one can write

$$\begin{bmatrix} \bar{s}_{11} & \bar{s}_{12} & 0 \\ \bar{s}_{21} & \bar{s}_{11}+\bar{s}_{22} & \bar{s}_{12} \\ 0 & \bar{s}_{21} & \bar{s}_{22} \end{bmatrix} \begin{Bmatrix} \bar{U}_b \\ \bar{U}_a \\ \bar{U}_c \end{Bmatrix} = \begin{Bmatrix} \bar{P}_b \\ \bar{P}_a \\ \bar{P}_c \end{Bmatrix} \tag{3.23}$$

where

"a" denotes the degrees of freedom on face a (i.e. at y=0),

"b" denotes the degrees of freedom on face b (i.e. at y= +Δy), and

"c" denotes the degrees of freedom on face c (i.e. at y= −Δy).

Let $\boldsymbol{U}(m)$ and $\boldsymbol{P}(m)$ be the Fourier transforms of $\boldsymbol{U}(y)$ and $\boldsymbol{P}(y)$ with respect to the coordinate y. That is

$$\hat{\boldsymbol{U}}(m) = \int_{-\infty}^{+\infty} \bar{\boldsymbol{U}}(y)\, e^{imy}\, dy$$

$$\hat{\boldsymbol{P}}(m) = \int_{-\infty}^{+\infty} \bar{\boldsymbol{P}}(y)\, e^{imy}\, dy \tag{3.24}$$

where m is the wavenumber (circular spatial frequency) corresponding to the coordinate y. By applying the Fourier transform to both sides of Eq. (3.23), the following relationship is obtained:

$$\begin{bmatrix} \bar{\boldsymbol{s}}_{11} & \bar{\boldsymbol{s}}_{12} & \boldsymbol{0} \\ \bar{\boldsymbol{s}}_{21} & \bar{\boldsymbol{s}}_{11}+\bar{\boldsymbol{s}}_{22} & \bar{\boldsymbol{s}}_{12} \\ \boldsymbol{0} & \bar{\boldsymbol{s}}_{21} & \bar{\boldsymbol{s}}_{22} \end{bmatrix} \begin{Bmatrix} \hat{\boldsymbol{U}}_b(m) \\ \hat{\boldsymbol{U}}_a(m) \\ \hat{\boldsymbol{U}}_c(m) \end{Bmatrix} = \begin{Bmatrix} \hat{\boldsymbol{P}}_b(m) \\ \hat{\boldsymbol{P}}_a(m) \\ \hat{\boldsymbol{P}}_c(m) \end{Bmatrix} \tag{3.25}$$

The displacements $\boldsymbol{U}_b(m)$ and $\boldsymbol{U}_c(m)$ can be written as

$$\hat{\boldsymbol{U}}_b(m) = \hat{\boldsymbol{U}}_a(m)\, e^{-im\Delta y}$$

$$\hat{\boldsymbol{U}}_c(m) = \hat{\boldsymbol{U}}_a(m)\, e^{+im\Delta y} \tag{3.26}$$

Substituting Eq. (3.26) into Eq. (3.25), one can write

$$\hat{\boldsymbol{s}}(m)\, \hat{\boldsymbol{U}}_a(m) = \hat{\boldsymbol{P}}_a(m) \tag{3.27}$$

where

$$\hat{\boldsymbol{s}}(m) = \bar{\boldsymbol{s}}_{21}\, e^{-im\Delta y} + (\bar{\boldsymbol{s}}_{11}+\bar{\boldsymbol{s}}_{22}) + \bar{\boldsymbol{s}}_{12}\, e^{+im\Delta y} \tag{3.28}$$

It is interesting to note that through this transformation, the dynamic stiffness matrix $\boldsymbol{s}(m)$ is a function of the wavenumber m. One can consider the matrix $\boldsymbol{s}(m)$ as the stiffness matrix of a strip element which extends to infinity in the y-direction and which relates exclusively the nodal displacements in the x-z plane due to the nodal forces in this plane. In

this way, it is possible to reduce a three-dimensional problem to a series of two-dimensional ones. Thus one can consider only the x-z plane in the rest of formulation.

Before proceeding, it is worthwhile to discuss the types of finite elements which were used in this study. Basically, there is no restriction on what type of element can be incorporated in the formulation. The condensation of the stiffness matrix described above assumes a linear variation of displacements in the y-direction. On the other hand, one can assume either linear, quadratic, or even high order variation of the displacements in the x- and z-directions. The main concern in selecting an element was the trade off between computational time and the sensitivity of the element to the changes of its dimensions (Δx, Δy, and Δz). For example, usually the top layer of a pavement system is very thin compared with the width of the pavement. Therefore, one should select an element which will provide accurate result for a large ratio of $\Delta x/\Delta z$. On the other hand, for the deeper layers, one may want to enlarge Δz (that is, small ratio $\Delta x/\Delta z$) so that less layers are needed and therefore the computational time can be reduced effectively.

For the reasons above, four types of element were derived and studied. They are called "SOLID8," "SOLID12A," "SOLID12B," and "SOLID16" (see Figure 3.6). Detailed derivation is included in Appendix A. Parametric studies of the performance of these elements will be discussed in Chapter Four.

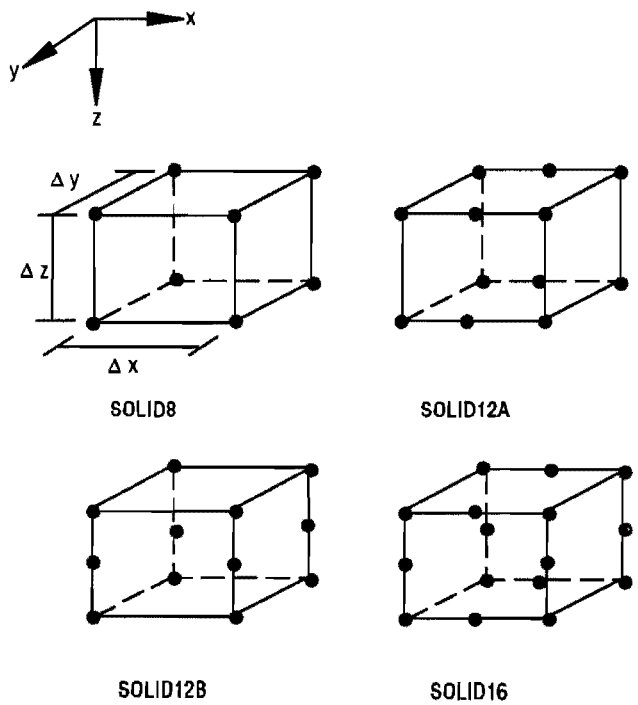

Figure 3.6 Four types of finite elements

3.5 Formulation of Lateral Region

As explained in Section 3.1, it is necessary to formulate a transmitting boundary such that its effect on the core region is equivalent to that of an infinite lateral region. Consider a layered stratum overlaying a rigid rock or a half space (Figure 3.7). The lateral region is semi-infinite in the x-direction and infinite in the y-direction. Again the stratum is discretized by finite elements. In principle, the technique used to obtain the stiffness matrix for the core region can be applied here to the lateral region. However, since the lateral region extends to infinity in the horizontal directions, special care has to be taken through the following levels.

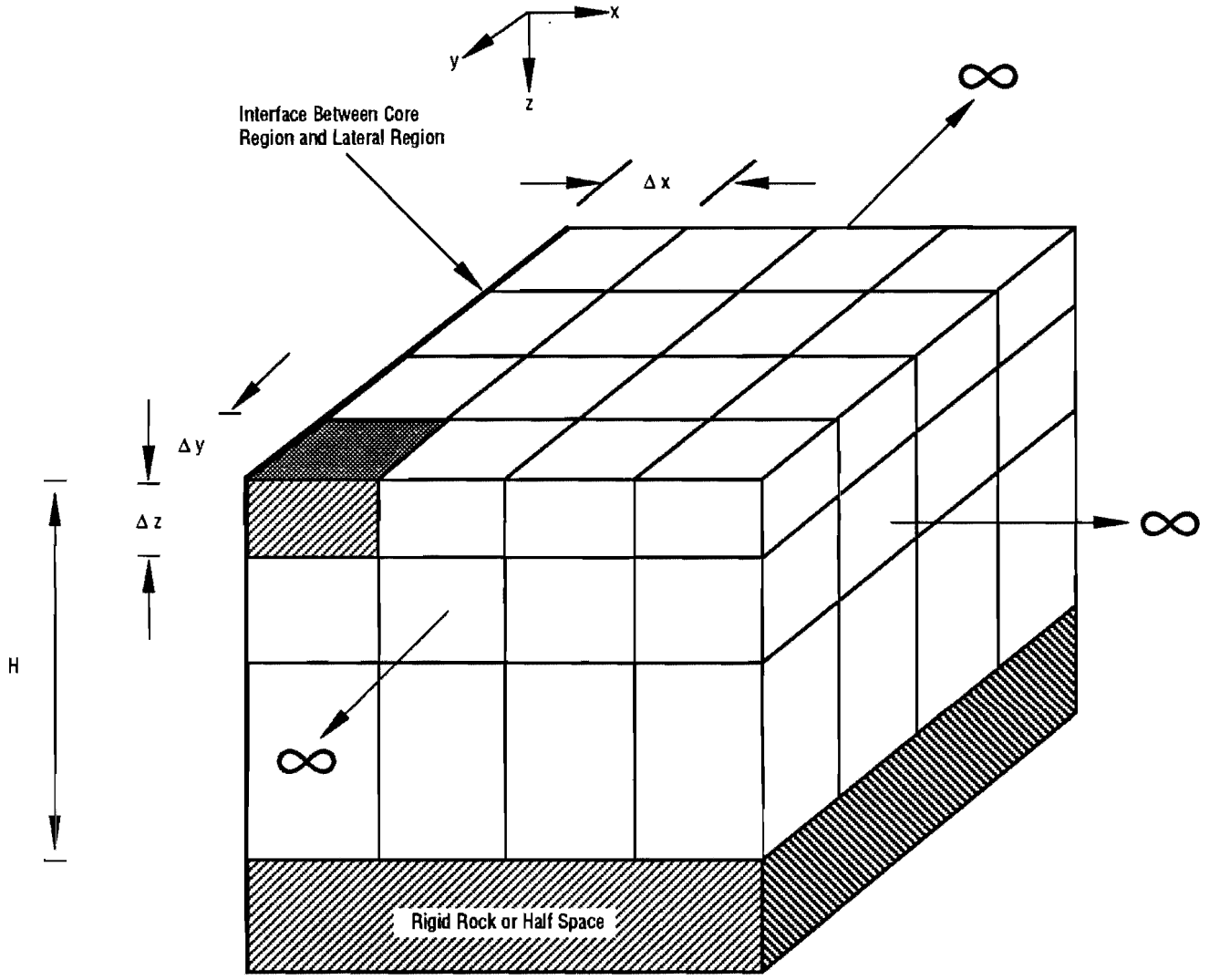

Figure 3.7 Discretization of the lateral region

3.5.1 Element Level

Each element has dimensions Δx, Δy, and Δz. Starting from the stiffness matrix $\boldsymbol{s}$ (Eq. 3.21), one can obtain the stiffness matrix $\boldsymbol{s}$ (Eq. 3.28) in the wavenumber domain.

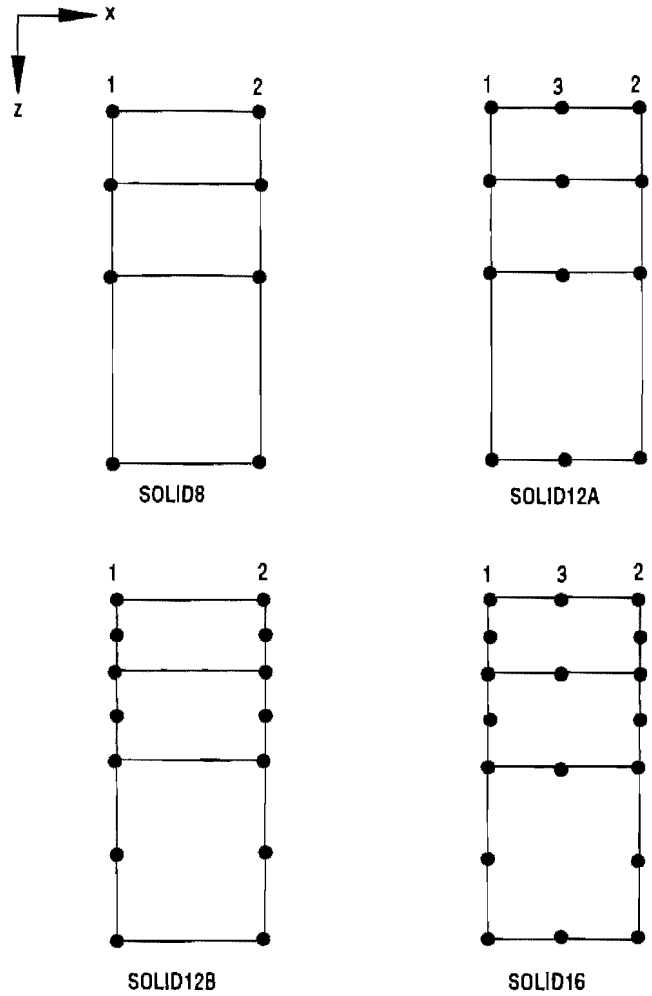

Figure 3.8 Four types of soil columns

3.5.2 Column Level

Once the stiffness matrix $\hat{\boldsymbol{S}}(m)$ is obtained, one can assemble these matrices into a matrix $\boldsymbol{S}(m)$ which will represent the stiffness matrix for a soil column. Depending on the type of element adopted, one may end up with different types of soil columns (see Figure 3.8). For elements SOLID8 and SOLID12B, there are two vertical nodal arrays which are denoted by numbers "1" and "2." For elements SOLID12A and SOLID16, there will be one additional mid-array denoted by number "3." Since there are no external loads acting at the mid-array, it is possible to eliminate these degrees of freedom by condensation. First, the matrix $\boldsymbol{S}(m)$ can be rearranged and partitioned as follows:

$$\hat{\boldsymbol{S}}(m) = \left[\begin{array}{cc|c} \hat{\boldsymbol{S}}_{11} & \hat{\boldsymbol{S}}_{12} & \hat{\boldsymbol{S}}_{13} \\ \hat{\boldsymbol{S}}_{21} & \hat{\boldsymbol{S}}_{22} & \hat{\boldsymbol{S}}_{23} \\ \hline \hat{\boldsymbol{S}}_{31} & \hat{\boldsymbol{S}}_{32} & \hat{\boldsymbol{S}}_{33} \end{array}\right] \tag{3.29}$$

By eliminating the third nodal array, a new matrix $\tilde{S}(m)$ can be obtained as

$$\tilde{S}(m) = \begin{bmatrix} \hat{S}_{11} & \hat{S}_{12} \\ \hat{S}_{21} & \hat{S}_{22} \end{bmatrix} - \begin{bmatrix} \hat{S}_{31} & \hat{S}_{32} \end{bmatrix} \begin{bmatrix} \hat{S}_{33} \end{bmatrix}^{-1} \begin{Bmatrix} \hat{S}_{13} \\ \hat{S}_{23} \end{Bmatrix} \tag{3.30}$$

Therefore, at the column level, one will obtain a matrix $\tilde{S}(m)$ which contains only arrays 1 and 2 for all types of elements. Figure 3.9a shows a generic soil column which can be characterized by its stiffness matrix $\tilde{S}(m)$. One can simply write $\tilde{S}(m)$ as

$$\tilde{S}(m) = \begin{bmatrix} \tilde{S}_{11} & \tilde{S}_{12} \\ \tilde{S}_{21} & \tilde{S}_{22} \end{bmatrix} \tag{3.31}$$

Notice that the only difference in the matrix $\tilde{S}(m)$ due to the different types of element is its size. For SOLID8 and SOLID12A, each nodal array contains (N+1) nodes, N being the number of layers in the stratum. While for SOLID12B and SOLID16, there will be (2xN+1) nodes

3.5.3 Expansion Level

By assembling two adjacent soil columns in the x-direction (Figure 3.9b), it is possible to write the following relationship:

$$\begin{bmatrix} \tilde{S}_{11} & \tilde{S}_{12} & 0 \\ \tilde{S}_{21} & \tilde{S}_{22}+\tilde{S}_{11} & \tilde{S}_{12} \\ 0 & \tilde{S}_{21} & \tilde{S}_{22} \end{bmatrix} \begin{Bmatrix} \tilde{U}_a \\ \tilde{U}_b \\ \tilde{U}_c \end{Bmatrix} = \begin{Bmatrix} \tilde{P}_a \\ \tilde{P}_b \\ \tilde{P}_c \end{Bmatrix} \tag{3.32}$$

where subscripts "a," "b," and "c" denote three nodal arrays in Figure 3.9b. Eliminating again array b by condensation, Eq. (3.32) can be rewritten as

$$\begin{bmatrix} \vec{S}_{11} & \vec{S}_{12} \\ \vec{S}_{21} & \vec{S}_{22} \end{bmatrix} \begin{Bmatrix} \vec{U}_a \\ \vec{U}_c \end{Bmatrix} \quad \begin{Bmatrix} \vec{P}_a \\ \vec{P}_c \end{Bmatrix} \tag{3.33}$$

where

$$\vec{S}_{11} = \tilde{S}_{11} - \tilde{S}_{12}(\tilde{S}_{11} + \tilde{S}_{22})^{-1}\tilde{S}_{21} \tag{3.34}$$

$$\vec{S}_{12} = -\tilde{S}_{12}(\tilde{S}_{11} + \tilde{S}_{22})^{-1}\tilde{S}_{12} \tag{3.35}$$

$$\vec{S}_{21} = -\tilde{S}_{21}(\tilde{S}_{11} + \tilde{S}_{22})^{-1}\tilde{S}_{21} \tag{3.36}$$

$$\vec{S}_{22} = \tilde{S}_{22} - \tilde{S}_{21}(\tilde{S}_{11} + \tilde{S}_{22})^{-1}\tilde{S}_{12} \tag{3.37}$$

After this process, one will obtain a new stiffness matrix $\boldsymbol{S}(m)$ for a region with width equal to $2\Delta x$ (Figure 3.9c). Repeating this process by using Eqs.(3.34) through (3.37), the width of the region will grow with increments $4\Delta x$, $8\Delta x$, $16\Delta x$, and so on. Table 3.1 shows the relationship between the number of cycles N_x and the width of the region T_x. It can be seen that just after a few cycles, the width of the region may be considered as infinitely large by providing some material damping (even as little as one percent) to the soil stratum. Then, this final stiffness matrix $\boldsymbol{S}(m)$ can be used to replace the infinite lateral region.

Notice that the expansion process can be also applied to the core region, especially for a pavement system, which can be reasonably modeled as a horizontally layered system. A simple example is illustrated in Figure 3.10a where a load is applied on the surface of the core region at a distance of $2\Delta x$ measured from the left interface and at a distance of $4\Delta x$ from the right. To solve the problem, one can start from the stiffness matrix of a pavement column (Figure 3.10b). Through applying the expansion process once, one can obtain the stiffness matrix for the left core region (Figure 3.10c), while for the right core region, the expansion process would be performed twice.(Figure 3.10d).

The advantage of using the expansion technique for the core region is that less computation time is needed to obtain the global stiffness, especially when the dimension of the core region in the x-direction is relatively large compared with the dimension in the z-direction. However, a disadvantage of using this technique is that the intermediate nodal arrays are removed from the process during the condensation. Therefore, the displacements at these nodes are not obtained directly. For almost all the cases of nondestructive testings, this does not impose any additional computations, since only the displacements along the traffic direction (i.e. the y-direction) at the x corresponding to the application of the load are of interest.

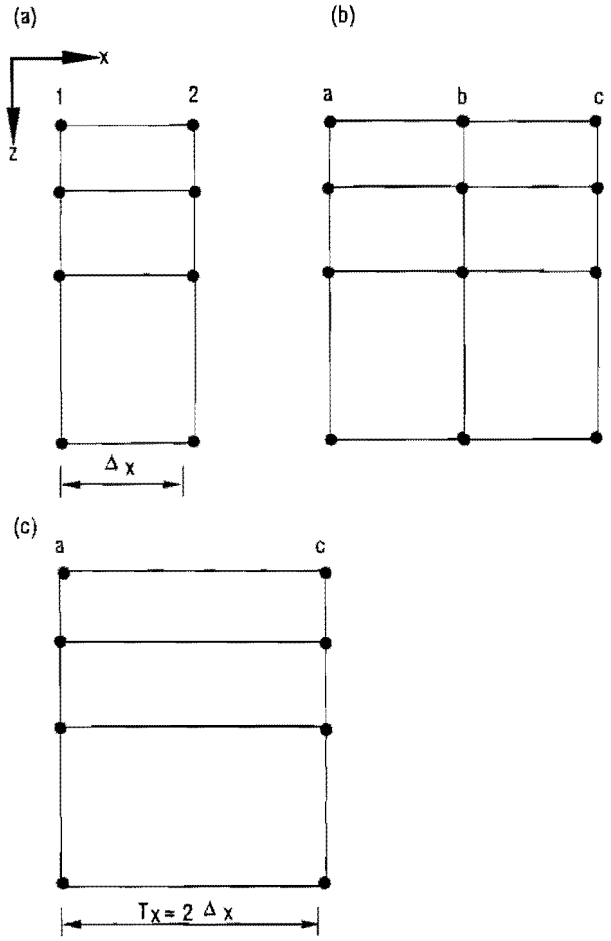

Figure 3.9 Illustration of the expansion level

Table 3.1 Relation between the number of cycles N_x and the total width T_x

N_x	T_x
1	2 Δx
2	4 Δx
4	16 Δx
6	64 Δx
8	256 Δx
10	1024 Δx

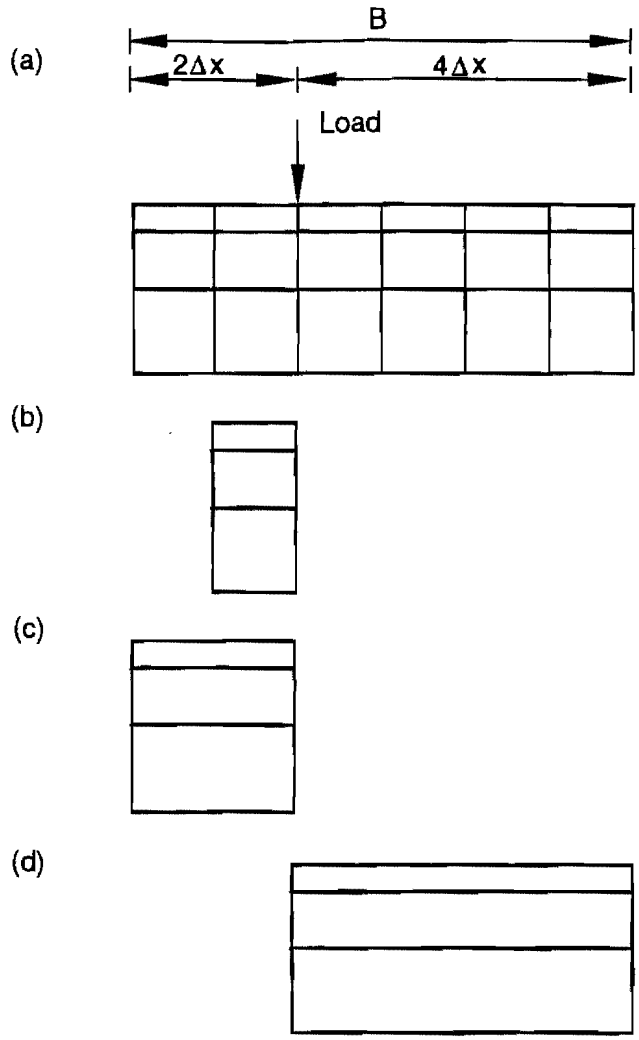

Figure 3.10 Example of the expansion process for the core region

3.6 Formulation of Bottom Boundary

Two types of bottom boundary are usually encountered in the modelling. One is much stiffer, nearly rigid rock and the other a homogeneous half space. For the rigid rock case, it is assumed that all the degrees of freedom at the bottom of the stratum are fixed. Therefore, it is quite simple to implement this condition by removing all the degrees of freedom at the bottom from the system of equations. Notice that the degrees of freedom at the bottom for a soil (or pavement) column should be removed before performing the expansion process.

To model the half space, a viscous boundary corresponding to the assumption of a vertically propagating wave is used herein. This type of boundary is viscous because it assumes that stresses can be expressed in terms of velocities, as

$$\sigma = \rho C_p \dot{w}$$
$$\tau = \rho C_s \dot{u} \tag{3.38}$$

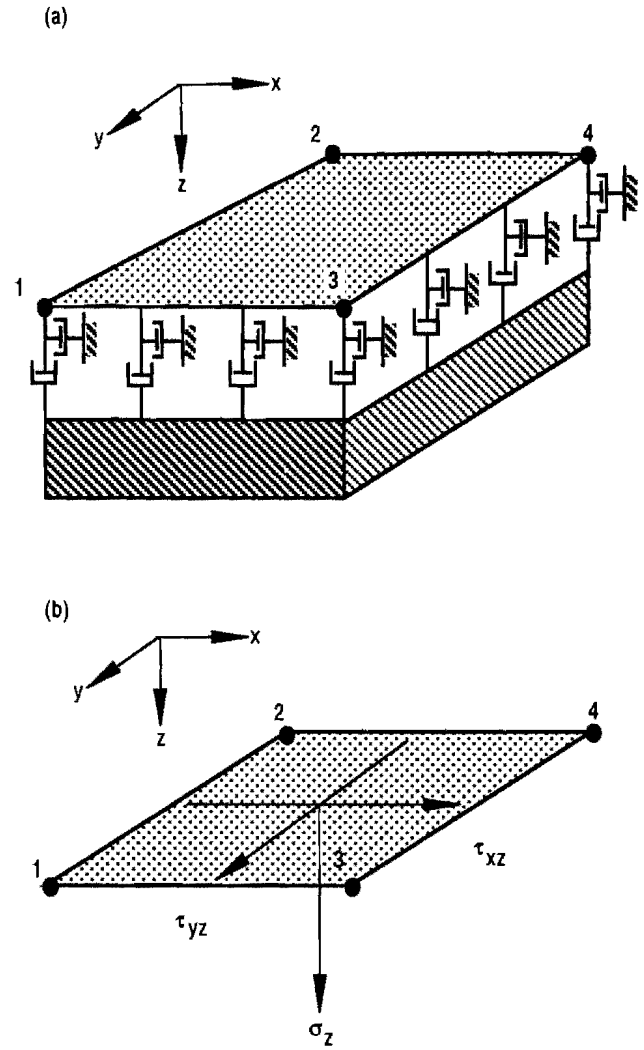

Figure 3.11 Viscous bottom boundary

where σ and τ are the normal and shear stress, respectively; w and u are the normal and tangential velocities. Therefore, in this method, the boundary is replaced by infinitesimal dashpots oriented normal and tangential to the boundary. Consider a generic finite element supported by dashpots at its bottom (Figure 3.11a). The characteristics of each dashpot can be expressed as (Figure 3.11b)

$$\begin{aligned} \tau_{xz} &= \rho C_s \dot{u}, \\ \tau_{yz} &= \rho C_s \dot{v}, \\ \sigma_z &= \rho C_p \dot{w}, \end{aligned} \tag{3.39}$$

or for a harmonic motion,

$$\begin{aligned} \bar{\tau}_{xz} &= i\omega\rho C_s \bar{u}, \\ \bar{\tau}_{yz} &= i\omega\rho C_s \bar{v}, \\ \bar{\sigma}_z &= i\omega\rho C_p \bar{w}. \end{aligned} \tag{3.40}$$

In matrix notation, Eq. (3.40) can be expressed as

$$\bar{\boldsymbol{T}} = i\omega\rho \boldsymbol{C}\, \bar{\boldsymbol{u}} \tag{3.41}$$

where

the vector $\bar{\boldsymbol{T}} = \begin{Bmatrix} \bar{\tau}_{xz} \\ \bar{\tau}_{yz} \\ \bar{\sigma}_z \end{Bmatrix}$, and

the matrix $\boldsymbol{C} = \begin{bmatrix} C_s & 0 & 0 \\ 0 & C_s & 0 \\ 0 & 0 & C_p \end{bmatrix}$.

The equivalent nodal forces can then be written as

$$\bar{\boldsymbol{P}} = \int_A \boldsymbol{N}^T \bar{\boldsymbol{T}}\, dA \tag{3.42}$$

in which the integral is evaluated over the bottom area of the element. Substituting Eq. (3.41) into Eq. (3.42), it yields

$$\bar{\boldsymbol{P}} = \bar{\boldsymbol{S}}_b\, \bar{\boldsymbol{U}} \tag{3.43}$$

where

$$\bar{\boldsymbol{S}}_b = i\omega\rho \int_y \int_x \boldsymbol{N}^T \boldsymbol{C}\, \boldsymbol{N}\, dx\, dy \tag{3.44}$$

Notice that matrix $\boldsymbol{s}_b$ is the dynamic stiffness matrix in the space domain. Once the matrix $\boldsymbol{s}_b$ is obtained, it can be treated as an ordinary stiffness matrix. One can get the corresponding stiffness matrix $\boldsymbol{s}_b$ in the wavenumber domain by using Eq. (3.28). Then it can

be assembled together with those of the finite elements to form the stiffness matrix for a soil (or pavement) column. The expansion technique can be applied to get the stiffness matrix either for the core region or lateral region with the viscous boundary acting at the bottom.

In this section, the derivation of the stiffness matrices for the core region, lateral regions and bottom boundary has been discussed. These matrices can then be assembled into a global matrix $\boldsymbol{s}$ (Eq. 3.18).

3.7 Formulation of Point Load and Disk Load Vectors

As mentioned in Section 3.3, for a time- and space-dependent problem it is necessary to transform the excitation load p(x, z, y, t) into its corresponding components in the frequency-wavenumber domain so that the system of equations (Eq. 3.18) can be solved for each frequency and wavenumber. The transformation from time domain to frequency domain is straightforward. Therefore, the discussion will concentrate on the transformation from the space domain to the wavenumber domain.

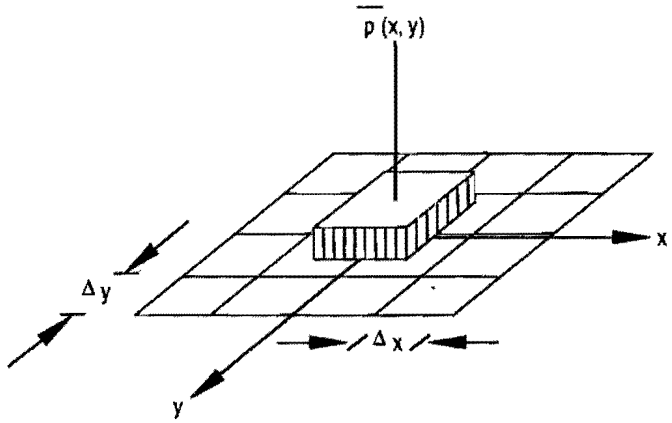

Figure 3.12 Distributed load in the space domain

In order to visualize the transformation of the load vector, an example is given here. Figure 3.12 shows an arbitrary excitation load P(x,y) acting on the surface of the pavement. The equivalent nodal forces $\boldsymbol{P}$ can be found by using

$$\overline{\boldsymbol{P}} = \int_y \int_x \boldsymbol{N}^T \, \bar{p} \, dx \, dy \tag{3.45}$$

where matrix $\boldsymbol{N}$ contains shape functions of the discrete model. In this example, nine non-zero nodal forces can be seen in Figure 3.13. All the nodal forces acting at $x = -\Delta x$ can be grouped as vector $\boldsymbol{P}_{-1}(y)$ as shown in Figure 3.13. Then through the Fourier transform, one can get the load vector $\boldsymbol{P}_{-1}(m)$ as shown in Figure 3.14. The same process can be repeated for the load vectors $\bar{\boldsymbol{P}}_0(y)$ and $\bar{\boldsymbol{P}}_{+1}(y)$. Two types of loads are found to be useful for nondestructive testing: a point load and a circular disk load.

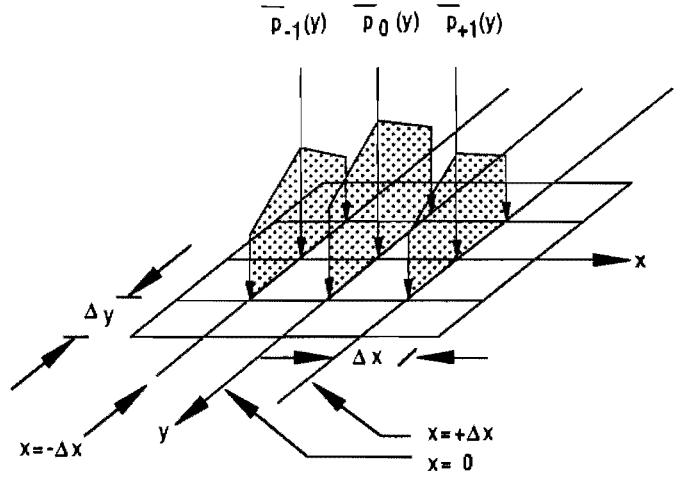

Figure 3.13 Equivalent nodal loads in the space domain

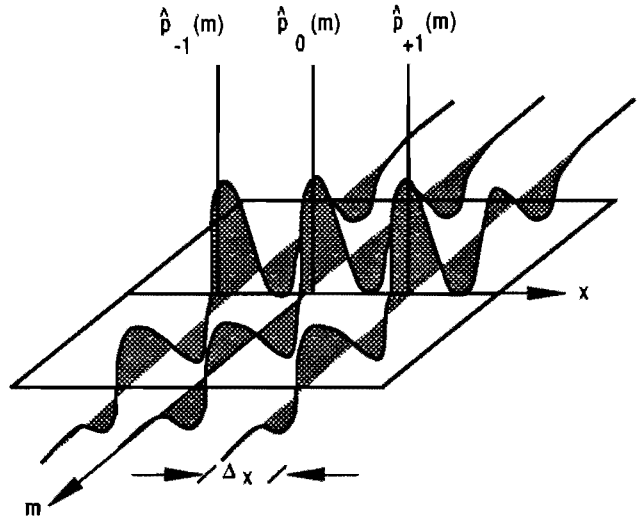

Figure 3.14 Equivalent nodal loads in the wavenumber domain

3.7.1 Point Load

Figure 3.15a depicts a harmonic point load acting on the surface. In the discrete model, it is a concentrated nodal force acting at the central node of the four surrounding elements. Therefore, the only non-zero load vector will be the one acting at x = 0. For a point load vector, its transform will be constant over all wavenumbers (Figure 3.15b).

3.7.2 Circular Disk Load

For a uniform circular disk load with radius R, the equivalent nodal

$$\bar{\boldsymbol{P}} = \int_{0^0}^{360^0} \int_0^R \boldsymbol{N}^T \bar{p}\, r\, dr\, d\theta \tag{3.46}$$

where $\bar{P}$ is the uniform distributed load equal to P ÷ (πR^2), P being the total load. Figure 3.16 illustrates a case where the disk is smaller than the four surrounding elements. With linear shape functions assumed, the equivalent nodal forces can be found as

$$\bar{P}_1 = \bar{P}_3 = \bar{P}_7 = \bar{P}_9 = \frac{\bar{p} R^4}{16\Delta x \Delta y}$$

$$\bar{P}_2 = \bar{P}_4 = \bar{P}_6 = \bar{P}_8 = \frac{2\bar{p} R^3}{3\Delta x} - \frac{\bar{p} R^4}{8\Delta x \Delta y} \tag{3.47}$$

$$\bar{P}_5 = \pi \bar{p} R^2 - \frac{4\bar{p} R^3}{3\Delta x} - \frac{4\bar{p} R^3}{3\Delta y} + \frac{\bar{p} R^4}{4\Delta x \Delta y}$$

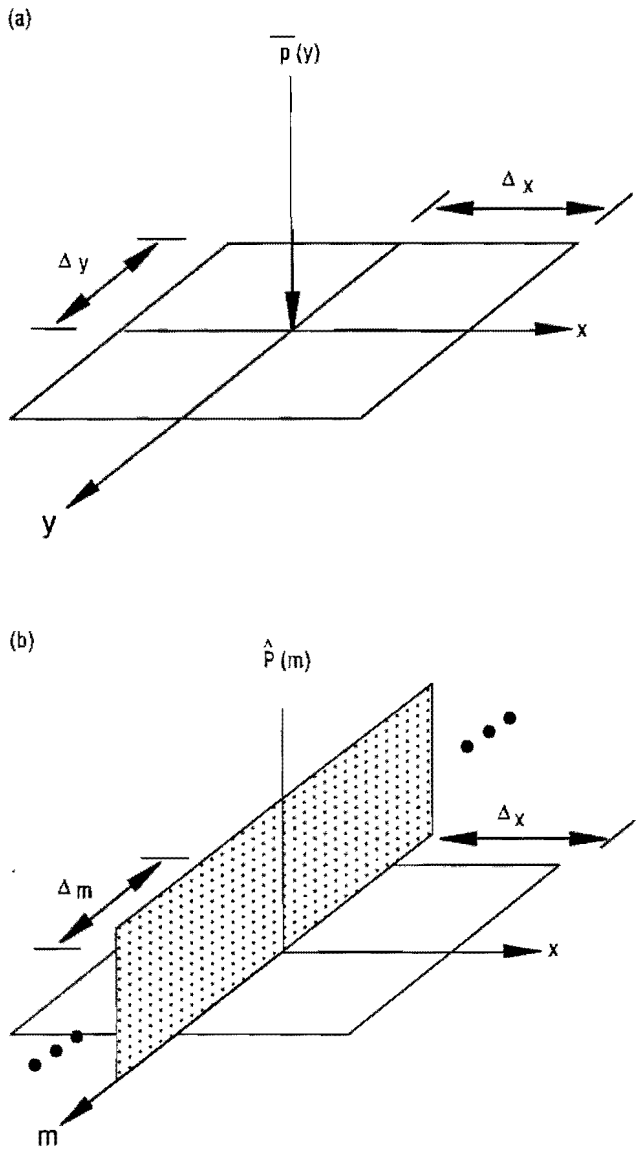

Figure 3.15 Point load in the space and wavenumber domains

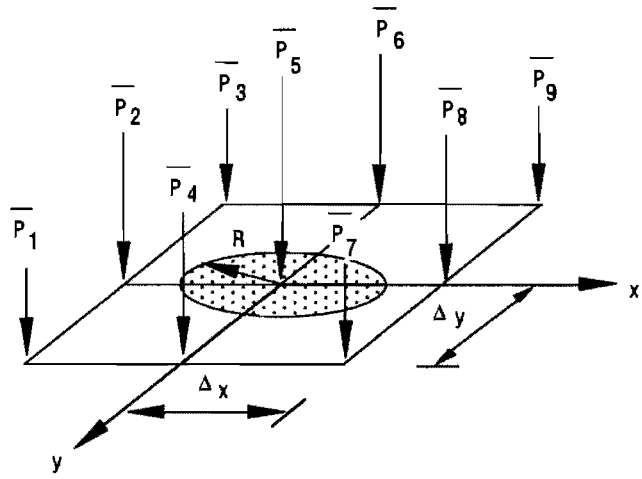

Figure 3.16 Disk load in the space domain

3.8 Computer Implementation

The soil-pavement formulation has been implemented into a computer program called "UTPVT" on the computer Cray X-MP/24 at the University of Texas at Austin. The main algorithm can be written as follows

(1) For each frequency, ω:
  a) For each wavenumber, m:
    i) calculate the stiffness matrix $\boldsymbol{S}(m,\omega)$ for soil-pavement system;
    ii) calculate the load vector $\boldsymbol{P}(m,\omega)$;
    iii) solve Eq. (3.18) : $\boldsymbol{S}\,\boldsymbol{U} = \boldsymbol{P}$ for displacements $\boldsymbol{U}(m,\omega)$;
  b) Perform inverse Fourier transform to obtain displacements $\boldsymbol{U}(y,\omega)$;
(2) Perform inverse Fourier transform to obtain time-history of displacements $\boldsymbol{U}(y,t)$.

Notice that the displacements have to be solved for each frequency and wavenumber. Therefore, computational time of UTPVT is proportional to the number of frequencies as well as the number of wavenumbers. Considerable effort has been made to reduce the computational time required. It is noteworthy to mention two major findings here.

First , it was found that the stiffness matrix $\boldsymbol{S}$ in Eq. (3.18) is not symmetric if the displacements are { u, v, w }. However, the matrix will become symmetric if the displacements are chosen as { u, iv, w }, where the symbol i is equal to –1. Physically, this means that in the wavenumber domain the displacement v in the y-direction is 90 degrees out of phase with the displacements in the x- and z- directions. Because of this, one can take advantage of symmetry to solve the system of equations. The number of operations needed is then reduced from approximately $2/3n^3$ to $1/3n^3$, for large values of n, where n is the number of equations in the system. Also nearly half the memory space is saved in the computer.

Secondly, the loading condition (both for a point load and a disk load) is symmetric with respect to the axis y = 0. In addition, the structure itself is also symmetric with respect to the axis y = 0. Therefore, all the displacements in the space domain should be symmetric with respect to the axis y = 0. This implies that the displacements in the wavenumber domain are also symmetric with respect to the axis m=0. Consequently, one can compute only the non-negative wavenumbers and duplicate the negative terms from them. The number of wavenumbers needed will then be equal to $(N_y + 2) + 1$, N_y being the total number points in the Fourier analysis.

Figure 3.17 shows the execution time on the Cray computer for several cases. The abscissa is the number of layers in the stratum for each case. For all cases, only one frequency is considered. The number of cycles in the expansion Nx is equal to 10 and the number of Fourier points Ny is 128. The total width of the pavement is 50 ft and the dimensions of the finite elements Δx, Δy, Δz are all equal to 0.5 ft. It can be seen that the execution time is approximately a third-order polynomial.

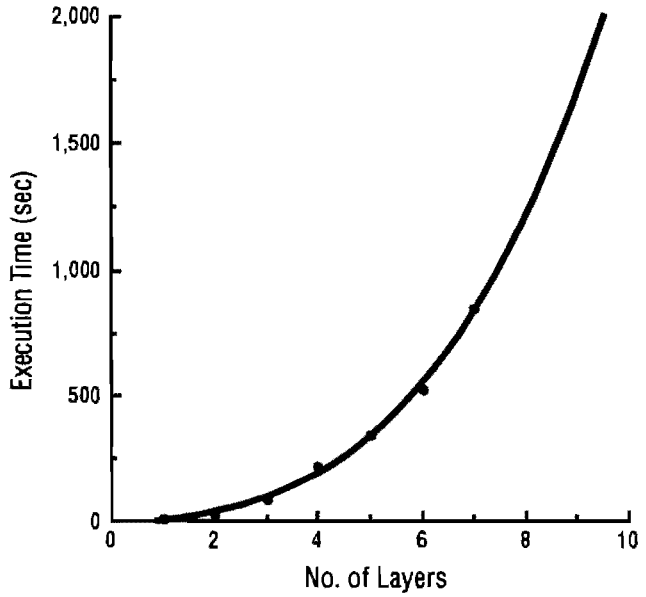

Figure 3.17 Execution time required in program UTPVT

3.9 Summary

The mathematical formulation for a soil-pavement system has been presented in this chapter. The formulation accounts not only for the dynamic nature of the problem, but also for the variation of properties in the soil-pavement system. The system considered consists of an irregular core region and two infinite layered lateral regions. The formulation can also be applied to many other problems.

The soil-pavement structure is modeled as a layered stratum resting on rigid rock or a half space. Each layer is considered to be isotropic, homogeneous, and linearly viscoelastic within each region. The stiffness matrices for the core region and lateral regions are

obtained in the frequency-wavenumber domain. An expansion technique is used to obtain the stiffness matrix for the infinite lateral regions. A viscous bottom boundary is incorporated in the formulation in order to simulatethe half space condition. Point loads and circular disk loads are considered. Finally, the formulation was implemented into a computer program called UTPVT.

CHAPTER 4. VALIDATION AND PARAMETRIC STUDY OF SOIL-PAVEMENT FORMULATION

4.1 Introduction

When applying a discrete model (like the Finite Element Method), it is important to recognize that the results will deviate to some extent from the exact solution depending upon the mesh size. The accuracy of the discrete solution can be improved by choosing a very small value of the discrete parameters such as time increment, element size, etc. There are, however, limits to the size of the mesh if the computational cost is to remain reasonable. Hence, it is essential to perform parametric studies using some model problems whose solutions are either simple or readily available, to determine suitable values of the discrete parameters so that a compromise can be reached between accuracy of the solution and costs of computation.

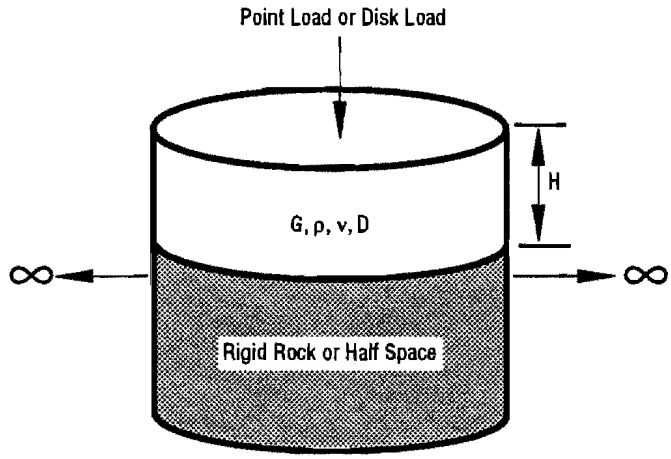

Figure 4.1 Schematic of the model problem

In this chapter, several key parameters in the soil-pavement formulation are investigated, such as type of element, number of sampling points, number of cycles for the expansion of the lateral regions, element size, material damping, and bottom boundary. The model problem shown in Figure 4.1 is selected for the purpose of the investigation. It is a homogeneous and isotropic stratum under axisymmetric loading in a three-dimensional space. The stratum extends to infinity in the horizontal plane, has a total thickness H, and rests on a rigid rock or a half space. For simplicity, the total thickness H, the shear

modulus G, and the mass density ρ are all assumed to have a value of one. The Poisson's ratio ν is 1/3. The material damping ratio D is given the values from 0%, 0.1%, 0.5%, 1% and 2%. The excitation force is assumed to be a steady-state vertical load acting on the surface of the stratum with unit amplitude. The circular excitation frequencies ω are equal to 0, 5 and 10 rad/sec with cyclic frequencies of f = 0 , 0.8, and 1.6 Hz, respectively. The last two frequencies correspond to Rayleigh wavelengths of 1.17 and 0.585.

For a stratum subjected to a vertical point load as in Figure 4.1, the solution can be obtained using the Green's functions obtained by Kausel (1981). This solution will be used as the reference for our investigation. Notice that in Kausel's solution, linearization of the displacement along the z-direction within each layer is assumed. One must therefore subdivide the stratum into several sub-layers. The effect of the number of sublayers is illustrated in Figures 4.2 and 4.3. This is a case with a frequency ω of 5 rad/sec and damping ratio D of 2%. The point load is applied at y = 0. The vertical displacements W are plotted against the horizontal distance y measured from the point of application of the load. It can be seen that the 4-layer solution deviates slightly from the 10-layer solution, but the results are almost identical for 10 and 16 layers. It should also be noticed that the displacement at y = 0 due to a point load should be infinite.

Further studies showed that the 16-layer solution provides accurate results for the higher frequency ω = 10 rad/sec. Therefore, in this chapter, the 16-layer solution is used as the solution with the Green's functions for frequencies from ω = 0 to 10 rad/sec.

4.2 Type of Element

Four types of elements were introduced in Chapter Three. They are SOLID8, SOLID12A, SOLID12B, and SOLID16 as shown in Figure 3.6. For the case (with D = 2% and ω = 5 rad/sec) mentioned in the previous section, the results obtained with these four elements and those from the Green's functions are presented in Figure 4.4 to Figure 4.7. The dimensions of each element are assumed to be 1/8 (i.e. $\Delta x=\Delta y=\Delta z=1/8$). The number of sampling points Ny is 64 and the number of cycles N_X is 10. This means that the total distance Ty for the Fourier transform is equal to 8. Due to the symmetry with respect to the coordinate y = 0, only the records from y = 0 to y = 4 are presented.

In Figure 4.4, the real part of the displacements generally matches the Green's function solution very well except close to the load. Disagreement occurs at the first two stations (y = 0 and y = 1/8), due to the use of finite elements to simulate a pointload. Theoretically, the displacement under the point load is infinite. But in the finite element approach, the displacement will always be finite. On the other hand, the imaginary part of the displacements matches very well at small distances and starts to deviate at a distance of about y = 1.

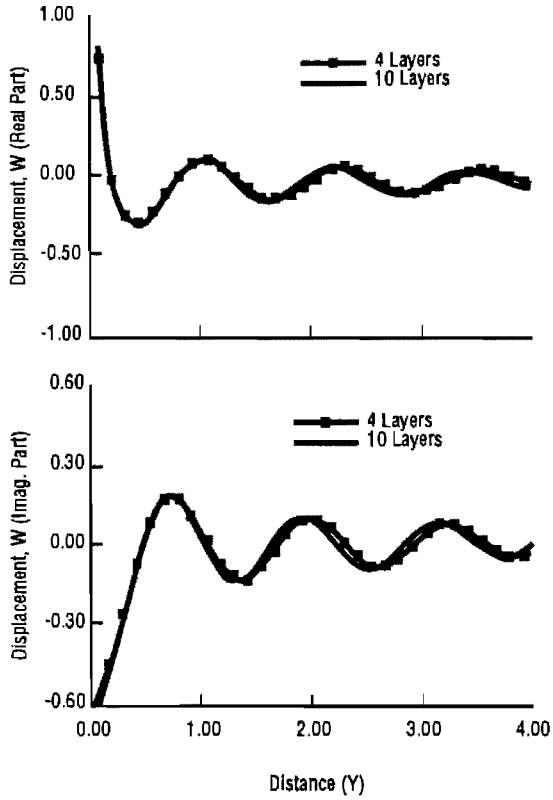

Figure 4.2 **Comparison of the 4-layer and the 10-layer solutions obtained from the Green's functions with 2 percent damping at frequency 0.8 Hz**

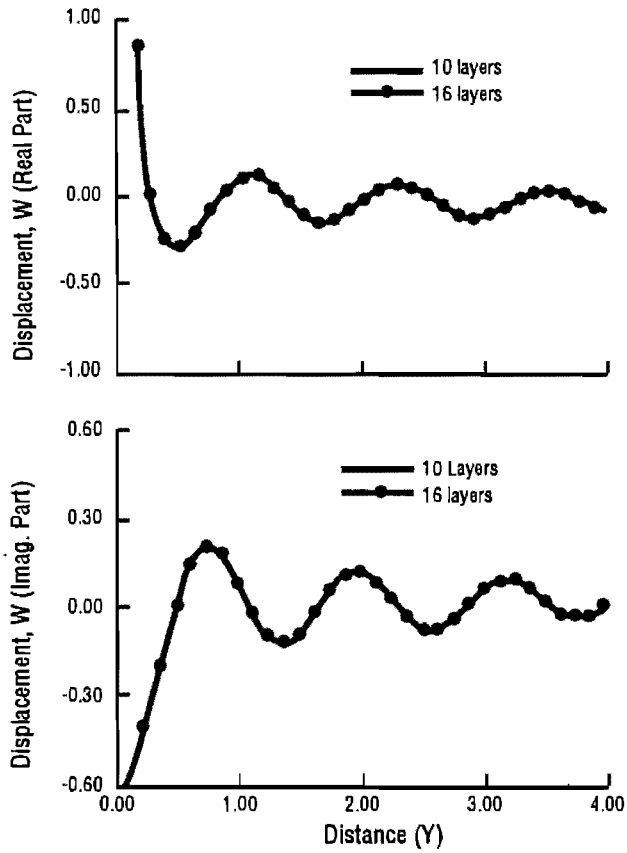

Figure 4.3 **Comparison of the 10-layer and the 16-layer solutions obtained from the Green's functions with 2 percent damping at frequency 0.8 Hz**

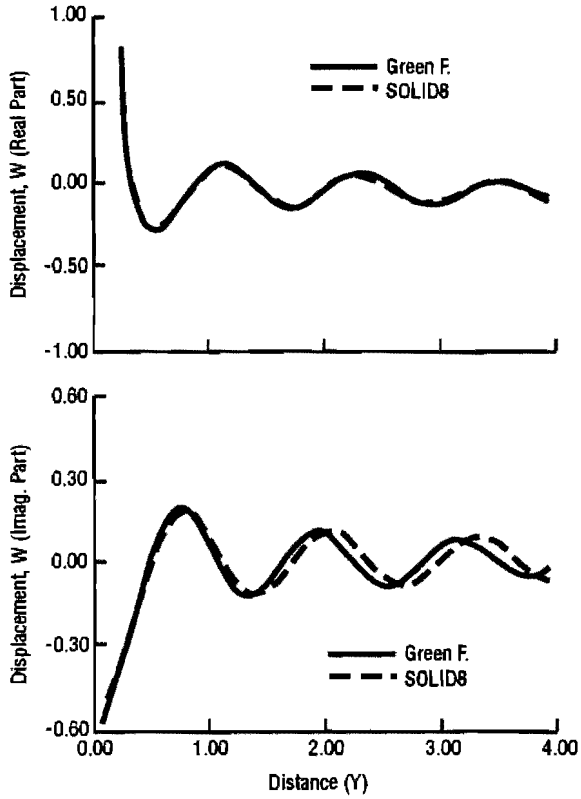

Figure 4.4 **Comparison of the Green's function and the SOLID8 solutions with $\Delta x = \Delta y = \Delta z = 1/8$, $N_x = 10$, $N_y = 64$, 2 percent damping at frequency 0.8 Hz**

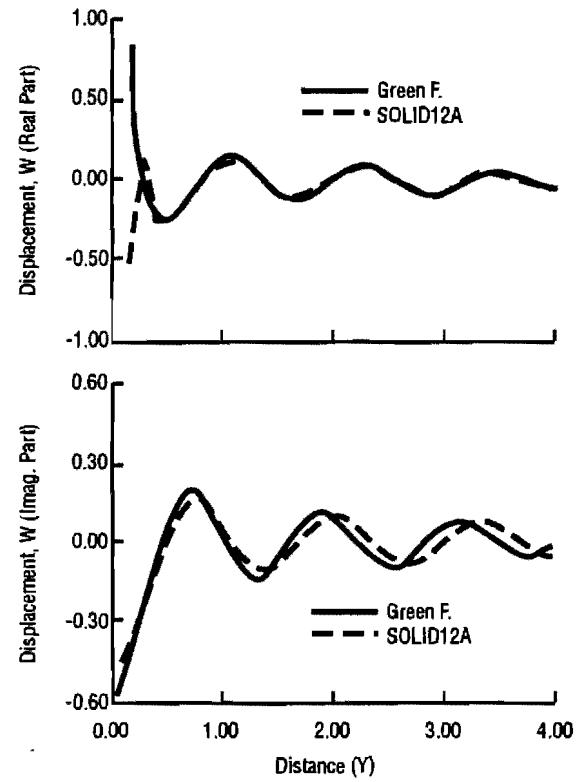

Figure 4.5 **Comparison of the Green's function and the SOLID12A solutions with $\Delta x = \Delta y = \Delta z = 1/8$, $N_x = 10$, $N_y = 64$, 2 percent damping at frequency 0.8 Hz**

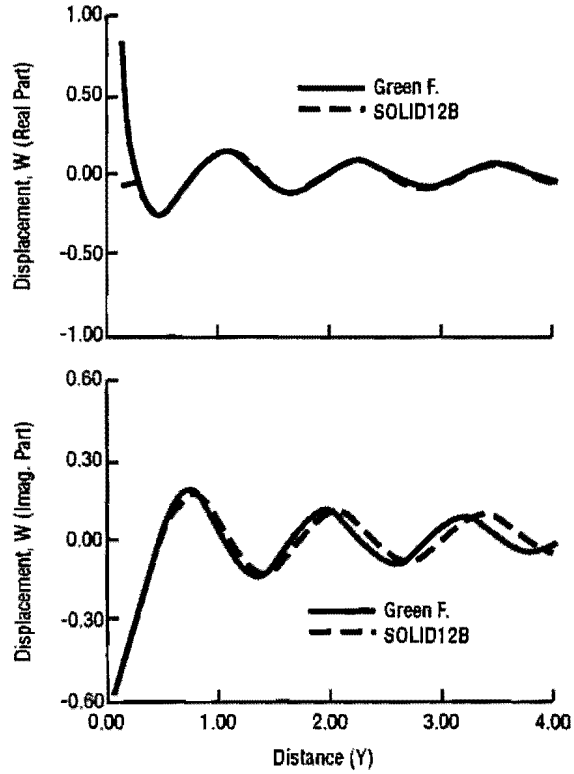

Figure 4.6 **Comparison of the Green's function and the SOLID12B solutions with $\Delta x = \Delta y = \Delta z = 1/8$, Nx = 10, Ny = 64, 2 percent damping at frequency 0.8 Hz**

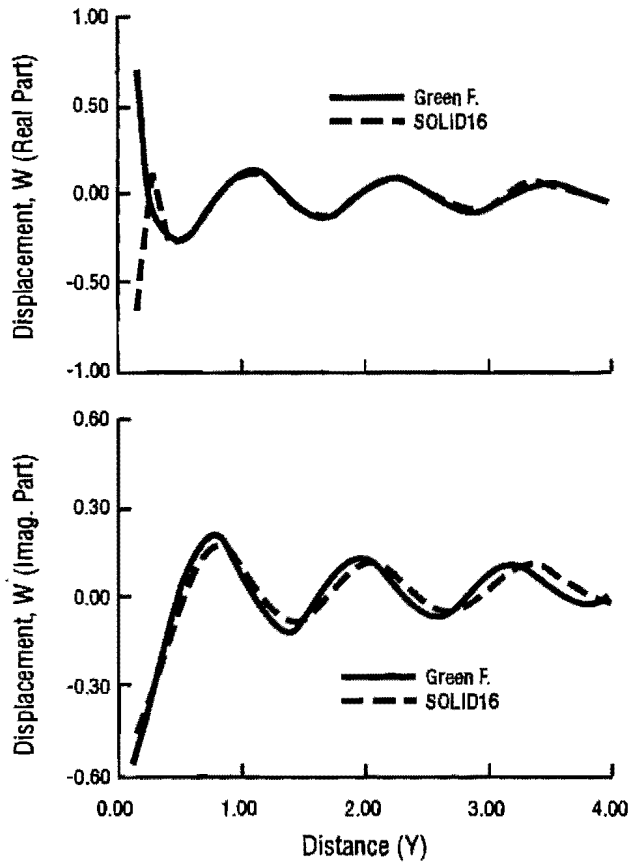

Figure 4.7 **Comparison of the Green's function and the SOLID16 solutions with $\Delta x = \Delta y = \Delta z = 1/8$, Nx = 10, Ny = 64, 2 percent damping at frequency 0.8 Hz**

A similar trend can be found in elements SOLID12A, SOLID12B and SOLID16 as shown in Figures 4.5, 4.6 and 4.7. For the elements SOLID12A and SOLID16, more disagreement in the real part of the displacements can be seen at distances ranging from y = 0 to y = 3/8. The reason for this is not clear because for elements like SOLID12A and SOLID16 which are quadratic in the x-direction and linear in the y-direction, one would have expected the results to be at least as good as those with elements which are linear in both horizontal directions.

In order to study the effect of the element aspect ratios (e.g. $\Delta x/\Delta y$), further studies were conducted using the element SOLID16. In Figure 4.8, Δy is equal to 1/8. It can be seen that the solution with Δx =1/8 and Δz = 1/4 produces a better match than that with Δx = 1/4 and Δz = 1/8. This implies that the solution is more sensitive to the ratio of $\Delta x/\Delta y$ than to the ratio $\Delta z/\Delta y$. Since the dimension of Δx is limited by the dimension of Δy, it was felt that using linear interpolation in the x-direction was sufficient, whereas using a quadratic expansion in the z-direction allowed to increase the vertical dimension without loss of accuracy. This point is further confirmed in Figure 4.9 where element SOLID12B is used and the result with Δz = 1/2 is still in good agreement with that for Δz = 1/8. Two major findings were described in this section. One was that the solutions which are linear in the x-direction show less trouble at small distances. The second is that quadratic interpolation in the z-direction can be helpful in the sense that a smaller number of layers can be used without loss of accuracy. Therefore, it was decided to use the element SOLID12B in this study. Further investigation of element SOLID12B will be presented in the following sections.

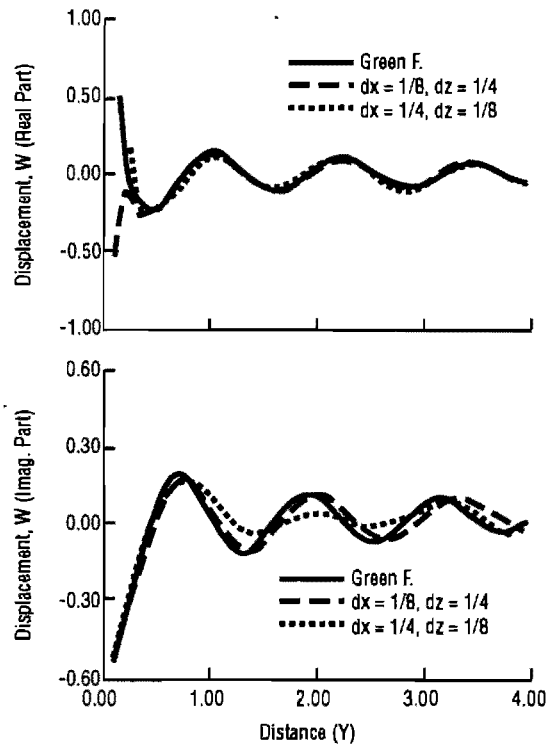

Figure 4.8 Comparison of the Green's function and two SOLID16 solutions with different Δx and Δz, but with Δy = 1/8, N_x = 10, N_y = 64, 2 percent damping at frequency 0.8 Hz

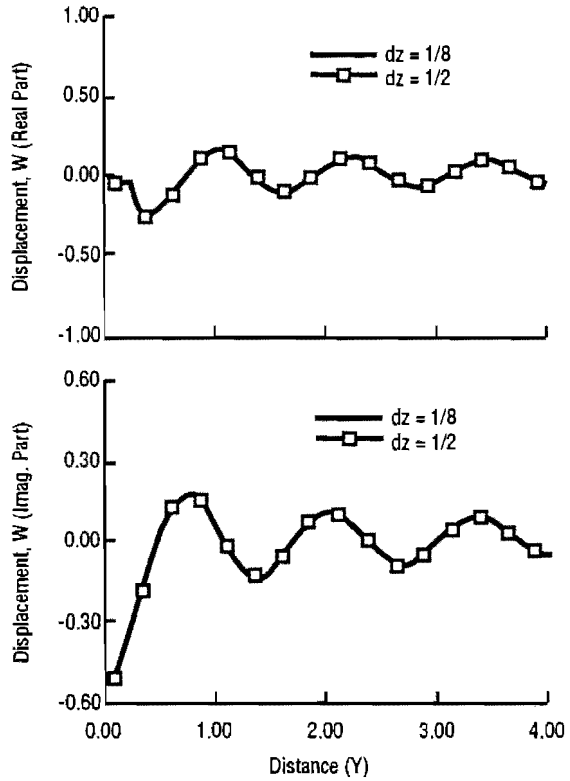

Figure 4.9 Comparison of two SOLID12B solutions with different Δz, but with $\Delta x = \Delta y = 1/8$, $N_x = 10$, $N_y = 64$, 2 percent damping at frequency 0.8 Hz

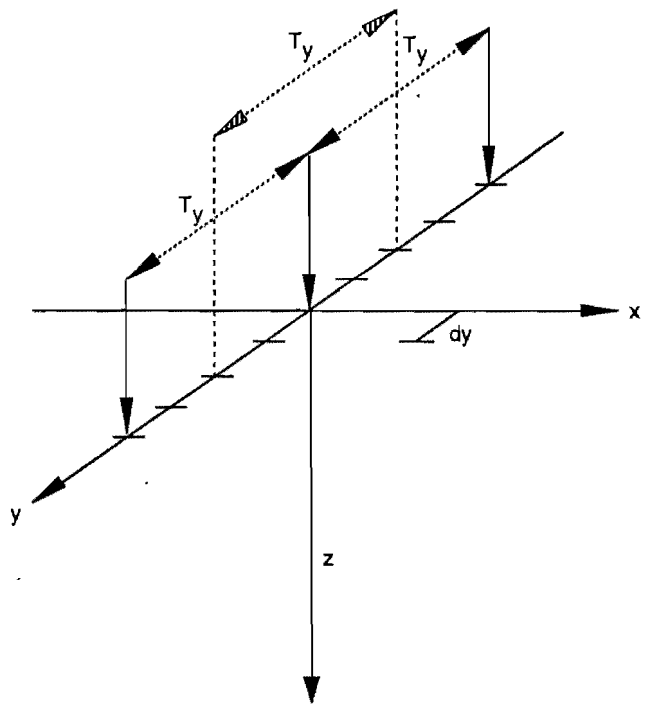

Figure 4.10 Illustration of the reoccurrence of Fast Fourier Transform

4.3 Number of Sampling Points

For a given value of the discrete interval Δy, the number of sampling points, N_y, will determine the total distance,T_y, at which the point-load will repeat itself in the y-direction, as shown in Figure 4.10. It is clear that for a better representation of a single point load, it is better to use as many sampling points as possible so that the influence of the adjacent point load is negligible. However, for practical applications, a small number of sampling points is preferred in order to cut down the computational costs. In the application of the SASW method, the receivers are generally placed at a distance of one to two wavelengths (for the surface waves) from the source. In this case, one should choose a value of N_y so that the solution is accurate within two wavelengths. For the stratum in the model problem, the Rayleigh wavelength λ_R is equal to 1.17 for an excitation ω = 5 rad/sec. The distance of two wavelengths will be equal to 2.34. As can be seen in Figure 4.11, the result with N_y = 64 is qualitatively in good agreement with the Green's function up to the distance of y = 1. For N_y = 128 (as in Figure 4.12), the result is good up to about a distance y=2.5 (> $2\lambda_R$ = 2.34). The

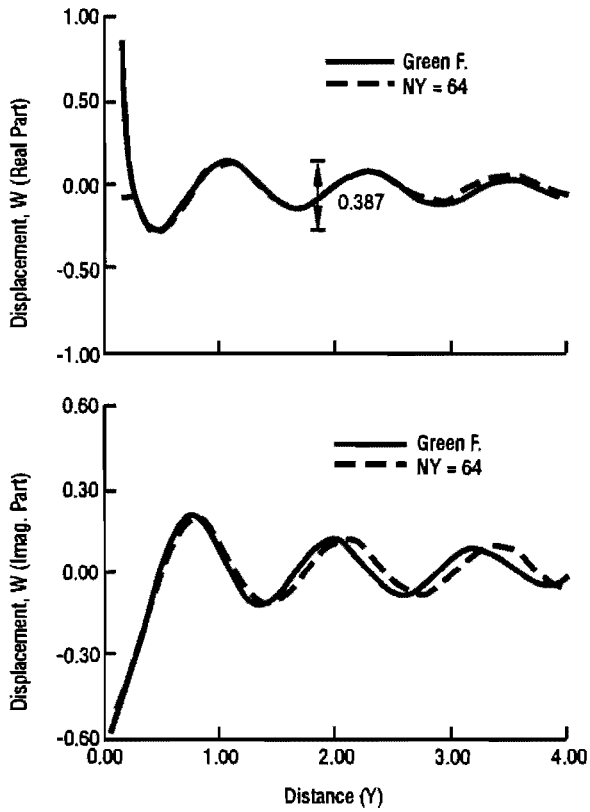

Figure 4.11 Comparison of the Green's function and the SOLID12B solutions with $\Delta x = \Delta y = 1/8$, $\Delta z = 1/2$, $N_x = 10$, $N_y = 64$, 2 percent damping at frequency 0.8 Hz

differences between the Green's function solution and the proposed solution are listed in Table 4.1. Each error in this table is the arithmetic average of the errors for the real and the

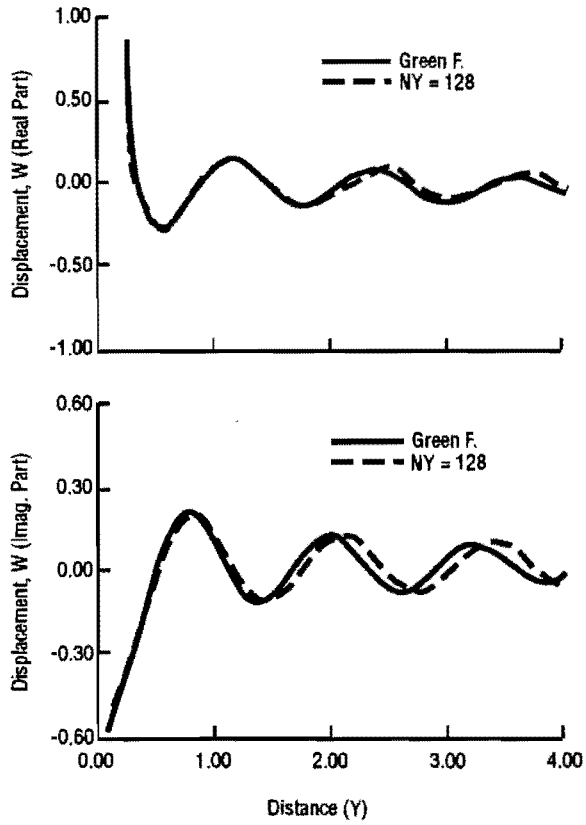

Figure 4.12 Comparison of the Green's function and the SOLID12B solutions with $\Delta x = \Delta y = 1/8$, $\Delta z = 1/2$, $N_x = 10$, $N_y = 128$, 2 percent damping at frequency 0.8 Hz

Table 4.1 Errors in displacement for different number of sampling points N_y with D = 2%, $\Delta x = \Delta y = 1/8$, $\Delta z = 1/2$, $N_x = 10$, $\omega = 5$ rad/sec

N_y / y	64	128	256	512
1.125 ($\approx 1\lambda_R$)	6.8%	3.5%	3.2%	3.2%
2.375 ($\approx 2\lambda_R$)	10.0 %	ff 4.8%	3.8%	3.8%

imaginary part. For each part, the error is calculated by the difference in displacements between the Green's function solution and the discrete solution; divided by the first peak-to-peak amplitude in the Green's function. For instance, for the real part, the first peak-to-peak amplitude is equal to 0.387 as shown in Figure 4.11. For $N_y = 64$, the error is 6.8% at y = 1.125 ($\approx 1\lambda_R$) and 10.0% at y = 2.375.($\approx 2\lambda_R$). While for Ny = 128, the error is 3.5% at y = 1.125 and 4.8% at y = 2.375.

This suggests that at least 128 points be used in order to obtain results with errors of 5% or less within two wavelengths. It should be noticed that the accuracy of the results is also affected by the value of Δy relative to the wavelength. This effect will be studied further in Section 4.5.

4.4 Number of Cycles in Lateral Expansion

For a given discrete interval, Δx, in the x-direction, the number of cycles in the expansion in the x-direction, N_X, determines the total distance T_X of the lateral region under consideration in the analysis. Table 3.1 shows the relation between N_X and T_X. For instance, $N_X = 8$ corresponds to a total distance $T_X = 256\ \Delta x$.

It is apparent that the use of a larger N_X will simulate better the semi-infinite lateral region. Figures 4.12 through 4.15 show the results for values of N_X of 10, 8, 6, and 4, respectively. As can be seen, the results with $N_X = 8$ are identical to those with Nx = 10 and they are both in good agreement with the Green's function solution. The solution with $N_X = 6$ is slightly less accurate while for $N_X = 4$, the solution is no longer acceptable.

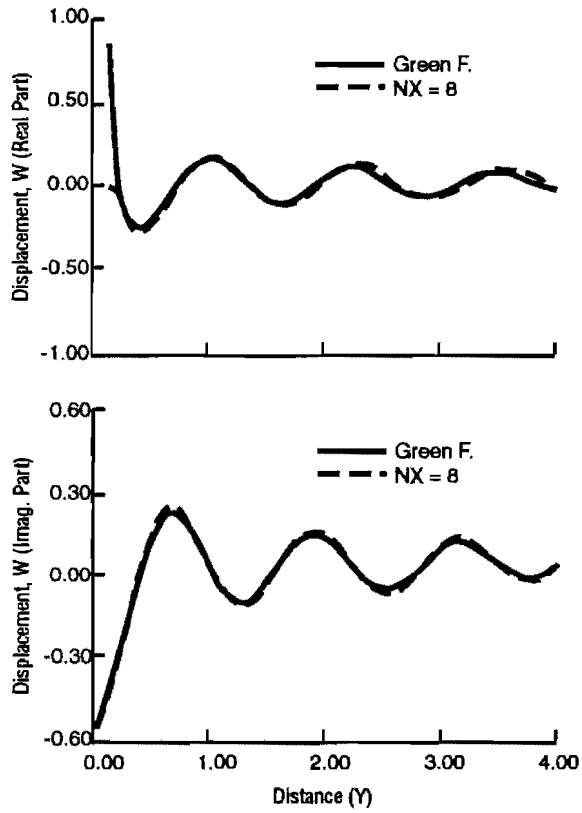

Figure 4.13 Comparison of the Green's function and the SOLID12B solutions with $\Delta x = \Delta y = 1/8$, $\Delta z = 1/2$, $N_X = 8$, $N_y = 128$, 2 percent damping at frequency 0.8 Hz

It is interesting to compare the total distances required in both the x- and y-directions for an accurate solution. Since Tx represents only one lateral region (meaning one-sided region), it is reasonable to use half of the total distance in the y-direction, T_y, for comparison. In these four cases, since Δx is equal to 1/8, the corresponding values of T_X are

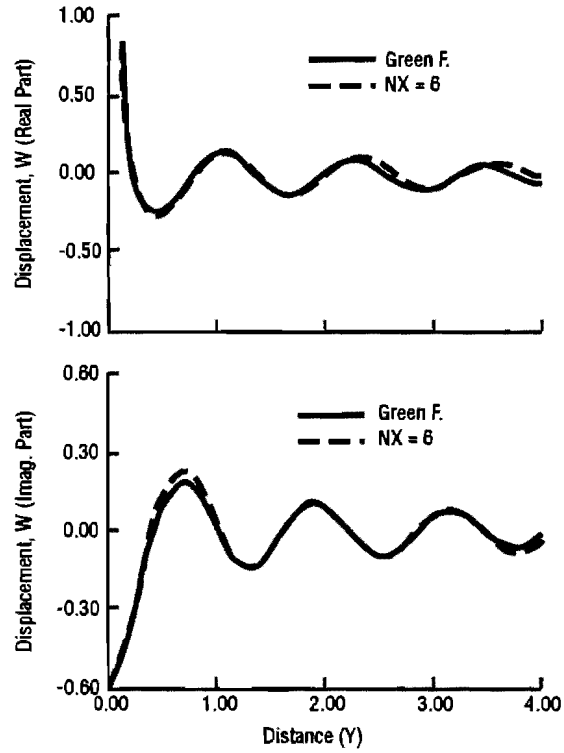

Figure 4.14 Comparison of the Green's function and the SOLID12B solutions with $\Delta x = \Delta y = 1/8$, $\Delta z = 1/2$, $N_x = 6$, $N_y = 128$, 2 percent damping at frequency 0.8 Hz

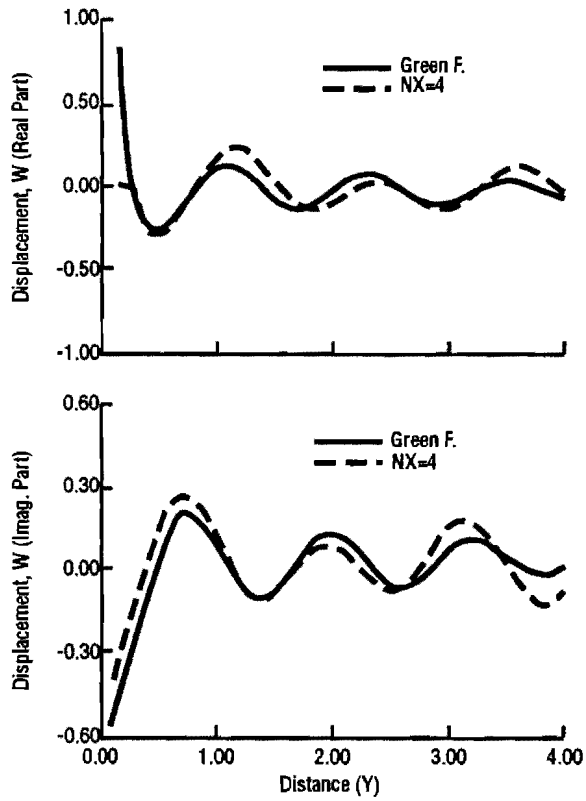

Figure 4.15 Comparison of the Green's function and the SOLID12B solutions with $\Delta x = \Delta y = 1/8$, $\Delta z = 1/2$, $N_x = 4$, $N_y = 128$, 2 percent damping at frequency 0.8 Hz

128, 64, 32, and 16. The number of sampling points, N_y, is equal to 128 with interval $\Delta y = 1/8$. The half value of T_y will be 8. The distance ratios $T_x/(T_y/2)$ will be 16, 8, 4, and 2, respectively. Therefore, in this case the minimum ratio $T_x/(T_y/2)$ required to give accurate results is about 8.

4.5 Element Size versus Wavelength

So far, only a single frequency $\omega = 5$ rad/sec has been studied. In this section, different frequencies will be considered to assess the effect of the element size relative to the wavelength.

For a better understanding of the nature of a dynamic problem, an example is depicted in Figure 4.16 where a one-dimensional harmonic plane wave propagates through a medium. The wave is a continuous function with a wavelength λ. The wavelength can be determined by the properties of the medium and the frequency of the wave. For a given medium, the wavelength is inversely proportional to the frequency. The higher the frequency, the shorter the wavelength. Therefore, instead of relating the element size to the frequency, one can use the ratio of wavelength to element size (wavelength-element ratio).

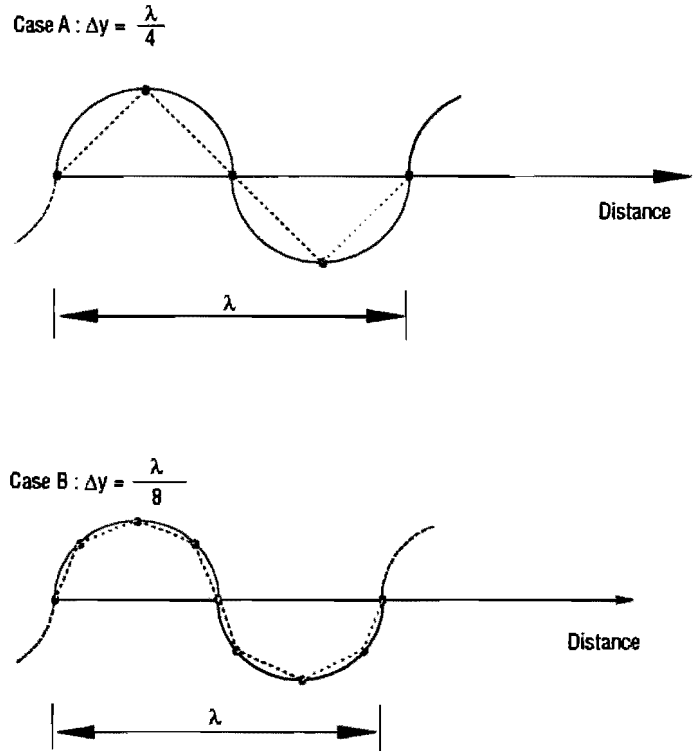

Figure 4.16 Linear discretization of a harmonic plane wave

For a discrete model, several discrete points are usually required in one cycle in order to represent the wave form properly. For case A with $\lambda/\Delta y = 4$ in Figure 4.16, a four-point linear interpolation is used in one cycle. The dashed line shows the discrete solution which does not represent well enough the continuous function. For an 8-point linear interpolation (case B with $\lambda/\Delta y = 8$), the representation has improved significantly. From this example, it

can be seen that for a good representation of a dynamic problem using linear interpolation, it is better to keep the ratio $\lambda/\Delta y$ at least within 4 to 8.

Since the problem in our study is a three-dimensional one, it is necessary to study three different wavelength-element ratios, namely, $\lambda_R/\Delta x$, $\lambda_R/\Delta y$, and $\lambda_R/\Delta z$ where λ_R is the wavelength of the Rayleigh wave. Since the linear interpolation in both the x- and y-directions has been adopted for element SOLID12B, it is obvious that one can keep Δx equal to Δy. Thus, in our investigation it is necessary to study only two quantities: $\lambda_R/\Delta y$ and $\lambda_R/\Delta z$.

Figure 4.17 shows the results using $\Delta x = \Delta y = 1/8$ and $\Delta z = 1/2$ for frequency $\omega = 0$ rad/sec. Since this is a static case, there is no physical meaning for the corresponding wavelength. Nevertheless, the results are in good agreement with those using the Green's function except close to the load.

Figures 4.18 and 4.19 show the results for frequency $\omega = 5$ rad/sec with a corresponding wavelength $\lambda_R = 1.17$. In Figure 4.18 with $\Delta y = 1/4$ and $\Delta z = 1/2$, the discrepancy between the Green's function solution and the discrete solution is quite noticeable. With $\Delta y = 1/8$ and $\Delta z = 1/2$, good agreement up to $2\lambda_R$ (= 2.34) can be obtained as shown in Figure 4.19 where $\lambda_R/\Delta y$ and $\lambda_R/\Delta z$ are about 9.4 and 2.3, respectively. Notice that because of the quadratic interpolation used in the z-direction, a smaller wavelength-element ratio $\lambda_R/\Delta z$ can be used without loss of accuracy.

For higher frequency $\omega = 10$ rad/sec with corresponding wavelength $\lambda_R = 0.59$, the results of $\Delta y = 1/8$ and $\Delta z = 1/2$ are no longer acceptable as shown in Figure 4.20. With $\Delta y = 1/16$ and $\Delta z = 1/2$, the results (Figure 4.21) are still not acceptable. In Figure 4.22 with $\Delta y = 1/16$ and $\Delta z = 1/4$ corresponding to $\lambda_R/\Delta y = 9.4$ and $\lambda_R/\Delta z = 2.3$, good agreement up to a distance of $2\lambda_R$ (= 1.17) is obtained.

It is suggested, therefore, that to use the ratios $\lambda_R/\Delta y = 10$ and $\lambda_R/\Delta z = 2.5$ in order to obtain good solutions up to two wavelengths. The material damping ratio was assumed to be 2% for all cases in this section. Detailed investigation of the effect of damping on the accuracy of the solution will be addressed in the next section.

4.6 Material Damping

In the preceding section, the material damping ratio D was assumed to have a value of 2% and so the dynamic rule with $\lambda_R/\Delta y = 10$ and $\lambda_R/\Delta z = 2.5$ was derived. It is expected that this dynamic rule can apply well for damping ratios larger than 2%, since more energy per unit distance would be dissipated and the displacement would die out faster. It is, therefore, interesting to investigate cases with damping ratio less than 2% using this rule.

Figures 4.23 through 4.25 show the results with zero damping. For zero frequency (as in Figure 4.23), both real and imaginary part are in good agreement with those of the Green's function. The imaginary part is zero for all distances since this is a static case. For frequencies $\omega = 5$ and 10 rad/sec, the discrepancy becomes significant.

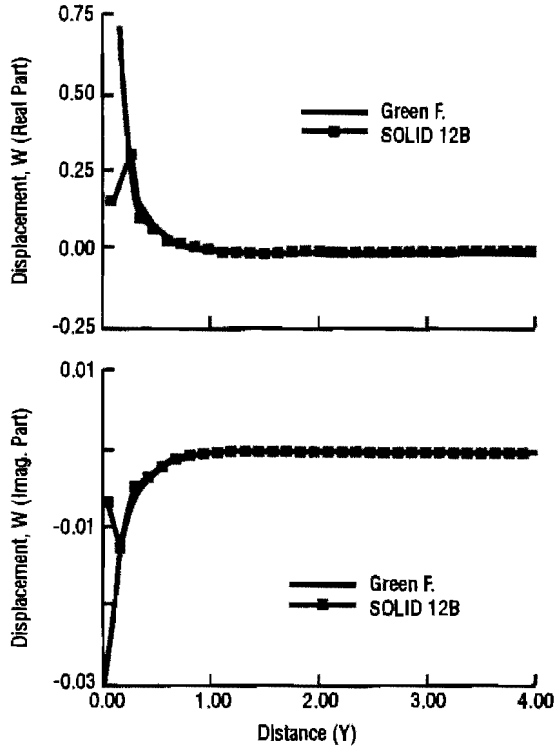

Figure 4.17 Comparison of the Green's function and the SOLID12B solutions with $\Delta x = \Delta y = 1/8$, $\Delta z = 1/2$, $N_x = 10$, $N_y = 128$, 2 percent damping at frequency 0 Hz

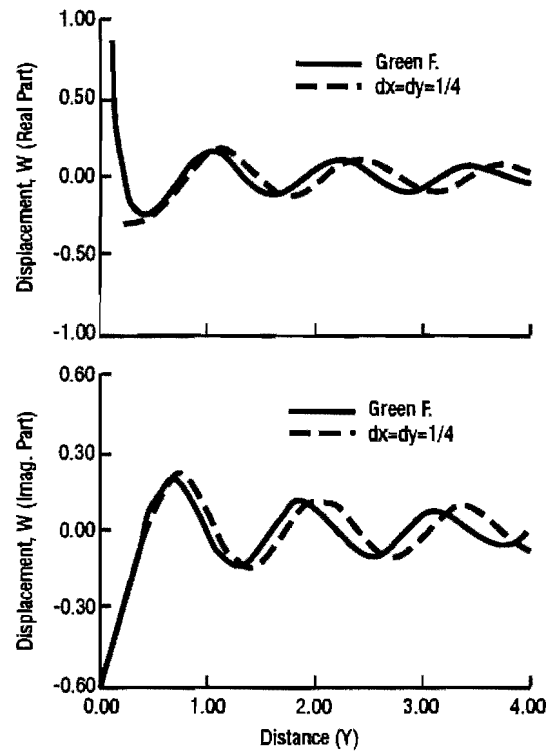

Figure 4.18 Comparison of the Green's function and two SOLID12B solutions with $\Delta x = \Delta y = 1/4$, $\Delta z = 1/2$, $N_x = 10$, $N_y = 128$, 2 percent damping at frequency 0.8 Hz

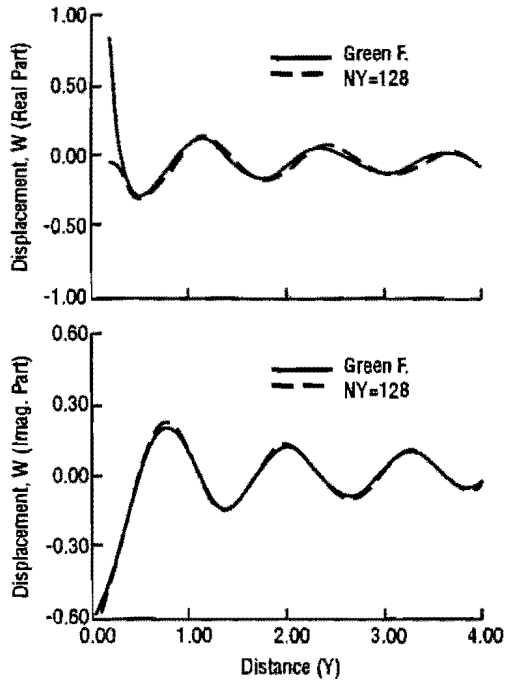

Figure 4.19 Comparison of the Green's function and the SOLID12B solutions with $\Delta x = \Delta y = 1/8$, $\Delta z = 1/2$, $N_x = 10$, $N_y = 128$, 2 percent damping at frequency 0.8 Hz

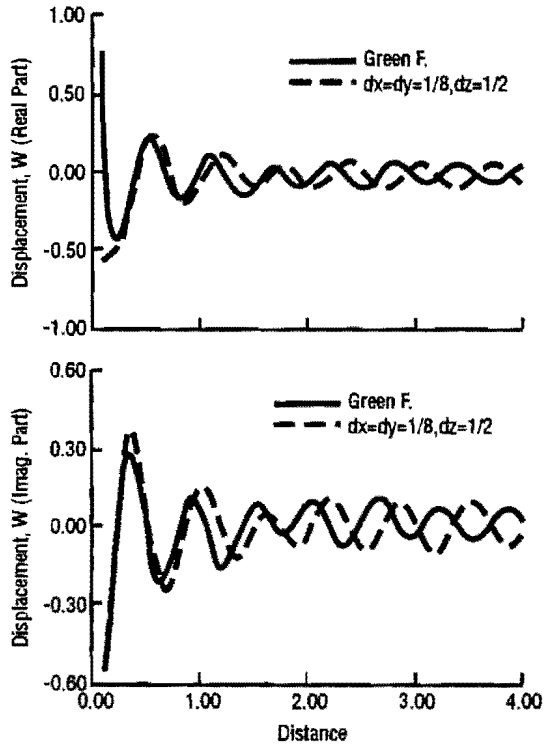

Figure 4.20 Comparison of the Green's function and the SOLID12B solutions with $\Delta x = \Delta y = 1/8$, $\Delta z = 1/2$, $N_x = 10$, $N_y = 128$, 2 percent damping at frequency 1.6 Hz

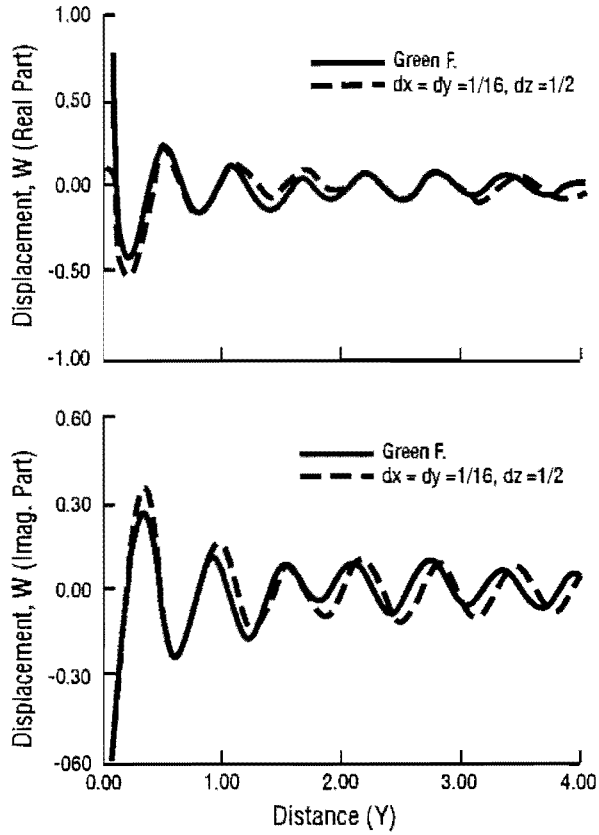

Figure 4.21 Comparison of the Green's function and the SOLID12B solutions with $\Delta x = \Delta y = 1/16$, $\Delta z = 1/2$, $N_x = 10$, $N_y = 128$, 2 percent damping at frequency 1.6 Hz

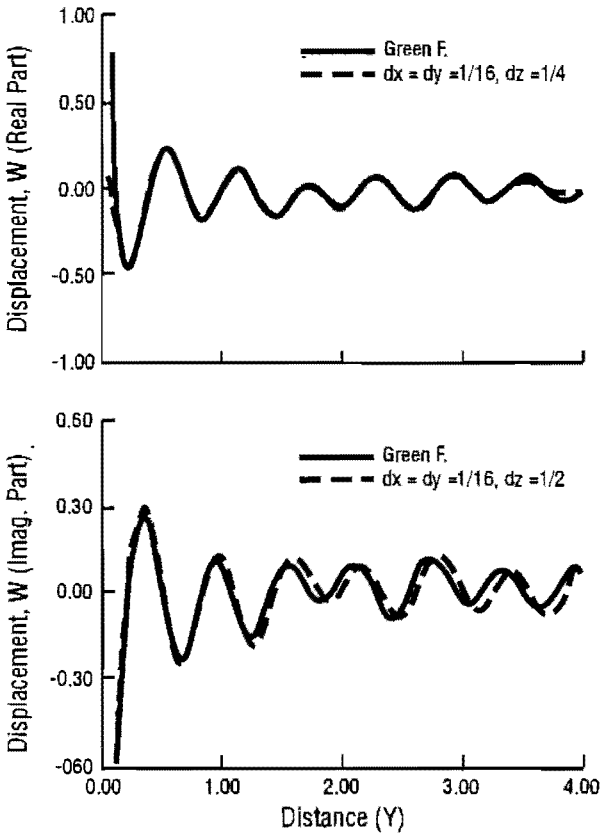

Figure 4.22 Comparison of the Green's function and the SOLID12B solutions with $\Delta x = \Delta y = 1/8$, $\Delta z = 1/4$, $N_x = 10$, $N_y = 128$, 2 percent damping at frequency 1.6 Hz

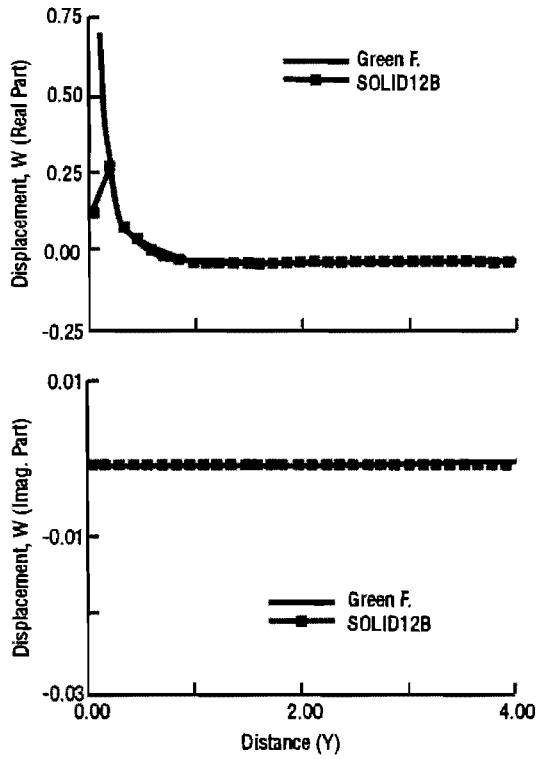

Figure 4.23 Comparison of the Green's function and the SOLID12B solutions with $\Delta x = \Delta y = 1/8$, $\Delta z = 1/2$, $N_x = 10$, $N_y = 128$, no damping at frequency 0 Hz

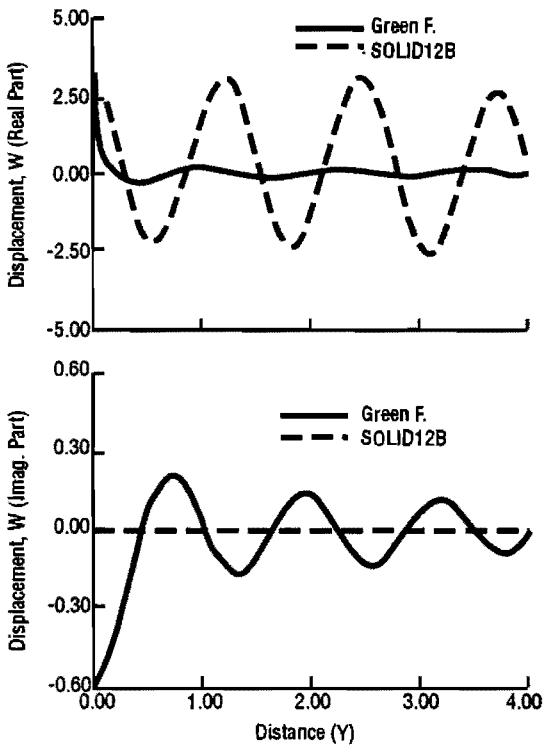

Figure 4.24 Comparison of the Green's function and the SOLID12B solutions with $\Delta x = \Delta y = 1/8$, $\Delta z = 1/2$, $N_x = 10$, $N_y = 128$, no damping at frequency 0.8 Hz

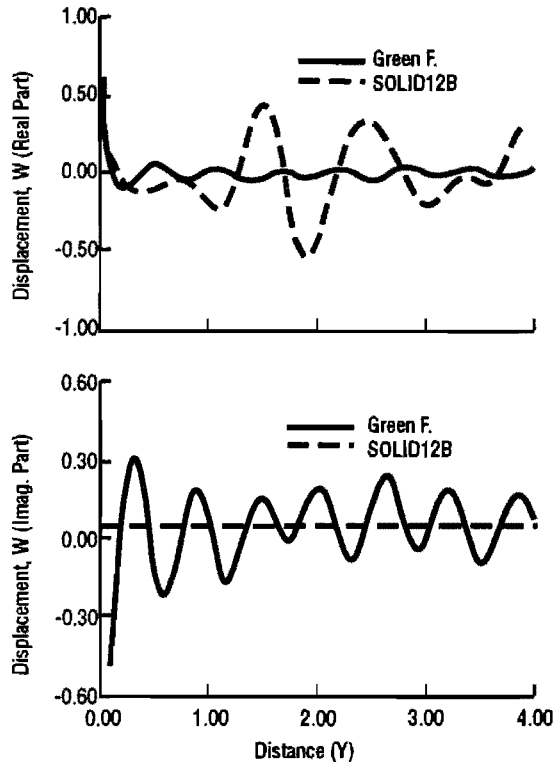

Figure 4.25 Comparison of the Green's function and two SOLID12B solutions with $\Delta x = \Delta y = 1/8$, $\Delta z = 1/2$, $N_x = 10$, $N_y = 128$, no damping at frequency 1.6 Hz

Figures 4.26 through 4.28 show the results for damping ratio D =0.1%. For zero frequency (as in Figure 4.26), both the Green's function solution and the present one start to have some

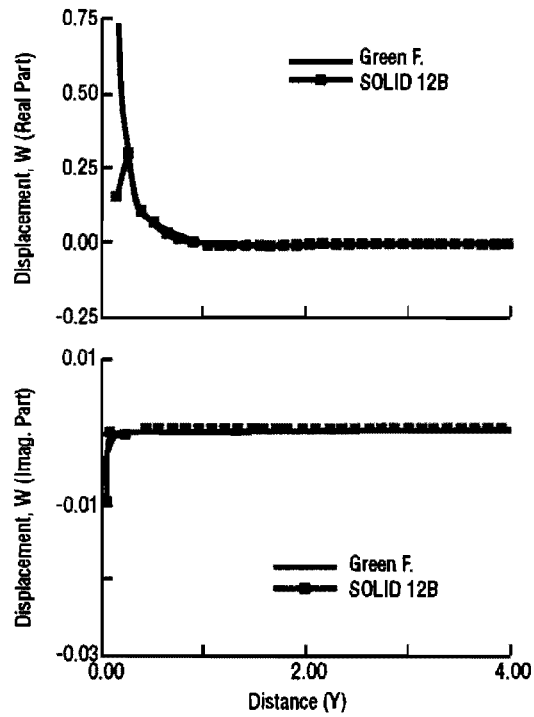

Figure 4.26 Comparison of the Green's function and the SOLID12B solutions with $\Delta x = \Delta y = 1/8$, $\Delta z = 1/2$, $N_x = 10$, $N_y = 128$, 0.1 percent damping at frequency 0 Hz

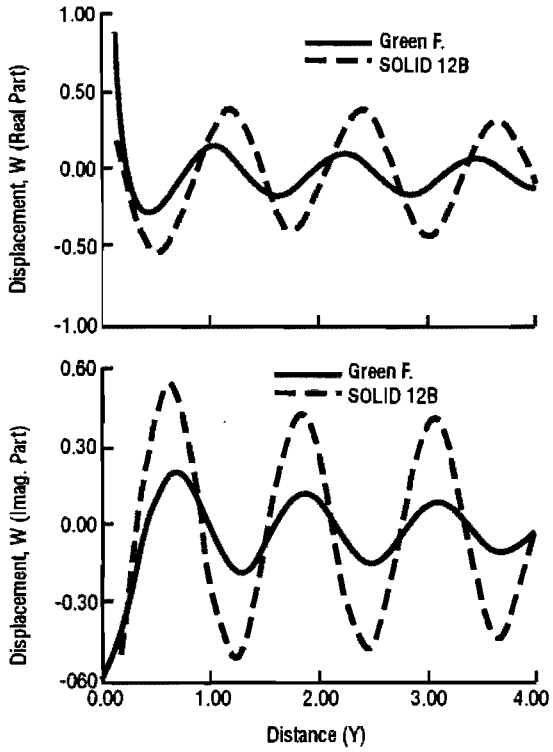

Figure 4.27 **Comparison of the Green's function and the SOLID12B solutions with $\Delta x = \Delta y = 1/8$, $\Delta z = 1/2$, $N_x = 10$, $N_y = 128$, 0.1 percent damping at frequency 0.8 Hz**

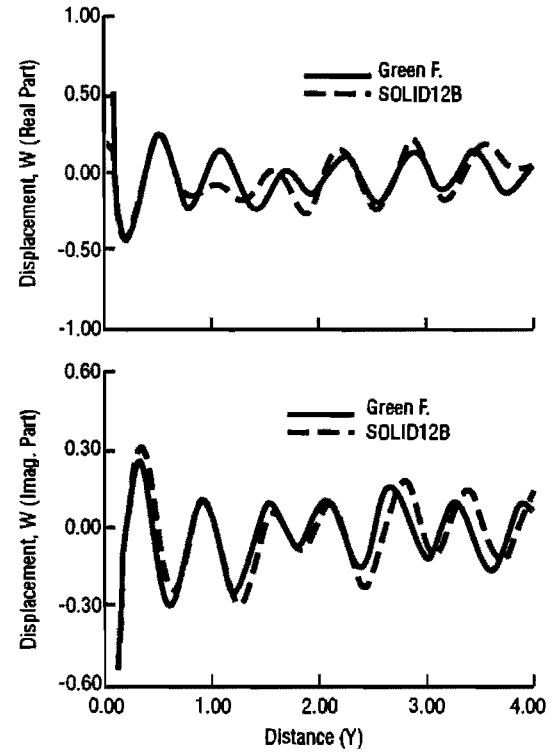

Figure 4.28 **Comparison of the Green's function and the SOLID12B solutions with $\Delta x = \Delta y = 1/8$, $\Delta z = 1/2$, $N_x = 10$, $N_y = 128$, 0.1 percent damping at frequency 1.6 Hz**

non-zero values in the imaginary part. For frequencies ω = 5 and 10 rad/sec, the imaginary part of the discrete solution improves significantly compared with that of zero damping. Still the discrepancy is not negligible.

Figures 4.29 through 4.31 and Figures 4.32 through 4.34 show the results for damping ratios D = 0.5 and 1%, respectively. Generally, it can be seen that the discrepancy decreases as the damping ratio increases. For damping ratios less than 2% but more than 0, the discrepancy can be reduced by using a number of points Ny larger than 128 and a number Nx larger than 10.

4.7 Half Space Bottom Boundary

So far, the investigation is done for the cases of rigid rock condition. In this section, the half space condition for the bottom boundary will be studied. The half space solution of Green's function is obtained by expanding the continuum stiffness matrix (Kausel, 1981). This solution will be used here as the reference in order to verify the viscous bottom boundary.

Consider the model problem as shown in Figure 4.1. Instead of a rigid rock, the bottom boundary is assumed to be a half space and its has identical material properties as the top layer. All materials have two percent damping . The load is a point load at a frequency of 0.8 Hz. The corresponding Rayleigh wavelength is 1.17. Three cases are presented here as shown in Figures 4.35, 4.36, and 4.37, where the thicknesses of the top layer are H=1, 2, and 3, respectively. For each case, the surface displacements are obtained for both solutions. The number of expansion N_x is 10 and the number of Fourier points N_y is 128 for the viscous boundary solution.

It can be seen that there is still some disagreement in both solutions for the case with H=1. For H=2, the discrepancy is practically negligible. However, no further improvement can be seen for H=3. Therefore, it was concluded that the discrepancy between two solutions becomes insignificant when the thickness H is larger than two wavelengths (=2.34).

4.8 Disk Load Solution

The disk load solution will be studied in this section. This is specially important for nondestructive testings like the Dynaflect and FWD where the displacements near the load are of interest.

Figure 4.38 shows the vertical displacements due to a disk load with a radius = 0.0625 at a frequency of 0.8 Hz. It can be seen that both solutions are in good agreement even near the load. Some small discrepancy can be found at large distances. Figure 4.39 shows the displacements in terms of amplitude and phase. Again, they are in good agreement. Some deviation in the phase can be seen when the distance is larger than 2.5.

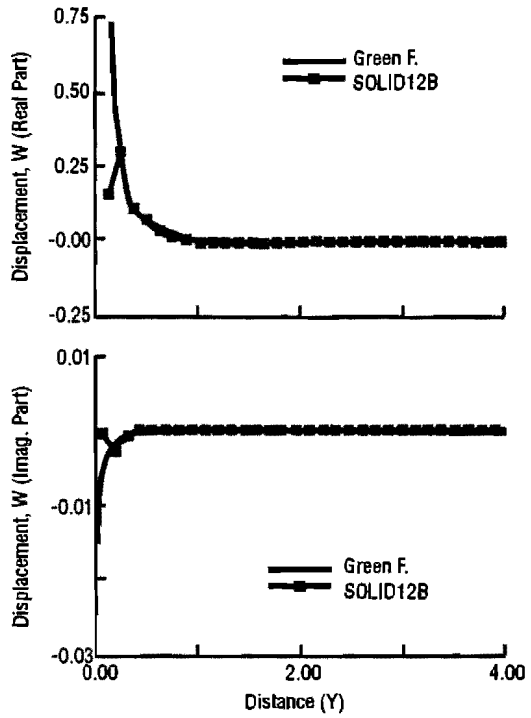

Figure 4.29 Comparison of the Green's function and the SOLID12B solutions with $\Delta x = \Delta y = 1/8$, $\Delta z = 1/2$, $N_x = 10$, $N_y = 128$, 0.5 percent damping at frequency 0 Hz

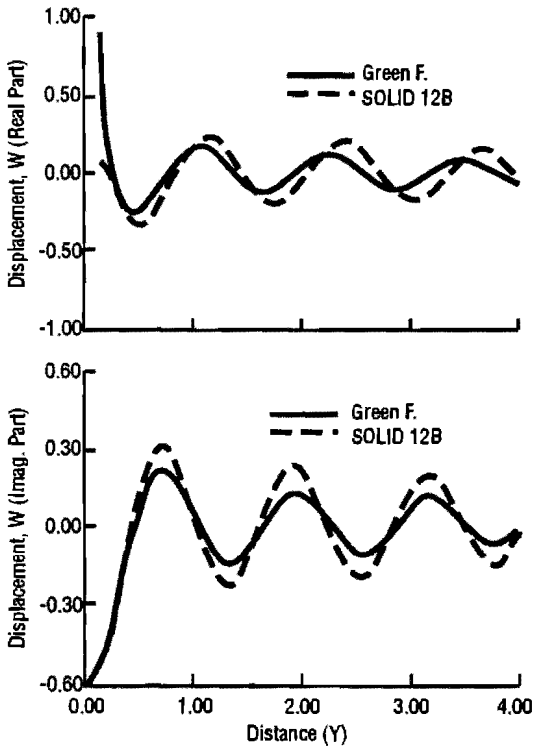

Figure 4.30 Comparison of the Green's function and the SOLID12B solutions with $\Delta x = \Delta y = 1/8$, $\Delta z = 1/2$, $N_x = 10$, $N_y = 128$, 0.5 percent damping at frequency 0.8 Hz

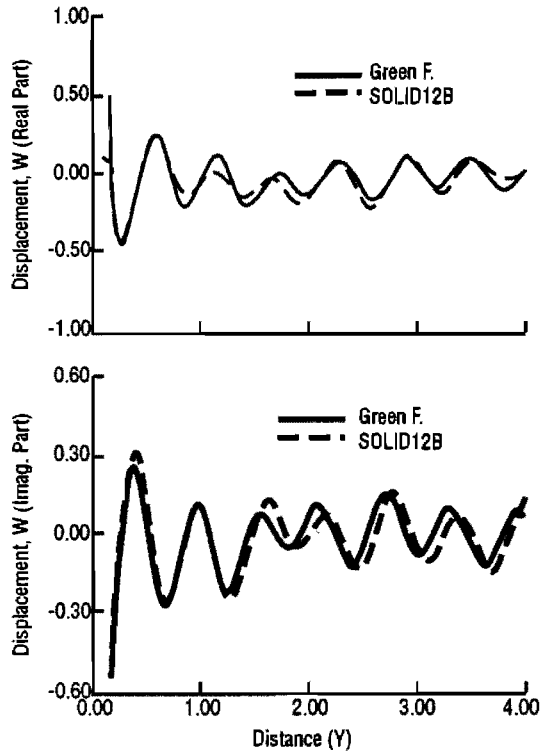

Figure 4.31 Comparison of the Green's function and the SOLID12B solutions with $\Delta x = \Delta y = 1/8$, $\Delta z = 1/2$, $N_x = 10$, $N_y = 128$, 0.5 percent damping at frequency 1.6 Hz

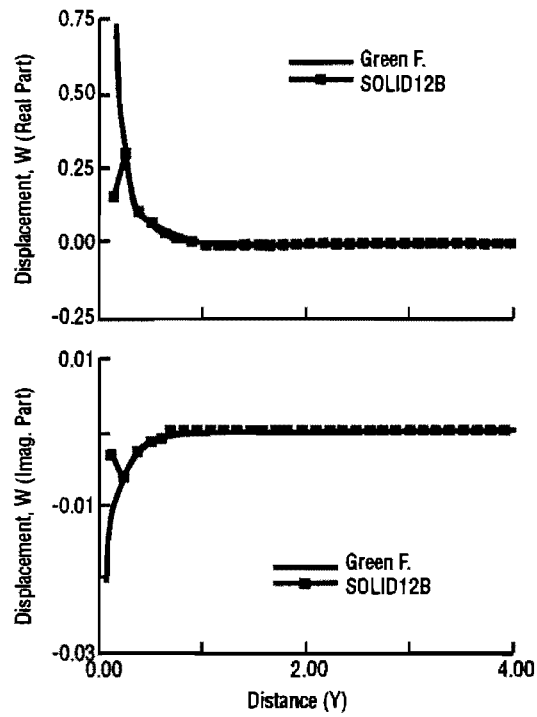

Figure 4.32 Comparison of the Green's function and the SOLID12B solutions with $\Delta x = \Delta y = 1/8$, $\Delta z = 1/2$, $N_x = 10$, $N_y = 128$, 1 percent damping at frequency 0 Hz

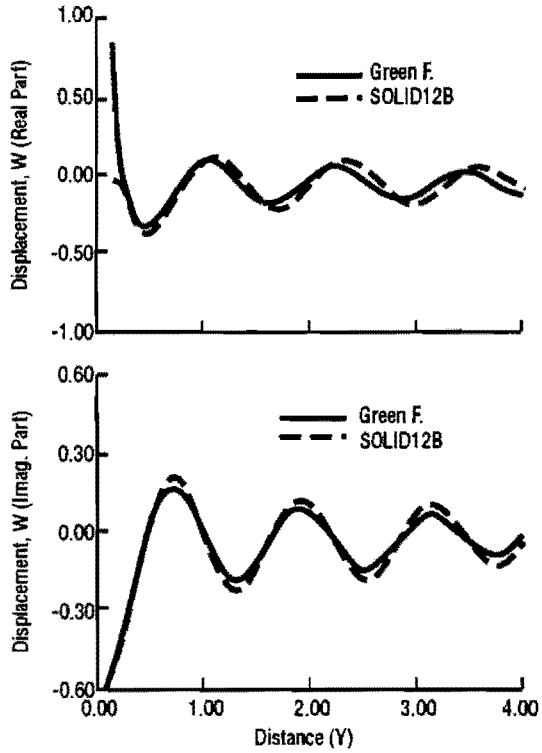

Figure 4.33 Comparison of the Green's function and the SOLID12B solutions with $\Delta x = \Delta y = 1/8$, $\Delta z = 1/2$, $N_x = 10$, $N_y = 128$, 1 percent damping at frequency 0.8 Hz

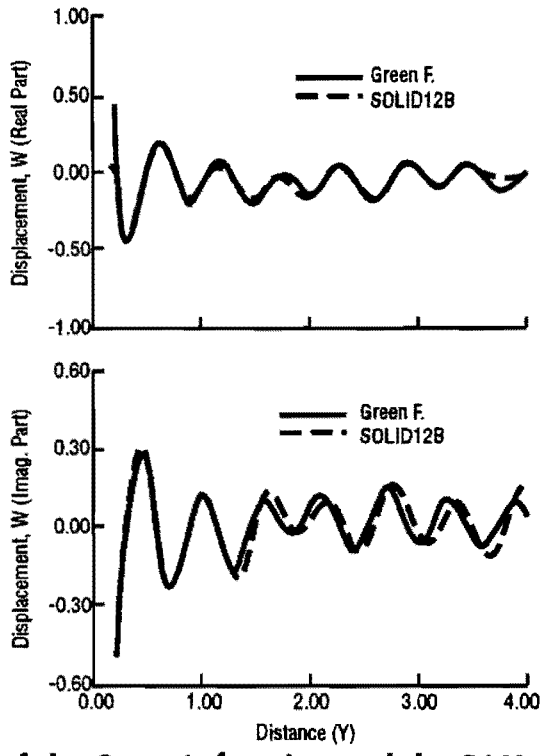

Figure 4.34 Comparison of the Green's function and the SOLID12B solutions with $\Delta x = \Delta y = 1/8$, $\Delta z = 1/2$, $N_x = 10$, $N_y = 128$, 1 percent damping at frequency 1.6 Hz

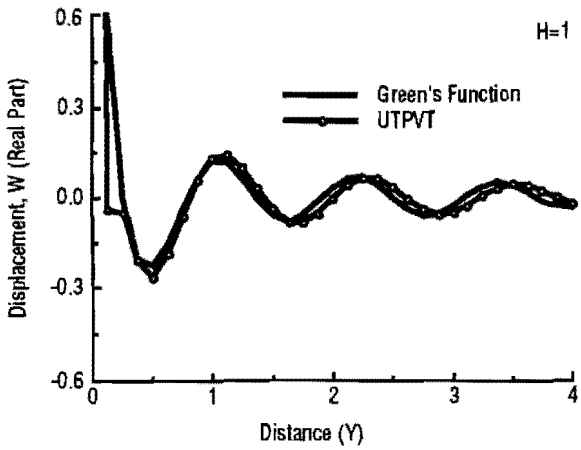

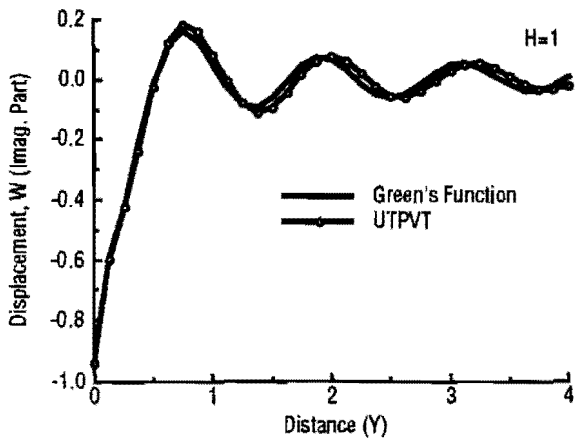

Figure 4.35 **Comparison of the Green's function and the SOLID12B solutions for a layer with thickness H = 1 over a half space with $\Delta x = \Delta y = 1/8$, $\Delta z = 1/2$, $N_x = 10$, $N_y = 128$, 2 percent damping at frequency 0.8 Hz**

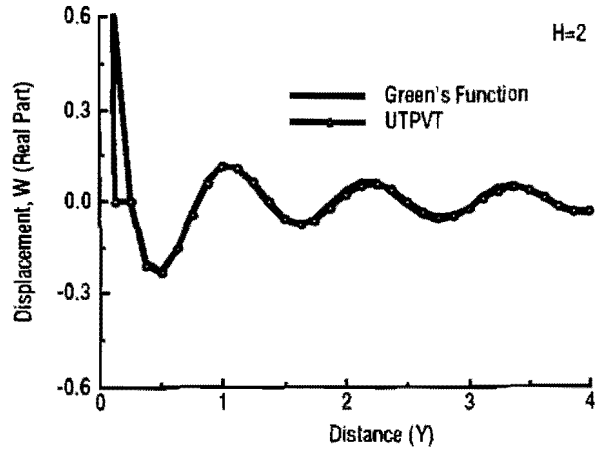

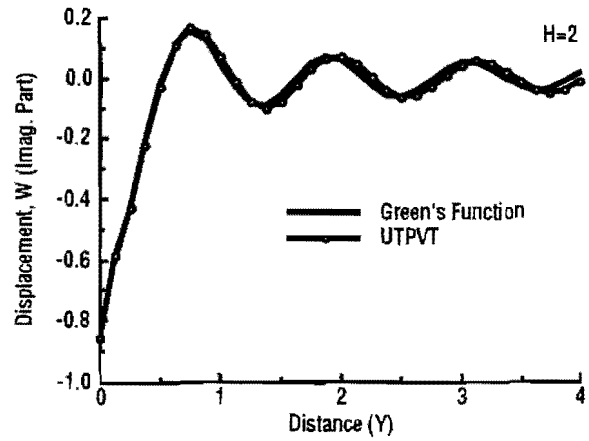

Figure 4.36 **Comparison of the Green's function and the SOLID12B solutions for a layer with thickness H = 2 over a half space with $\Delta x = \Delta y = 1/8$, $\Delta z = 1/2$, $N_x = 10$, $N_y = 128$, 2 percent damping at frequency 0.8 Hz**

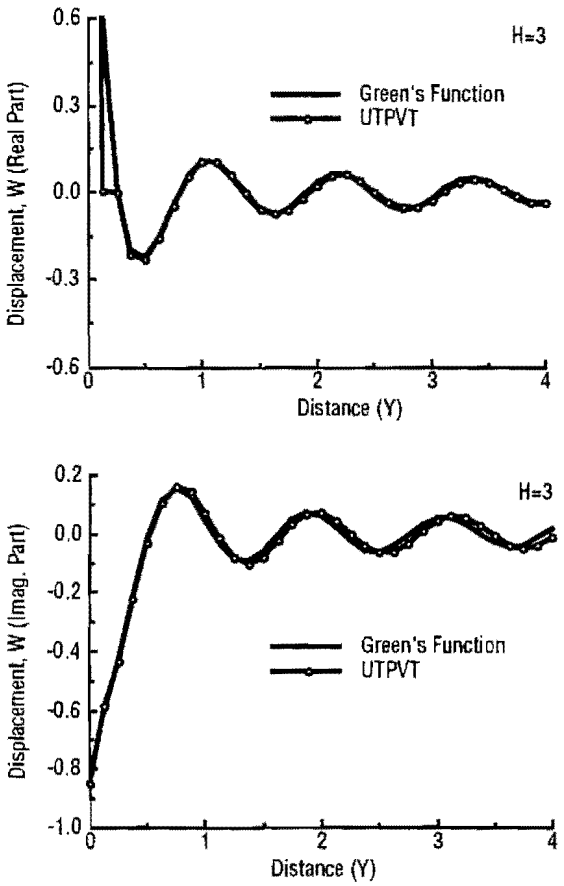

Figure 4.37 **Comparison of the Green's function and the SOLID12B solutions for a layer with thickness H = 3 over a half space with $\Delta x = \Delta y = 1/8$, $\Delta z = 1/2$, $N_x = 10$, $N_y = 128$, 2 percent damping at frequency 0.8 Hz**

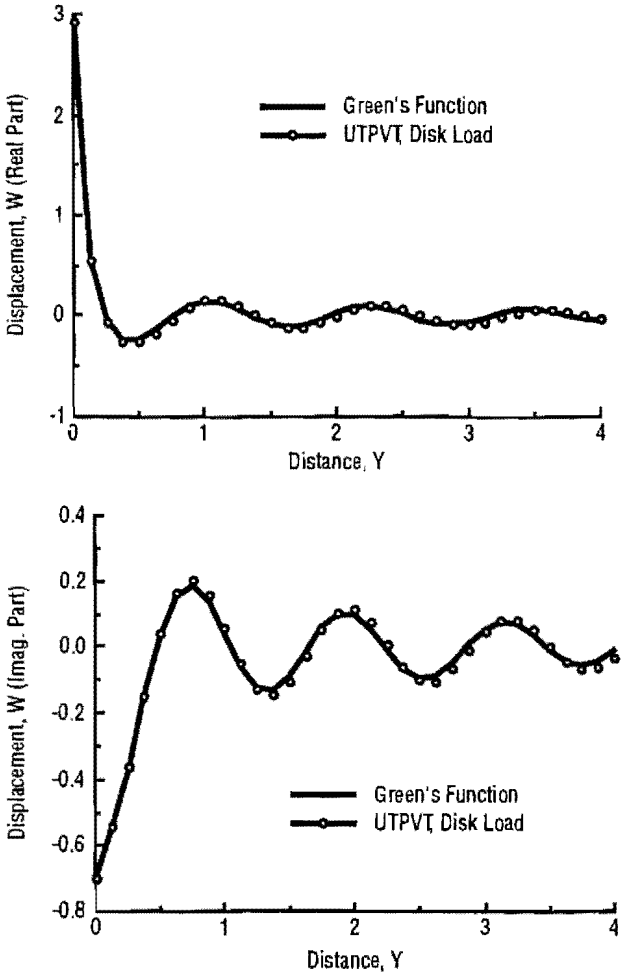

Figure 4.38 **Comparison of the Green's function and the SOLID12B solutions for a disk load in terms of real and imaginary with $\Delta x = \Delta y = 1/8$, $\Delta z = 1/2$, $N_x = 10$, $N_y = 128$, 2 percent damping at frequency 0.8 Hz**

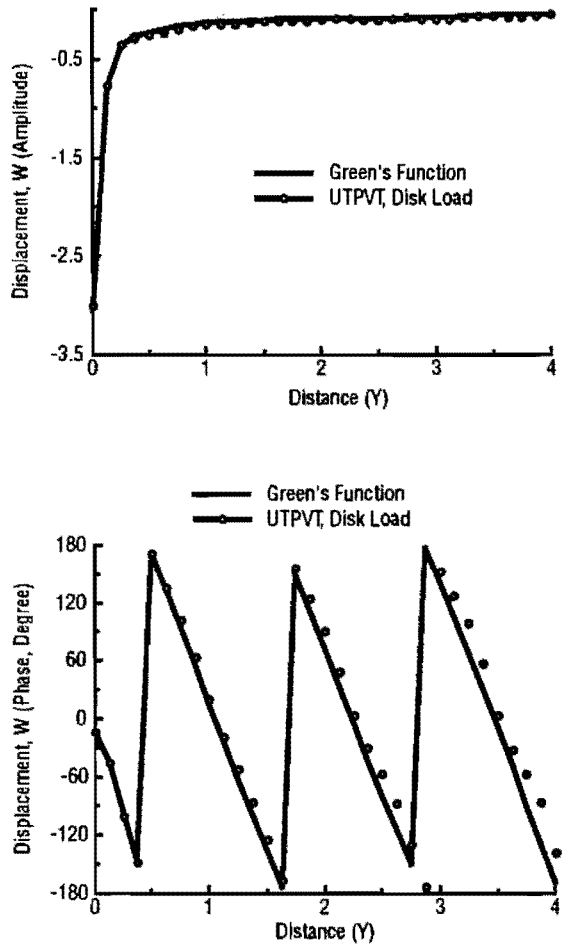

Figure 4.39 Comparison of the Green's function and the SOLID12B solutions for a disk load in terms of amplitude and phase with $\Delta x = \Delta y = 1/8$, $\Delta z = 1/2$, $N_x = 10$, $N_y = 128$, 2 percent damping at frequency 0.8 Hz

4.9 Summary

. Parametric studies have been conducted in this chapter to investigate key parameters in the formulation, such as type of element, number of sampling points, number of extension, element size, material damping, and bottom boundary. The element SOLID12B is found to be the best type of the element, since it has less trouble at small distances and less number of layers is needed to simulate the stratum without loss of accuracy. For damping ratio equal to 2% or larger, one can obtain results below 5% error within two wavelengths measured from the load by keeping the wavelength-element ratios $\lambda_R/\Delta y = 10$ and $\lambda_R/\Delta z = 2.5$ and using $N_y = 128$ and $N_x = 10$. For damping ratio less than 2%, it is suggested to use larger values for $\lambda_R/\Delta y$, $\lambda_R/\Delta z$, N_y, and N_x than those for damping ratio of 2%. With the dynamic rule above, the disk load of the soil-pavement formulation is in good agreement with Green's function. For half space bottom boundary, it was found that the viscous boundary will be in good agreement with Green's function by putting the half space at a depth of two wavelengths.

CHAPTER 5. APPLICATION OF SOIL-PAVEMENT FORMULATION TO NONDESTRUCTIVE TESTS

5.1 Introduction

This chapter presents an application of the soil-pavement formulation to the nondestructive testing of pavements. The aim of this chapter is to determine the significance of the lateral boundary on the measured deflections.

Three typical in-service pavement sections were selected as the test sites for analysis. They are road FM 137 in Paris, Texas; Interstate Highway 10 in El Paso, Texas; and Route 1 in Austin, Texas. Detailed information on these sites is included in Section 5.2. The results of the Dynaflect, the FWD, and the SASW test simulations are presented in Sections 5.3, 5.4 and 5.5, respectively.

5.2 Description of the Test Sites

Figures 5.1 through 5.4 depict the cross-sections of the three test sites selected. For simplicity, road FM 137 and Interstate Highway 10 were designated as profile 1 and profile 2. On Route 1, the test site was selected on the ramp which is supported by two retaining walls. It was considered interesting to investigate the influence of the retaining walls on the measured deflections. Therefore, two profiles were studied for this site. The section without the walls was named profile 3. The one including the walls was named profile 4.

Each pavement section is modeled as a multilayer system surrounded by soil. The layer thicknesses of the test sites are given in Table 5.1. No information was available concerning the thickness of the subgrade above bedrock for each section. Various thicknesses were assigned for analysis as listed in Table 5.1. Complete analyses were done for the Dynaflect test since only one frequency is involved, but due to computational costs, only one value of the subgrade thickness was used for the FWD and the SASW tests. The material properties are also given in Table 5.1. For simplicity, Poisson's ratios, the unit weights and the material dampings were assumed to be 0.333, 120 pcf and 2 percent.

The effect of lateral boundary was studied by varying the test loading position d which is the distance measured from the edge of the pavement (Figure 5.1). For the Dynaflect test, 5 positions were studied (d=1, 2, 4, 8, 12 ft). Only three loading positions (d=1, 4 , 12 ft) were used for the FWD and the SASW tests. In order to study the effect of neglecting the lateral boundary, the deflections of a continuous stratum are also obtained by assuming that the core region (including

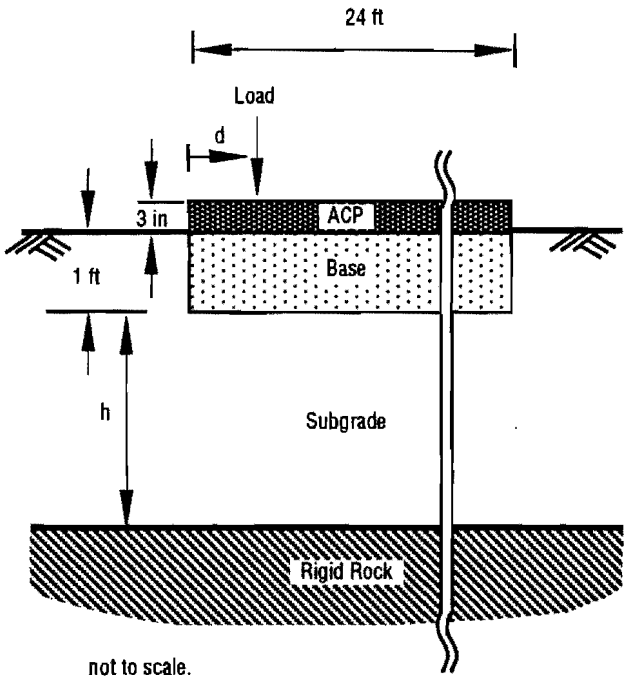

Figure 5.1 Idealized cross-section of the test site on Road FM 137, in Paris, Texas (Profile 1)

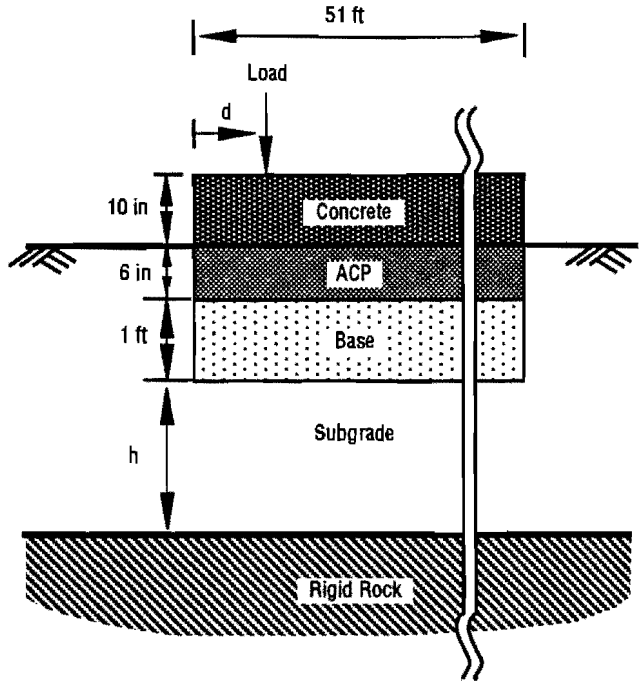

Figure 5.2 Idealized cross-section of the test site on Interstate Highway 10, in El Paso, Texas (Profile 2)

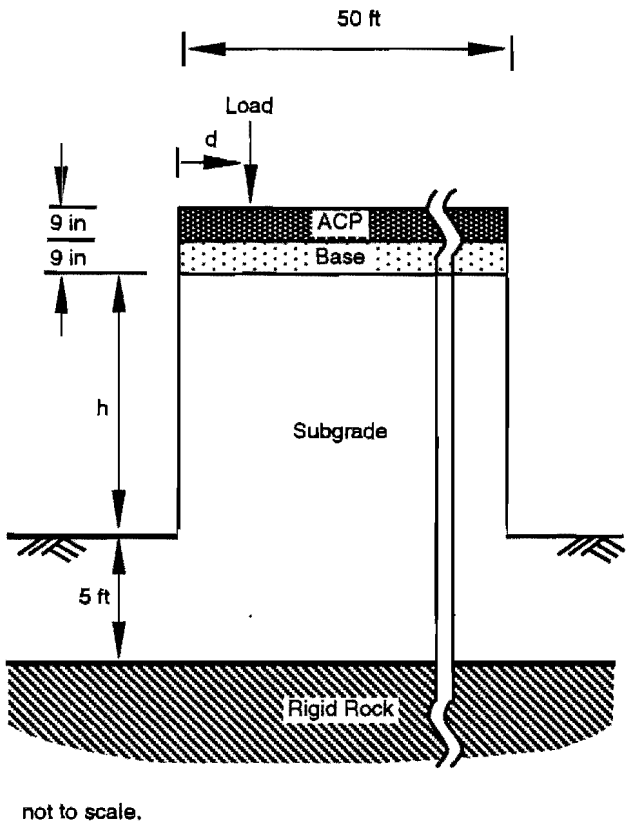

Figure 5.3 Idealized cross-section of the test site on Route 1, in Austin, Texas without the concrete retaining walls (Profile 3)

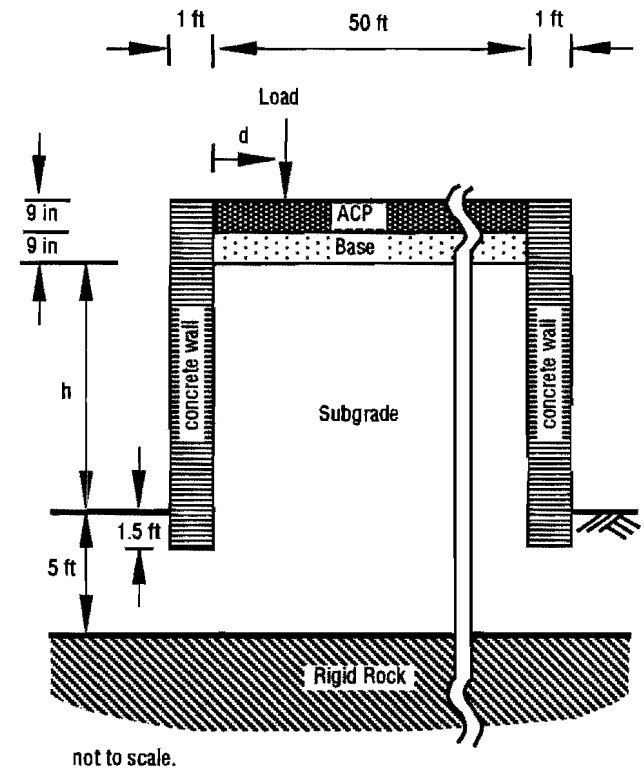

Figure 5.4 Idealized cross-section of the test site on Route 1, in Austin, Texas with the concrete retaining walls (Profile 4)

Table 5.1 Properties of three test sites

Site	Layer	Thickness (ft)	Young's Modulus (ksi)	Shear Wave Velocity (fps)
FM 137	Surface	0.25 (3 in.)	431	2,500
	Base	1	44	800
	Subgrade	8, 15, 31 (Dynaflect) 15 (FWD, SASW)	17	500
IH 10	Surface	0.833 (10 in.)	5,589	9,000
	Base	0.5 (6 in.)	431	2,500
	Sub-base	1	44	800
	Subgrade	8, 15, 31 (Dynaflect) 8 (FWD, SASW)	14	500
Route 1	Surface	0.75 (9 in.)	431	2,500
	Base	0.75 (9 in.)	44	800
	Subgrade	4, 10, 20 (Dynaflect) 4 (FWD, SASW)	17	500
	Subgrade	5	17	500
	Concrete Walls	1	5,589	9,000

the surface layer) extends horizontally to infinity. In other words, there would be no material variation in the horizontal directions for the continuous stratum.

5.3 Simulation of the Dynaflect Tests

The results of the Dynaflect test simulation on the four test profiles are presented in this section. For each profile, three different values of the subgrade thickness were used. The subgrade thicknesses h were assumed to be 8, 15, and 31 ft for profiles 1 and 2. For profiles 3,and 4, the subgrade thicknesses were assumed to be 4, 10, and 20 ft .

Figure 5.5a shows the deflection basins of profile 1 for h = 8 ft where the unit of the deflections (mils) is equal to a thousandth of an inch. In this figure, 6 deflection basins are included. They are the basins for the continuous stratum and 5 different loading positions. It can be seen that all basins collapse together. This implies that the deflection basins are insensitive to the lateral boundary for this profile. Although the lateral stiffness contrast is substantial in the surface layer, the thickness of this layer is very thin, compared with other layers. Therefore, the contribution of the surface layer to the global stiffness is insignificant. Also the stiffness contrast between the base layer and the surrounding subgrade is not large enough (800:500, in terms of shear wave velocity). Thus, the effect of the lateral boundary on the measured deflections is insignificant.

In order to investigate the differences between defection basins, deflection normalization was performed where the basin of the continuous stratum was used as the denominator. Figure 5.5b shows the normalized deflections for the 5 loading conditions. In this figure, when the normalized deflection is greater than one, it implies that the deflection at this station exhibits larger value than that of the continuous stratum. For example, in the case of d = 1 ft, the deflections at the near stations (1, 2, 3, 4) are larger but the deflections at the far stations (5, 6, 7) are smaller than those

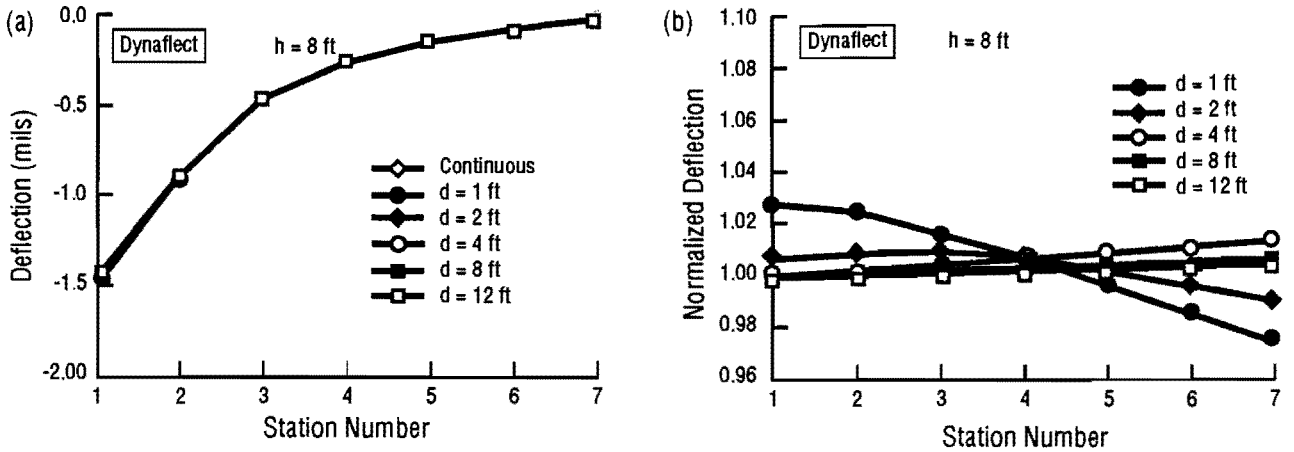

Figure 5.5 Dynaflect deflection basins and normalized deflections at various loading positions for Profile 1 with the thickness of subgrade h = 8 ft

of the continuous stratum. However, the differences are within 3 percent, and they become even smaller as the loading position moves away from the edge.

The results for h = 15 and h = 31 ft are presented in Figures 5.6 and 5.7. Again, the deflection basins are insensitive to the lateral boundary.

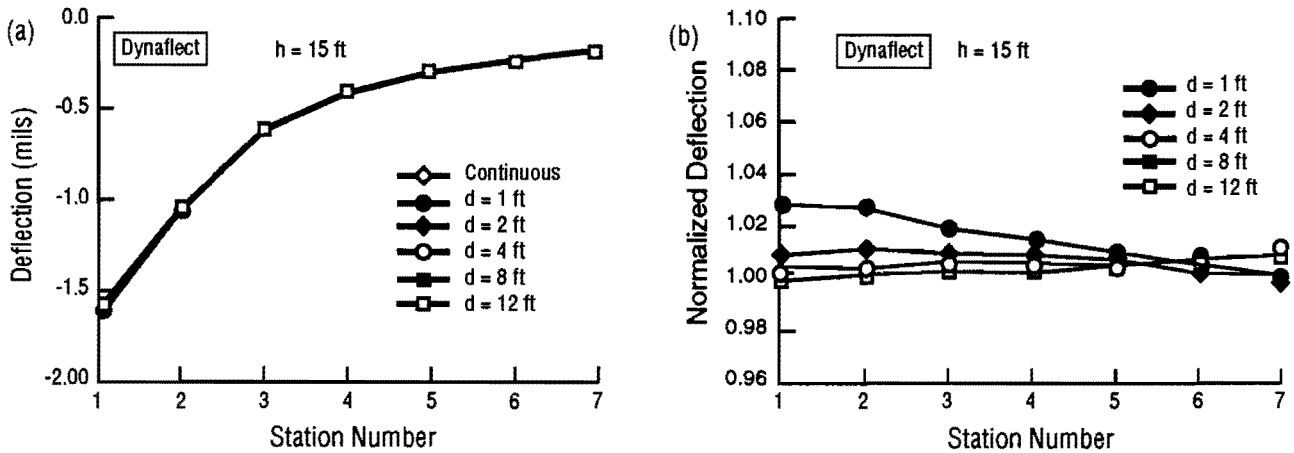

Figure 5.6 Dynaflect deflection basins and normalized deflections at various loading positions for Profile 1 with the thickness of subgrade h = 15 ft

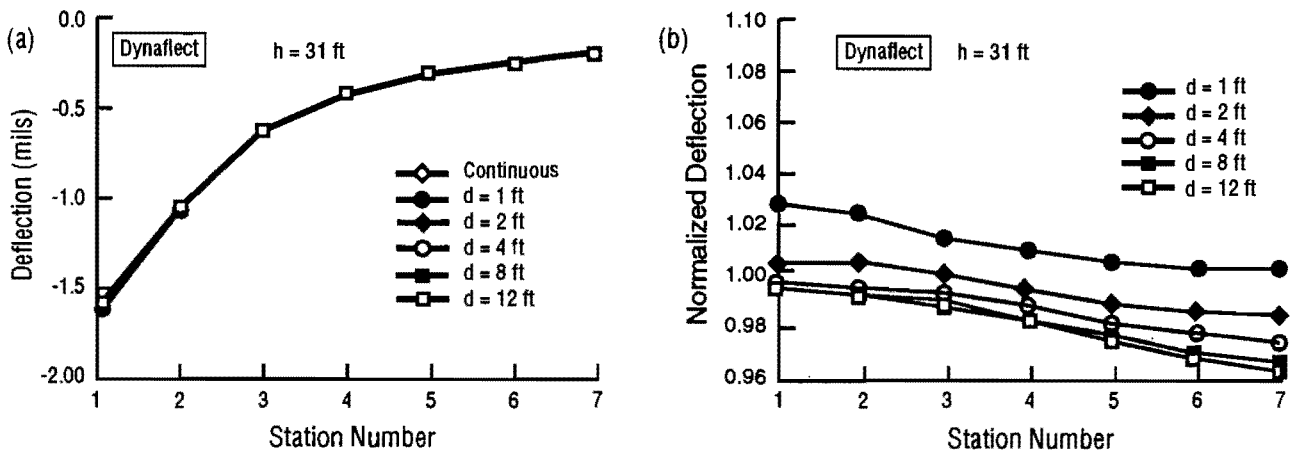

Figure 5.7 Dynaflect deflection basins and normalized deflections at various loading positions for Profile 1 with the thickness of subgrade h = 31 ft

Figures 5.8 through 5.10 show the results for profile 2 with h = 8, 15, and 31 ft. Now the influence of the lateral boundary can be seen easily on both the deflection and normalized deflection diagrams. For all h's, the differences between basins are around 50 to 70 percent at

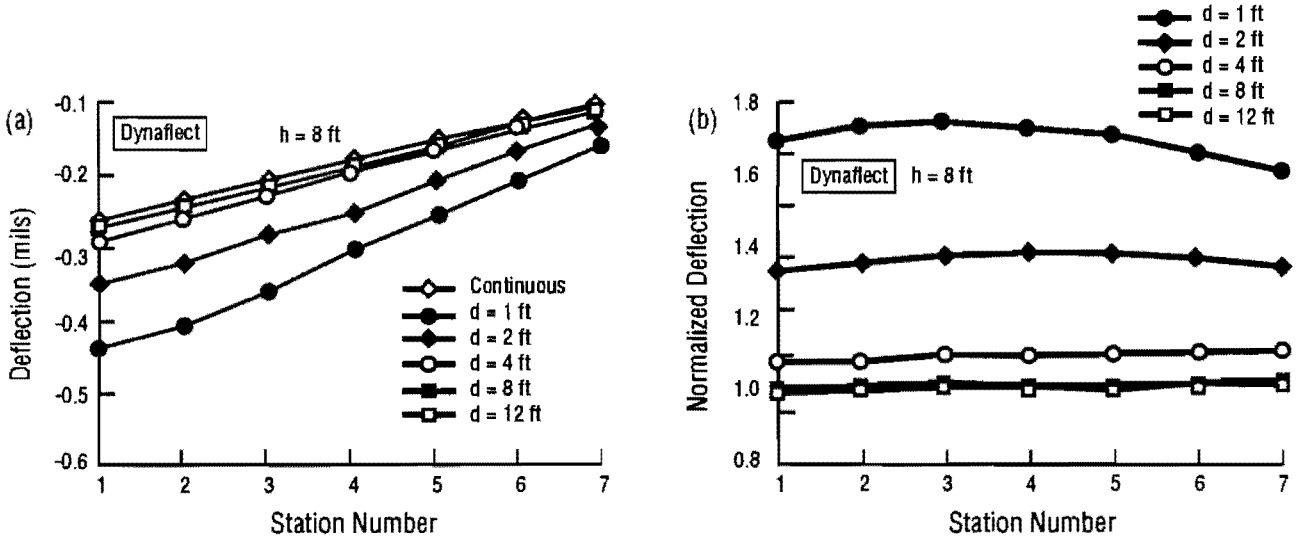

Figure 5.8 Dynaflect deflection basins and normalized deflections at various loading positions for Profile 2 with the thickness of subgrade h = 8 ft

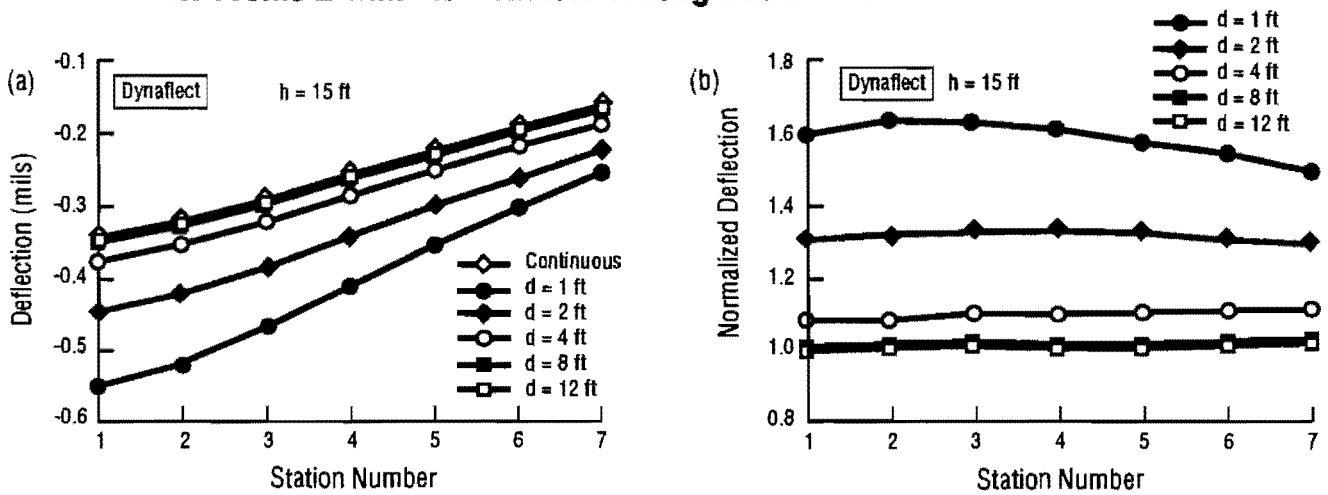

Figure 5.9 Dynaflect deflection basins and normalized deflections at various loading positions for Profile 2 with the thickness of subgrade h = 15 ft

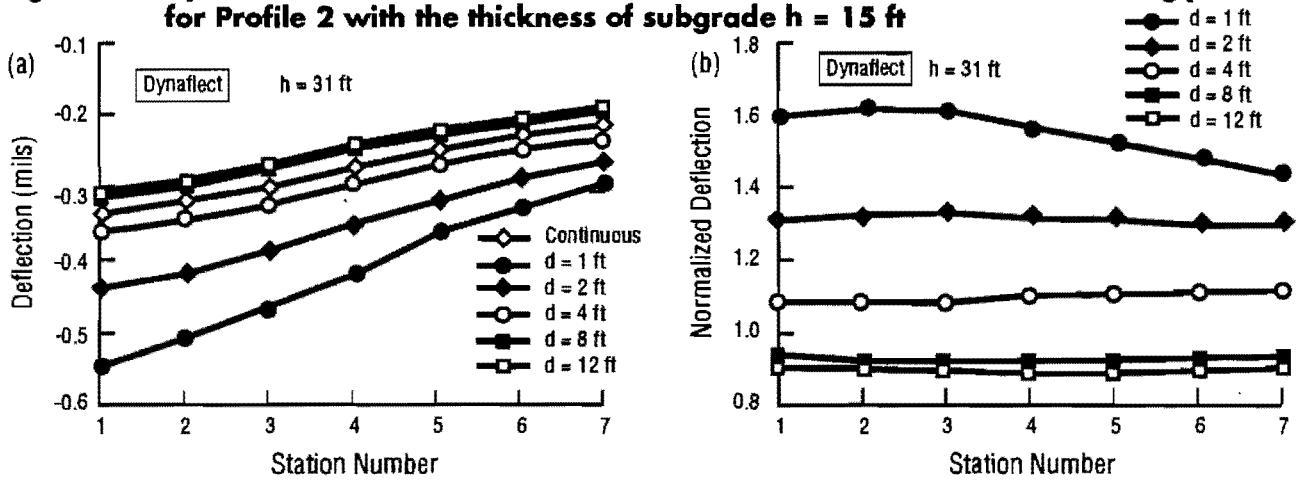

Figure 5.10 Dynaflect deflection basins and normalized deflections at various loading positions for Profile 2 with the thickness of subgrade h = 31 ft

the position d = 1 ft. This is due to the large thickness of the surface layer and the large stiffness contrast (2500:500) between the base and surrounding subgrade. The differences drop to 30 percent at d = 2 ft and 10 percent at d = 4 ft. Beyond d = 8 ft, the differences are basically within 5 percent.It should be noticed that the effect of the lateral boundary is not constant across the stations resulting in a change of the shape of the deflection basin. For h = 8 ft and d = 1 ft, the difference in deflection is about 70 percent at station 1, but decreases to 60 % for station 7. As the subgrade thickness increases, this differential influence seems to be more significant, but it decreases as the distance d increases for all thicknesses.

For profile 3, it can be seen in Figures 5.11a through 5.13a that the deflection basins increase when the height of the ramp increases. This is due to the lack of lateral support. From the normalized deflection diagram (Figure 5.11b), the difference in deflection can go from 55 to 90 percent at d = 1 ft for the short ramp. The difference is insignificant for d = 12 ft. For the medium and high ramps, the difference becomes more pronounced. For the high ramp with d = 1 ft, the difference varies from 80 percent to 125 percent. In this case even for d = 12 ft, the difference becomes significant (ranging from 20 to 60 percent).

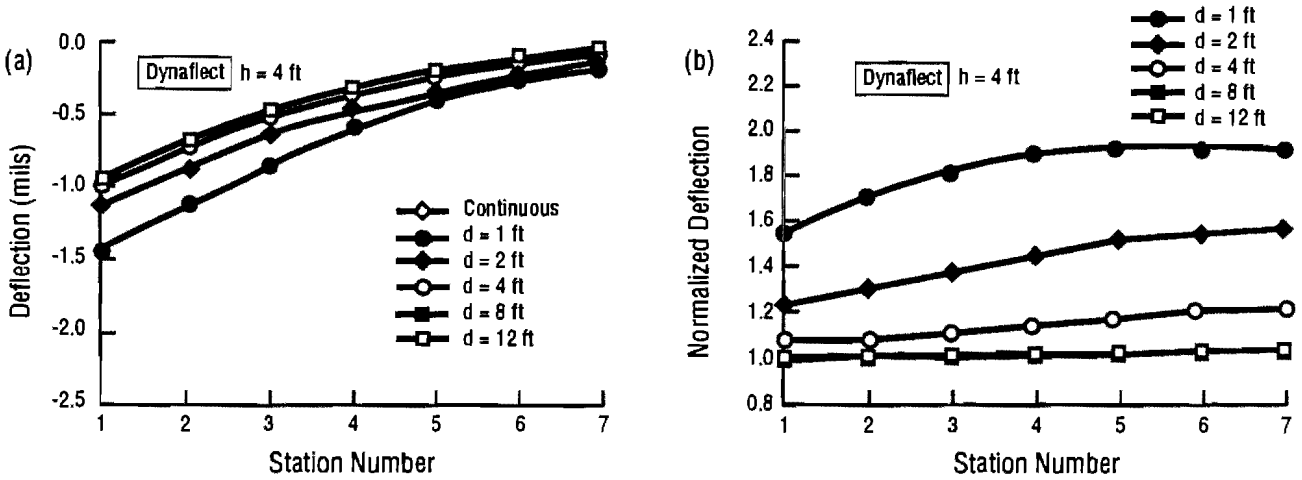

Figure 5.11 Dynaflect deflection basins and normalized deflections at various loading positions for Profile 3 with the thickness of subgrade h = 4 ft

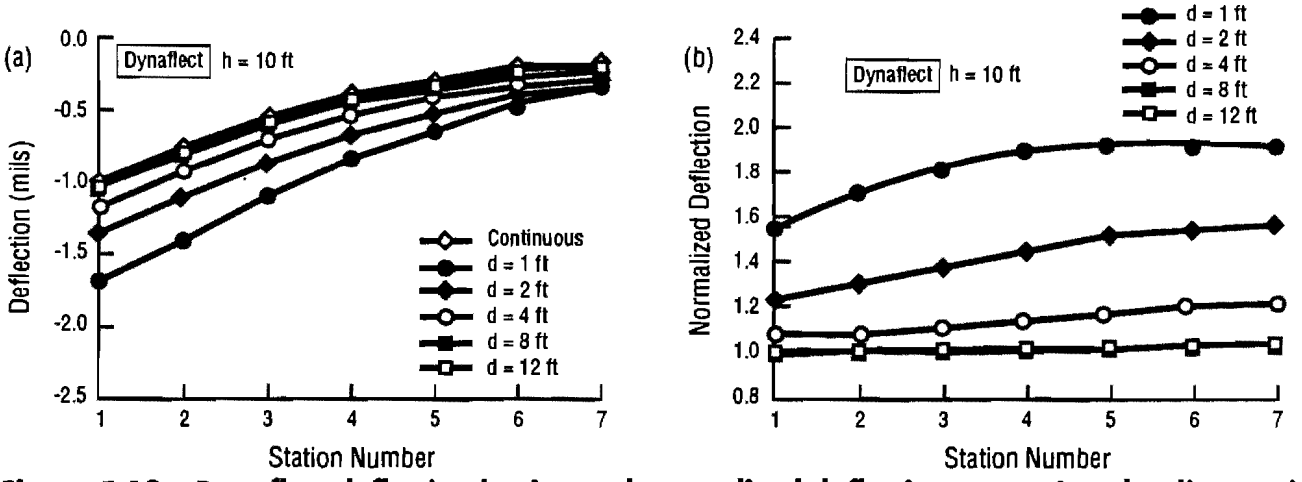

Figure 5.12 Dynaflect deflection basins and normalized deflections at various loading positions for Profile 3 with the thickness of subgrade h = 10 ft

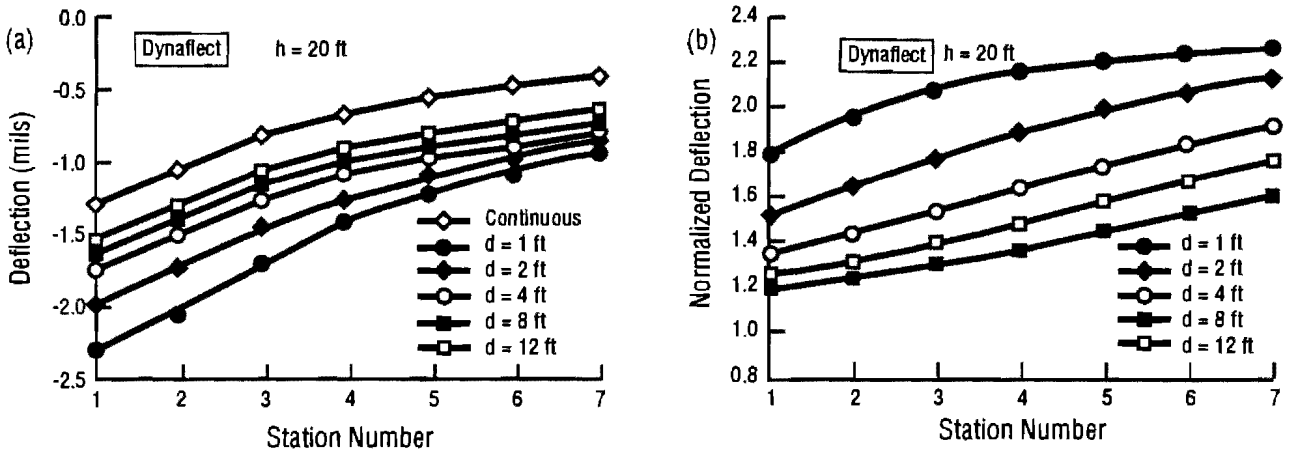

Figure 5.13 Dynaflect deflection basins and normalized deflections at various loading positions for Profile 3 with the thickness of subgrade h = 20 ft

The differential influence of the lateral boundary on the various stations is also more important. For instance, there is a difference of 130 percent at station 7 but only 70 percent at station 1 for the case with h = 10 ft and d = 1 ft.

Figures 5.14 through 5.16 show the results for profile 4. Since the core region is supported by the concrete retaining walls which are stiffer, the deflections exhibit smaller values when the loading position d moves closer to the edge. As the distance d increases, the basin become larger and converges to the one of the continuous stratum. The difference in deflections become larger again when the height of the ramp increases. The maximum difference between basins is about 90 percent.

Comparison of the basins of profiles 3 and 4 are presented in terms of deflection ratio which is equal to the deflection of profile 3 divided by that of profile 4. Figure 5.17 shows the deflection ratios for three different heights of the ramp. The effect of the lateral concrete walls versus a hypothetical free boundary is seen to be very significant. As the height of the ramp increases, both the difference in deflections between the two profiles and the differential influence on the stations

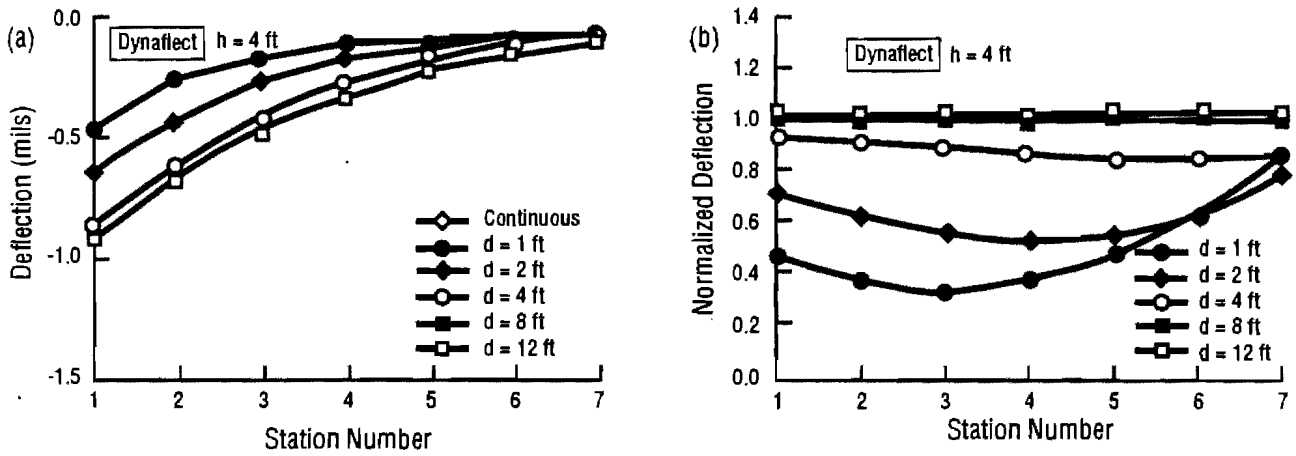

Figure 5.14 Dynaflect deflection basins and normalized deflections at various loading positions for Profile 4 with the thickness of subgrade h = 4 ft

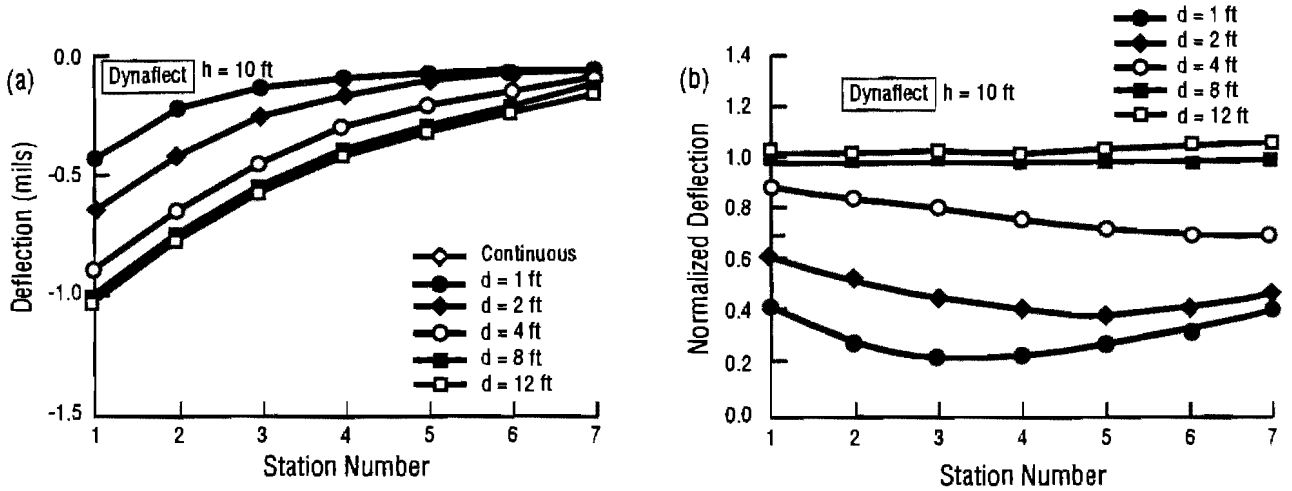

Figure 5.15 Dynaflect deflection basins and normalized deflections at various loading positions for Profile 4 with the thickness of subgrade h = 10 ft

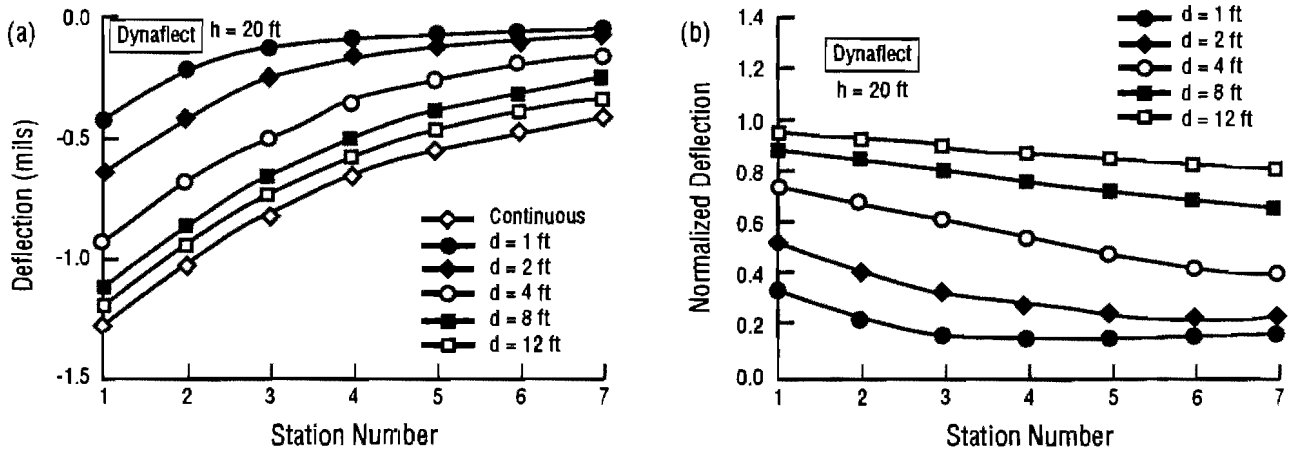

Figure 5.16 Dynaflect deflection basins and normalized deflections at various loading positions for Profile 4 with the thickness of subgrade h = 20 ft

increase. For example, the difference in deflection is about 30 percent at station 1 but 100 percent at station 7, even for d = 12 ft.

5.4 Simulation of the FWD Tests

Figure 5.18a shows the time history of the applied load used for the FWD simulations (a triangular impulse with a duration of 30 milliseconds and a peak amplitude of 10,000 lbs) and Figure 5.18b shows the amplitude of its Fourier transform. Most of the energy is on the range of frequencies from 0 to 50 Hz. Figure 5.19a shows, a comparison of the transfer functions obtained from the Greens' functions and the UTPVT program at station 2 for a continuous stratum of profile 3 with subgrade thickness h = 4 ft. Theagreement between the two solutions is quite good, especially at the first peak which occurs around 22 Hz. Figure 5.19b shows the time histories of the displacements at station 2 for both solutions. They are in excellent agreement. Notice that the unit of the deflections for the FWD test is mils per kip (i.e. they are divided by a value of 10 to refer them to the same force applied in the Dynaflect test later). The time records of all stations

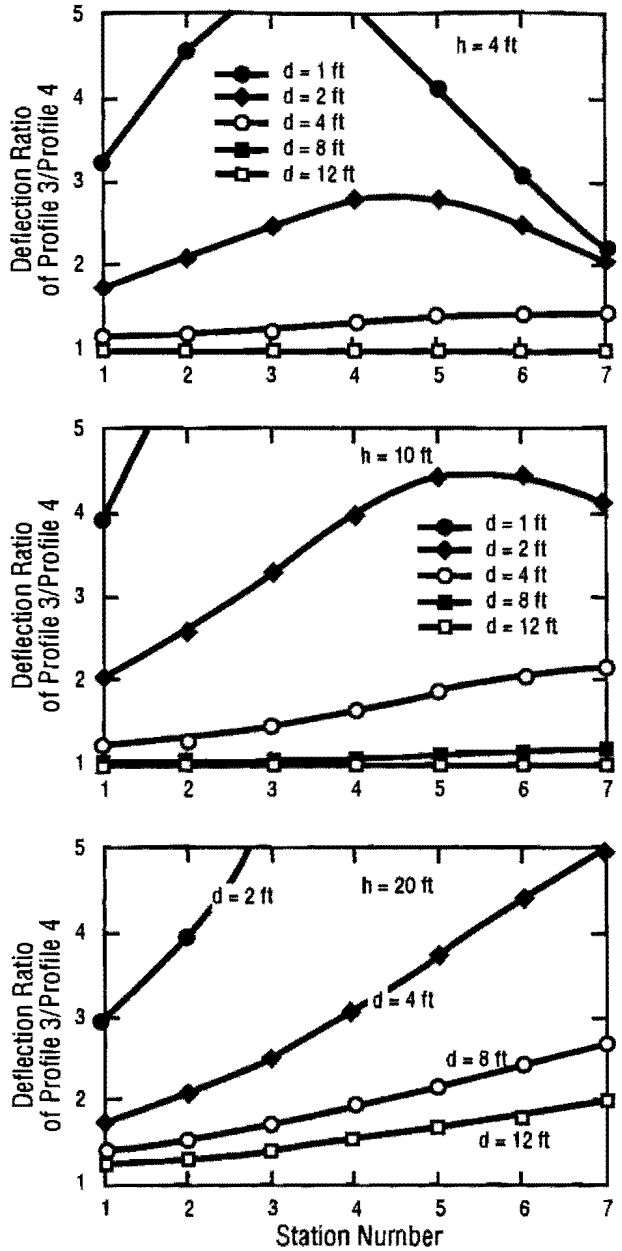

Figure 5.17 Dynaflect deflection ratios of Profile 3 over Profile 4 at various loading positions for the thicknesses of subgrade h = 4, 10, and 20 ft

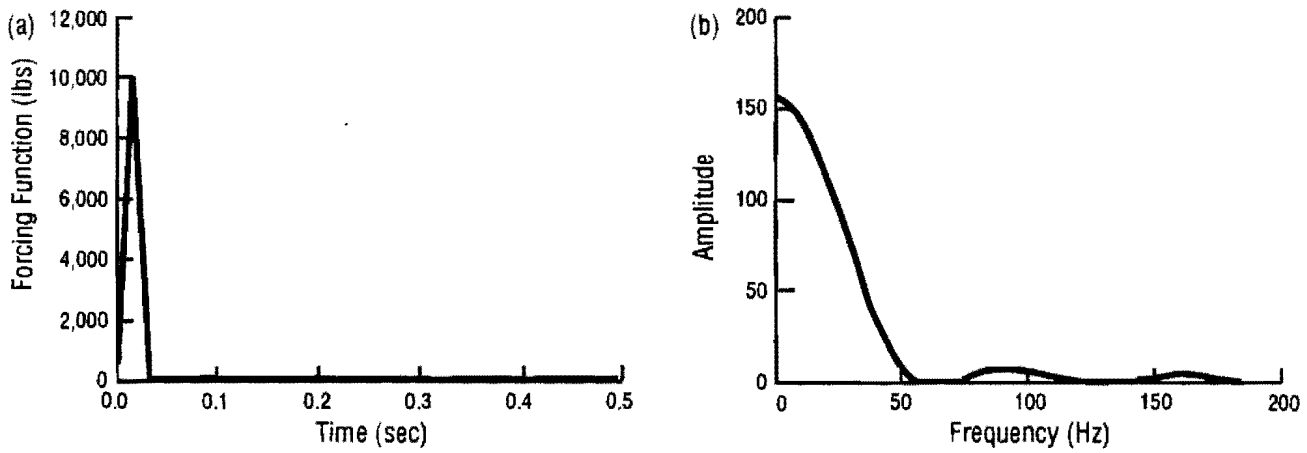

Figure 5.18 FWD forcing function in the time and frequency domains

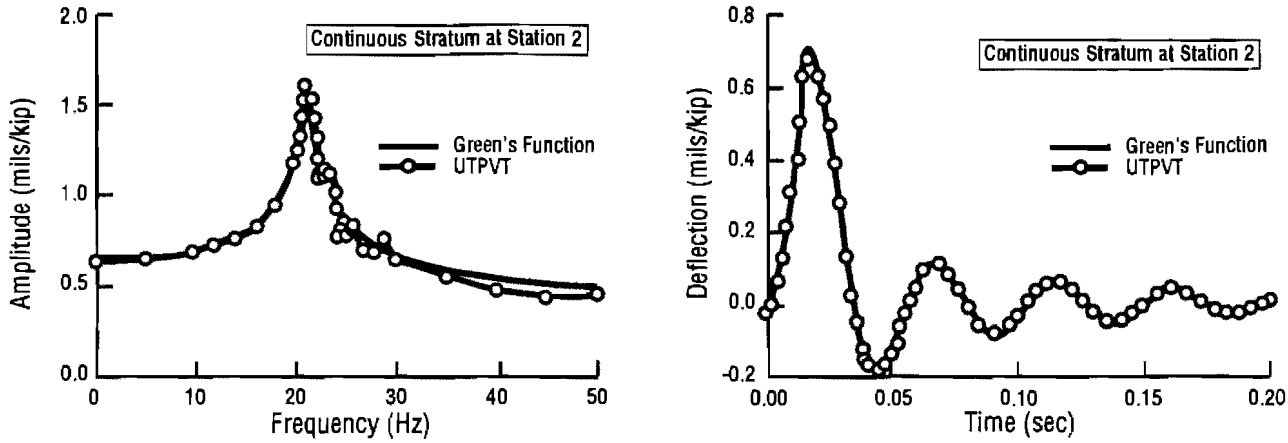

Figure 5.19 Comparison of the Green's function and UTPVT solutions for the transfer functions and time histories at Station 2 for a continuous stratum in FWD test

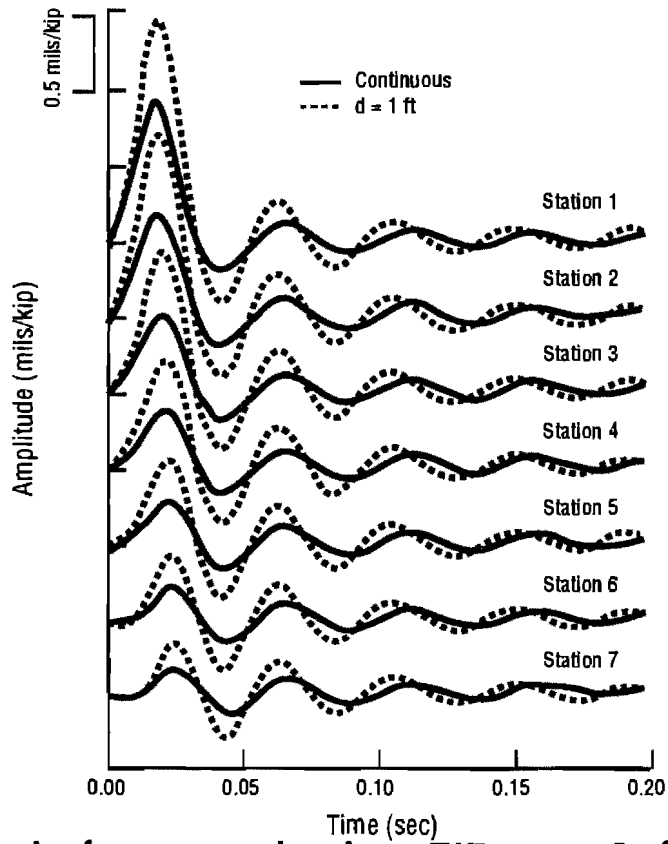

Figure 5.20 Time histories for seven stations in an FWD test on Profile 3 with h = 4 ft and loading position d = 1 ft

for profile 3 at a distance d = 1 ft are presented in Figure 5.20. The rest of the time records can be found in Appendix B. Only the peak deflections of the FWD test are presented herein.

Figures 5.21 through 5.24 show the results for profiles 1, 2, 3, and 4. The trends are generally similar to those reported for the simulation of the Dynaflect tests.

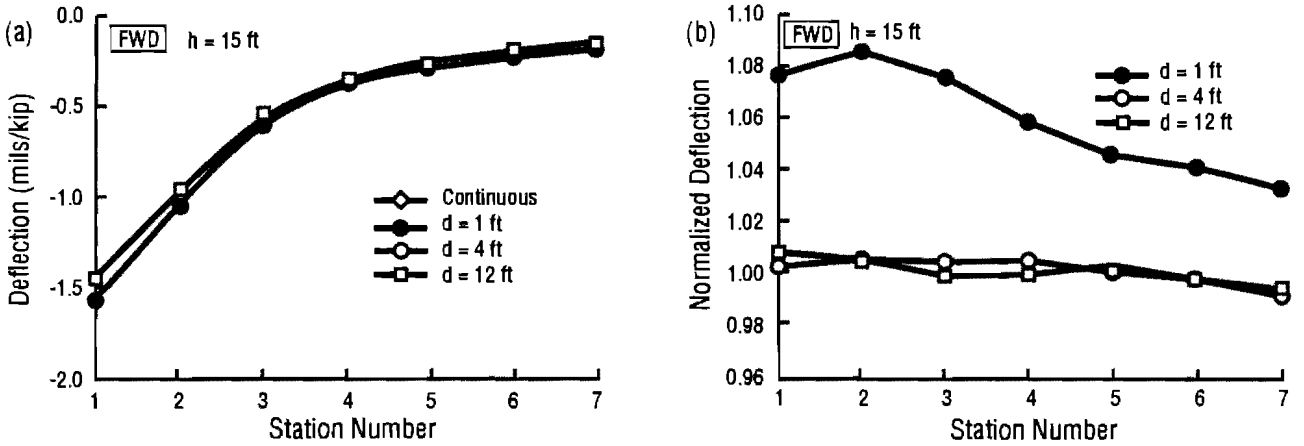

Figure 5.21 FWD deflection basins and normalized deflections at various loading positions for Profile 1 with the thickness of subgrade h = 15 ft

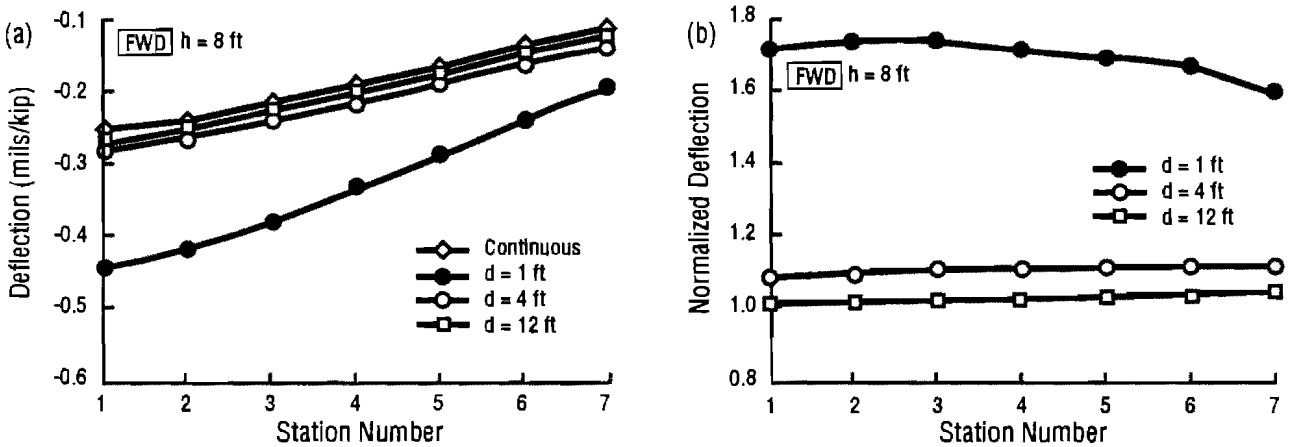

Figure 5.22 FWD deflection basins and normalized deflections at various loading positions for Profile 2 with the thickness of subgrade h = 8 ft

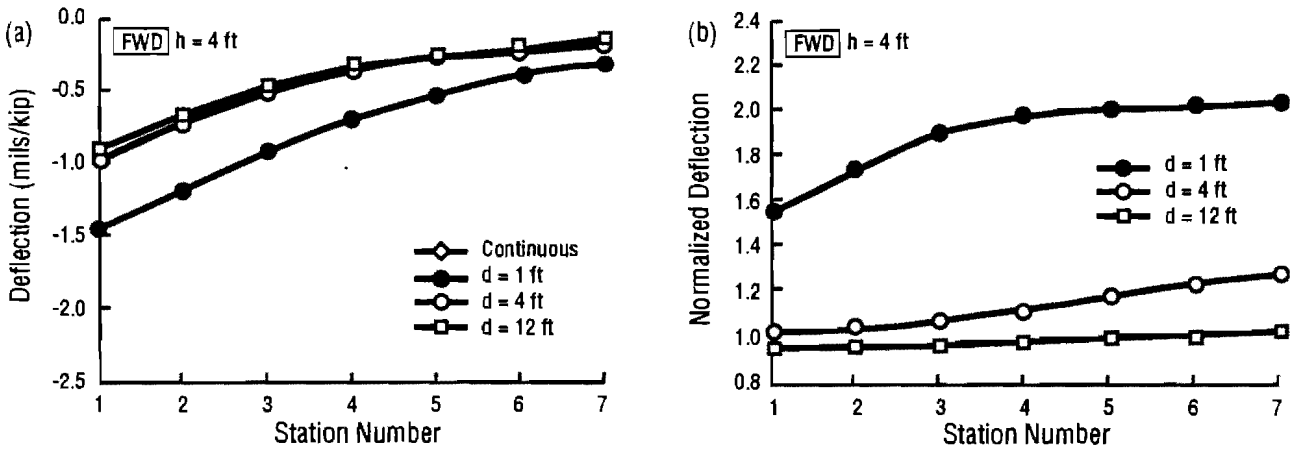

Figure 5.23 FWD deflection basins and normalized deflections at various loading positions for Profile 3 with the thickness of subgrade h = 4 ft

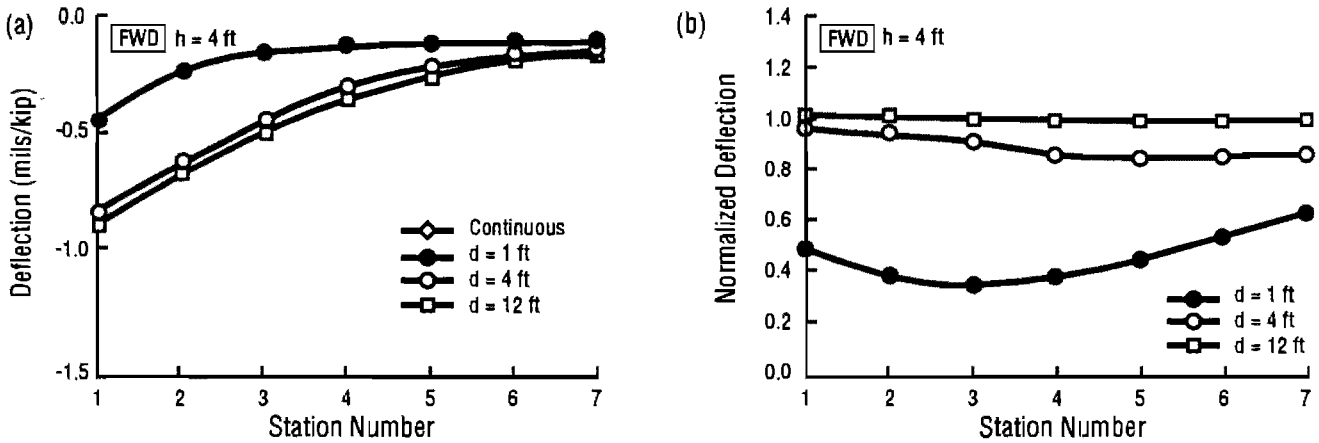

Figure 5.24 FWD deflection basins and normalized deflections at various loading positions for Profile 4 with the thickness of subgrade h = 4 ft

5.5 Simulation of the SASW Tests

As mentioned in Chapter Two, the SASW method uses the phase spectrum for the dispersion analysis. It differs from the Dynaflect and the FWD tests in many aspects. Therefore, no comparison could be made between the SASW method and other tests. The dispersion curves were obtained by using the spacing ratio d2/d1 = 2, as shown in Figure 2.8 and the d1 was taken to be one wavelength of the surface wave for each frequency. Several phase diagrams for receivers other than receivers d1 and d2 are included in Appendix C for whose who may wish to perform their own analyses on the dispersion data.

Figure 5.25a shows the dispersion curve of the continuous stratum for profile 1 with h = 15 ft. The average surface wave velocity for wavelengths less than 0.25 ft is about 2300 fps. If one multiplies this value by 1.1, one obtains a shear wave velocity of 2530, which is close to the shear wave velocity (2500 fps) of the surface layer. Some large fluctuations occur in the dispersion curve for wavelengths between 0.25 and 3 ft. Sánchez-Salinero (1987) and Sheu (1987) have observed similar phenomena in both theoretical and experimental data. The fluctuations are caused by the reflected body waves blended into the measured surface displacements due to the change in stiffnesses between layers. Despite the fluctuations, the dispersion curve starts to decrease as the wavelength increases and for a wavelength of 10 ft, the wave velocity is about 500 fps.

Figures 5.25b through 5.25d show the dispersion curves for three loading positions (d = 1, 4, 12 ft) along with the curve of the continuous stratum. For d = 1 ft, some very small deviations caused by the lateral boundary can be found for short wavelengths from 0.15 to 0.6 ft but the results are essentially unchanged in the average below 1 ft. Larger deviations can be seen for long wavelengths. This indicates, as expected, that the lateral boundary has more influence on the long wavelengths (low frequencies). For d = 4 ft, the deviation in the short wavelengths disappears while some minor deviation still remains in the range of long wavelengths. For d = 12 ft, the deviation becomes insignificant.

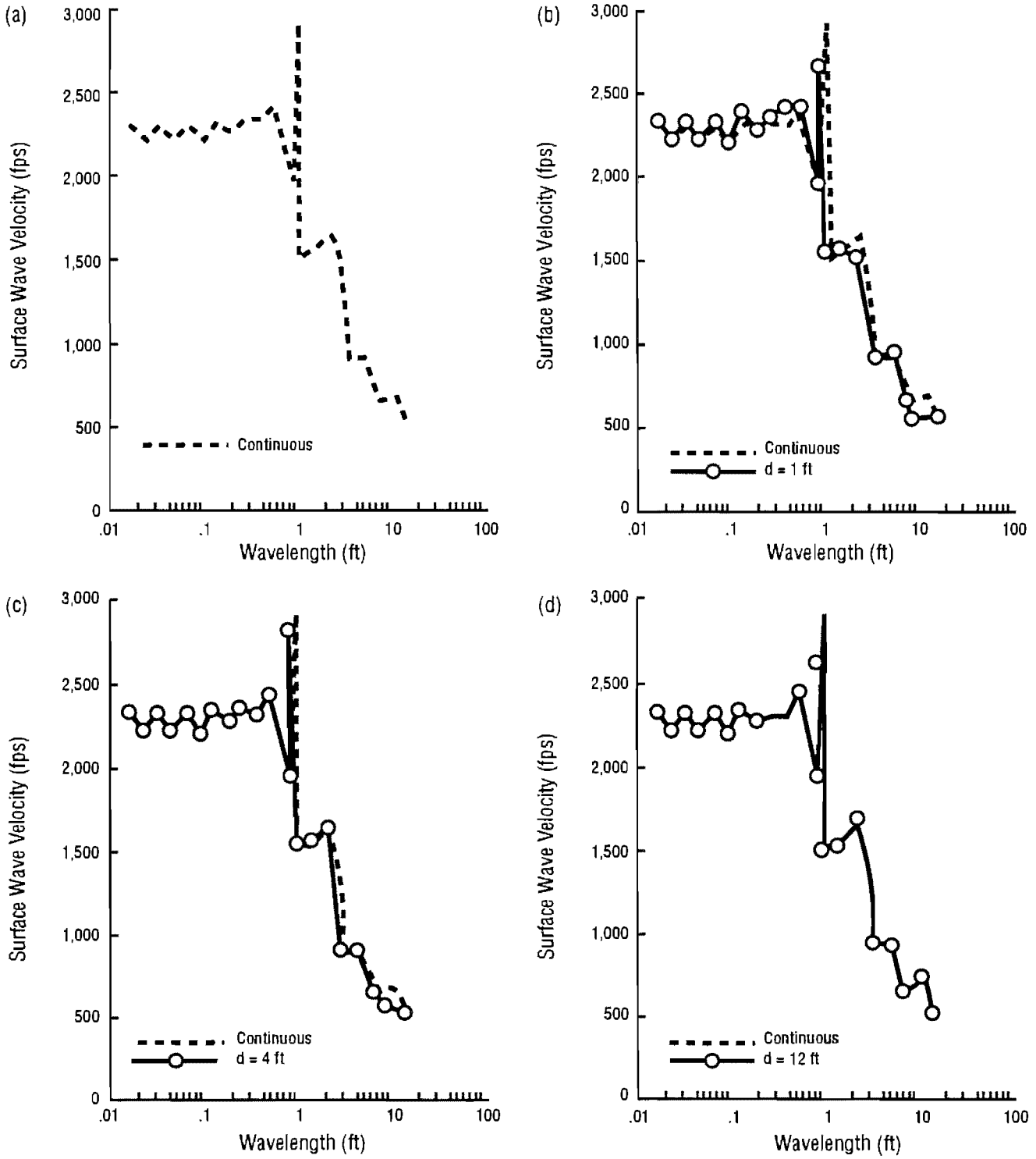

Figure 5.25 Dispersion curves of the continuous stratum and three loading positions for Profile 1

Figure 5.26 shows the dispersion curves for profile 2. The average surface wave velocity for wavelengths less than 0.83 ft is about 8,200 fps. Large fluctuations can be seen for wavelengths between 1 and 2 ft. By varying the loading position, again it was found that generally the lateral boundary has more influence on the long wavelengths.

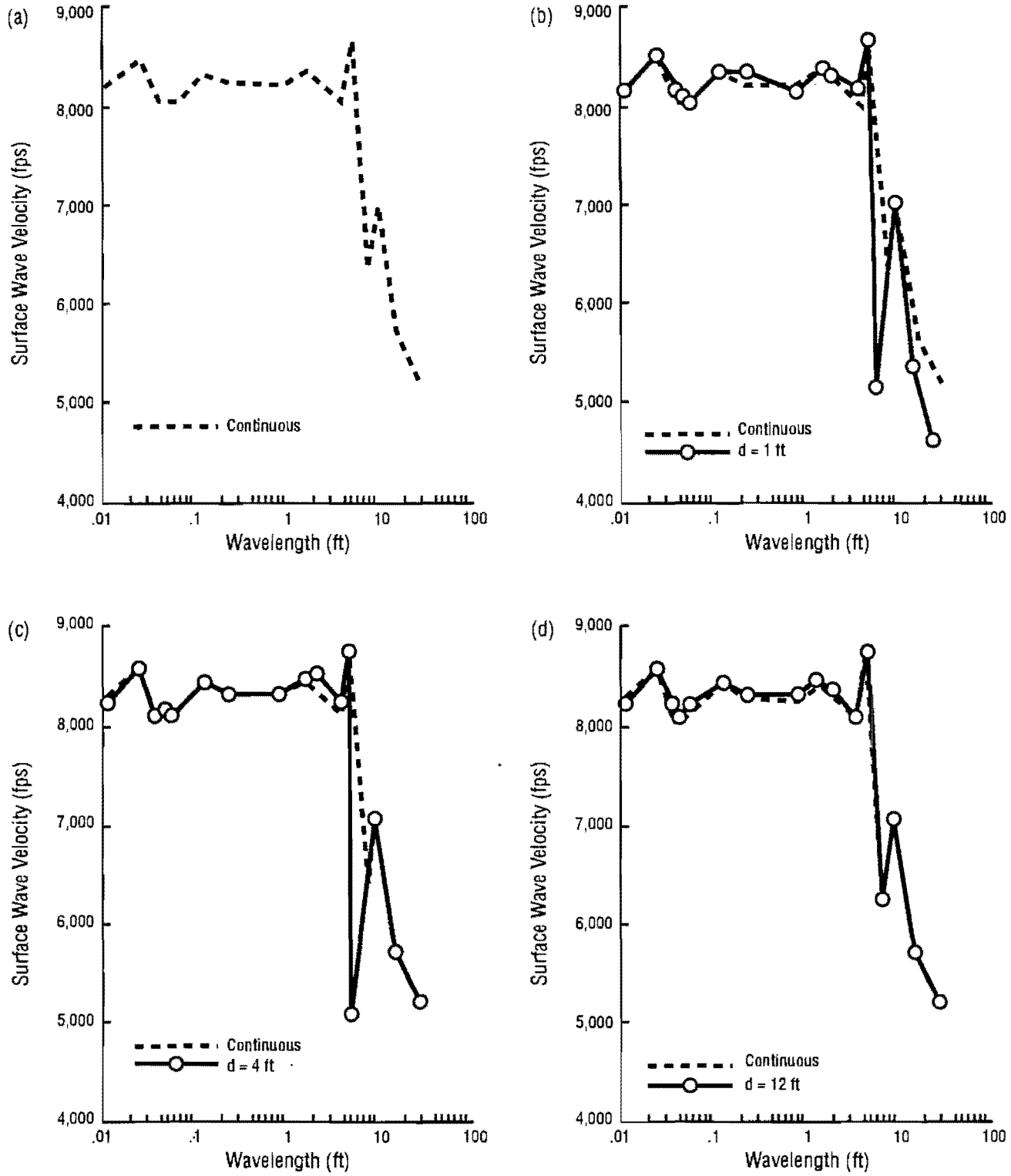

Figure 5.26 Dispersion curves of the continuous stratum and three loading positions for Profile 2

Similar comments apply to dispersion curves for profiles 3 and 4 (Figures 5.27 and 28). Figure 5.29 shows a comparison of the dispersion curves of profiles 3 and 4 for various loading positions.

It can be seen that the influence of the reflections from the lateral boundary can be seen easily at d = 1 ft and that the existence of retaining walls in profile 4 can cause larger fluctuations in the dispersion curves.

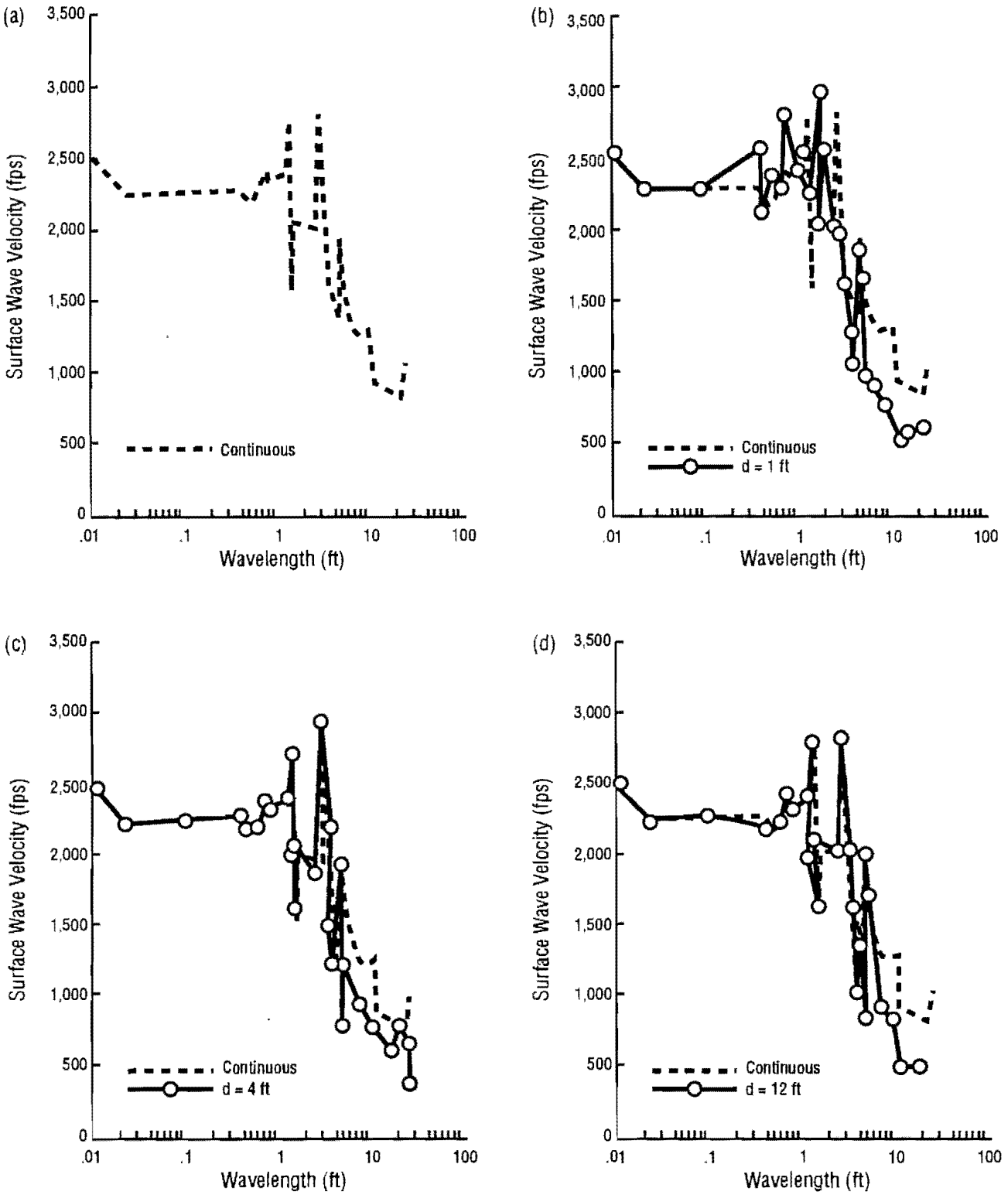

Figure 5.27 Dispersion curves of the continuous stratum and three loading positions for Profile 3

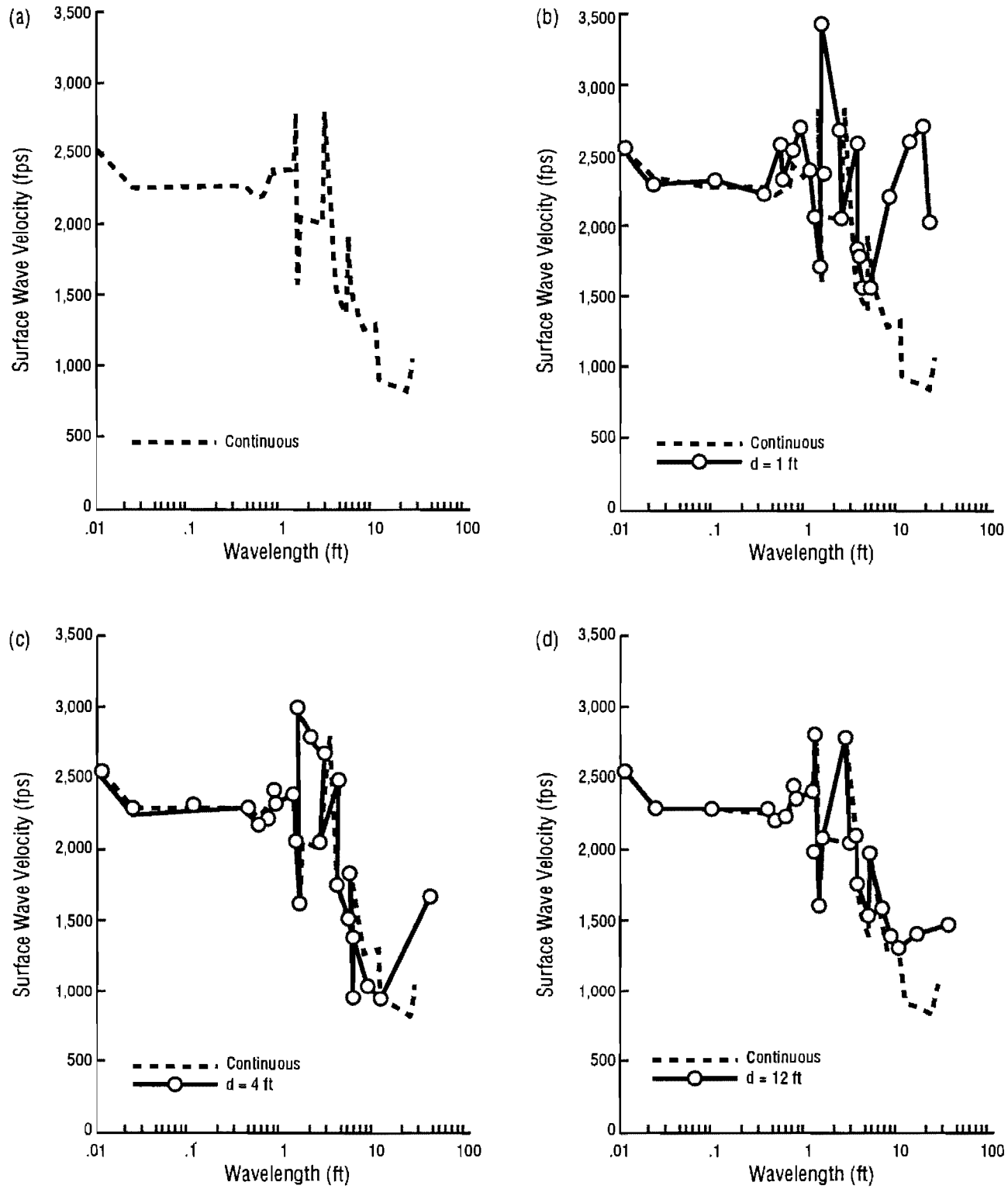

Figure 5.28 Dispersion curves of the continuous stratum and three loading positions for Profile 4

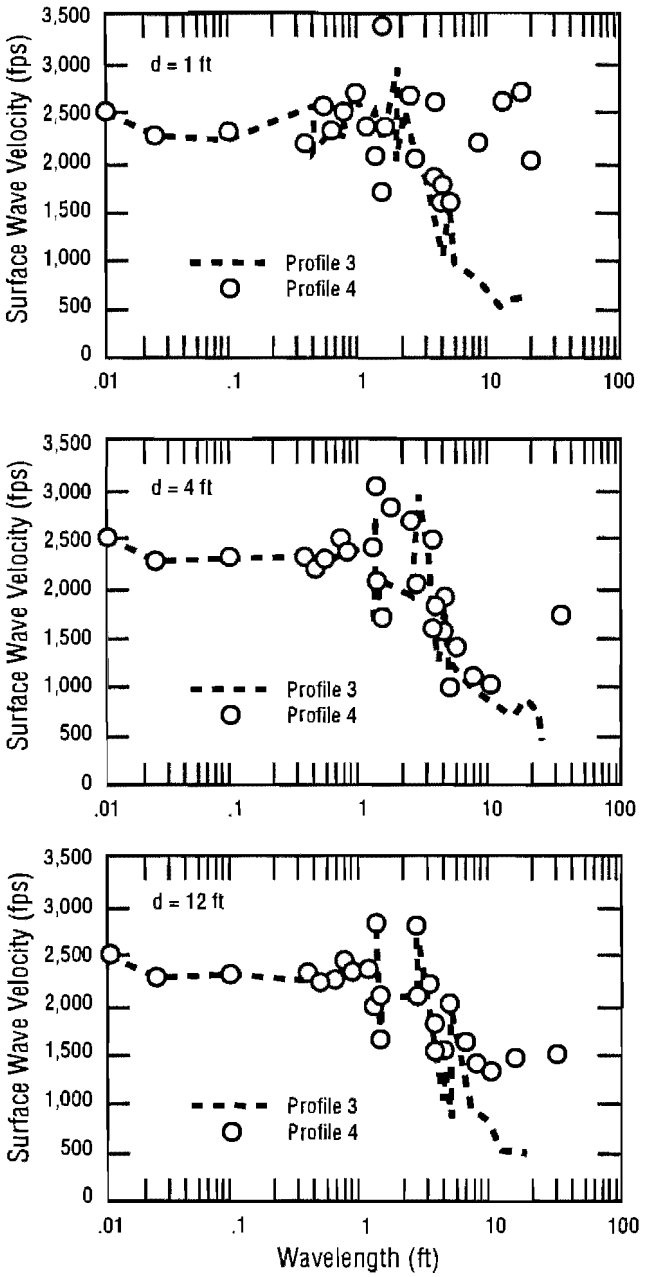

Figure 5.29 Dispersion curves of three loading positions for Profiles 3 and 4

5.6 Summary

The application of the soil-pavement formulation to the interpretation of the results of nondestructive testing of pavements has been presented in this chapter. The computer program UTPVT was used to assess the importance of the lateral boundary on the measured deflections. The Dynaflect, the FWD, and the SASW tests were simulated on three actual pavement sections. The three test sites are road FM 137, Interstate Highway 10, and the ramp on Route 1. The effects of the lateral boundary were studied by varying the testing loading position, d, measured from the edge of the pavement. For comparison purposes, the results of a continuous stratum were also presented. Different thicknesses of subgrade, h, were assign to each section in order to study

also the influence of the depth to bedrock in the Dynaflect test. However, due to the cost of computation, only one value was used for the thickness of subgrade in the FWD and the SASW tests.

In the Dynaflect tests, the results indicate that the influence of the lateral boundary on the measured deflections strongly depends on: (1) the loading position; (2) the thickness of the surface layer; (3) the lateral stiffness contrast between the base and the surrounding soil. A closer position, a larger value of the thickness, and a higher contrast will cause a larger influence of the lateral boundary. It was found that the basins for all positions are insensitive to the lateral boundary on road FM 137. The maximum error induced by neglecting the lateral boundary is within 5 percent. Significant error may occur, however, on Interstate Highway 10. At the position of d = 1 ft, the error can range from 50 to 70 percent. However, beyond d = 8 ft, the error drops to 5 percent. It was found also that the lateral boundary may have differential influence on various stations which will, in turn, change the shape of the basins. This differential influence becomes more pronounced when the loading is closer to the edge.

For the ramp on Route 1, the results show that the error caused by neglecting the lateral boundary and the change in the basin shape will increase as the height of the ramp increases. The existence of the retaining walls is also important on the measured deflections, especially for the high ramp. For example, the error induced by neglecting the walls is still about 30 percent at station 1 even when the load is located at 12 ft for the high ramp.

In general, similar trends can be observed in the FWD tests as were found in the Dynaflect tests. For these particular cases studied, the dynamic effects seem to be more important for the FWD tests.

The SASW simulations were conducted based on the spacing ratio of d2/d1 = 2. The results indicate that in general the dispersion curve follows the trend of the shear wave velocity profile. In the case of the continuous stratum, reflected body waves at the horizontal interfaces resulted in large fluctuations in the dispersion curves. The existence of the lateral boundary can cause more fluctuations, especially for long wavelengths.

CHAPTER 6. SUMMARY, CONCLUSIONS, AND RECOMMENDATIONS

6.1 Summary

Nondestructive testing for structural evaluation of pavements plays an important role for highway engineers in selecting rehabilitation and reconstruction strategies. Many traditional methods of structural evaluation are originally based on limiting deflection criteria by empirically correlating pavement performance with the measured deflections. Considerable efforts are under way to develop a more rational and mechanistic approach for structural evaluation. While there are still some problems which have not yet been fully resolved, especially in the interpretation of the data from nondestructive tests and in the inversion process, an appropriate forward model can be used not only as a research tool to study the important variables, but also as a design tool to determine the structural adequacy of pavements.

The three-dimensional elastodynamic solution for a layered half space is the formulation that has been used until now in the interpretation of results from dynamic testing of pavements. It assumes that each layer has infinite dimension in the horizontal plane. Therefore, material variations in the horizontal directions cannot be considered in this model. However, a highway road has a finite width in its transverse direction and variation in material properties between the road and the surrounding soil is not uncommon. Hence, an appropriate model which can account for the existing lateral boundary conditions is necessary to assess the significance of the finite pavement width on the measured deflections.

The primary goal of this study was to develop a mathematical model which could take into account not only the dynamic nature of the loads, but also the variation of material properties in the soil-pavement system. The soil-pavement structure was modeled as a layered stratum resting on bedrock or a half space. The pavement, base and subgrade were represented by a finite-element core region. An expansion technique was developed to obtain the stiffness matrix for the infinite lateral region. A viscous boundary was implemented to simulate the bottom boundary for a half space. Fourier superposition technique was applied to both the time variable and the longitudinal spatial coordinate of the

road. The stiffness matrices and load vectors were obtained in the frequency-wavenumber domain. Point load and disk load solutions were implemented into a computer program called UTPVT.

6.2 Conclusions and Recommendations

A number of parametric studies were conducted in order to assess the accuracy of the formulation, comparing the results to those provided by the Green's functions for the case where the material properties are constant in the horizontal direction. From these studies, it was concluded that:

(1) In the study of four types of finite elements developed in this study, the element SOLID12B, which is linear in the x- and y-directions and quadratic in the z-direction, was found particularly attractive, providing good agreement in results for the displacements close to the point load and requiring less layers to simulate the stratum without loss of accuracy.

(2) For damping ratio equal to 2 percent or larger, one can obtain the displacements with less than 5 percent error within two wavelengths from the load by keeping the element-wavelength ratios $\lambda_R/\Delta x = \lambda_R/\Delta y = 10$ and $\lambda_R/\Delta z = 2.5$ and using the Fourier points $N_y = 128$ and number of expansion cycles $N_x = 10$. For damping ratio less than 2 percent, larger values for $\lambda_R/\Delta x$, $\lambda_R/\Delta y$, $\lambda_R/\Delta z$, N_y, N_x, are suggested.

(3) The half space solution will result in accurate surface displacements by putting the viscous boundary at a depth of two wavelengths.

An investigation of the effects of the lateral boundary on the measured deflections in the Dynaflect, the Falling Weight Deflectometer (FWD) , and the Spectral-Analysis-of-Surface Waves (SASW) tests was conducted on three typical in-service pavement sections. They are road FM137, in Paris, Texas; Interstate Highway 10, in El Paso, Texas; and Route 1 in Austin, Texas. The conclusions from the studies of three test sites are:

(1) In the Dynaflect simulation, the results indicate that the effects of the lateral boundary on the measured deflections are directly related to: a) the loading position with respect to the edge of pavement; b) the thickness of the surface layer; c) the lateral stiffness contrast between the road and the surrounding soil; d) the height of the ramp, if the test is performed on a ramp. A closer loading position, a larger value of the thickness, a higher contrast, and a larger value of the ramp height will result in a larger influence of the lateral boundary.

(2) The lateral boundary has differential influence on different stations which will, in turn, change the shape of the deflection basins. This differential influence becomes more pronounced when the loading is closer to the edge.

(3) The errors induced by neglecting the lateral boundary are below 5 percent on the test site of FM 137. Significant errors may occur, however, on Interstate Highway 10. At the loading position of d = 1 ft, the errors are between 50 to 70 percent for various stations. Beyond d = 8 ft, the errors are within 5 percent.

(4) The existence of the retaining walls is important on the measured deflections, especially for the "high" ramp. For example, differences of around 20 percent can still occur at the outer station even when the load is located at 12 ft from the edge.

(5) Similar trends were found in the FWD test simulations.

(6) For these particular sites, dynamic effects seem to be more important in the FWD tests than in the Dynaflect tests. The basins of the FWD exhibit larger values than those of the Dynaflect.

(7) The results of the SASW tests indicate that in general the dispersion curve can be used to estimate the shear wave velocity profile. However, some fluctuations may occur in the dispersion curve because of the reflected body waves due to the abrupt change in the stiffness at the horizontal interfaces between layers. The existence of the lateral boundary can cause more fluctuations. This effect will be more pronounced for "long" wavelengths.

The effects of the lateral boundary on the measured deflections have been studied here through analytical simulations. Correlation of these results with actual measurements is necessary. The use of the UTPVT program validated with extensive field data can lead to a more rational interpretation of nondestructive test data and better structural evaluation of pavement in engineering practice. Finally, the soil-pavement formulation developed in this study can be applied to many other problems with 2 dimensional geometry but 3 dimensional loading, such as tunnel detection, material characterization of dams, etc.

Appendix A Formulation of Finite Elements

A.1 General Formulation

In general, a valid solution in solid mechanics has to satisfy three basic conditions for every point in the body under consideration. These conditions are the stress-strain relations, the strain-displacement compatibility equations, and the stress equilibrium equations. Alternatively, the last condition can be met via the principle of virtual work (Zienkiewicz, 1977).

For an isotropic linear elastic medium, the stress-strain relations in a rectangular Cartesian coordinate system (x, y, z) are given by

$$\begin{aligned}
\sigma_x &= (\lambda+2G)\varepsilon_x + \lambda\varepsilon_y + \lambda\varepsilon_z \\
\sigma_y &= \lambda\varepsilon_x + (\lambda+2G)\varepsilon_y + \lambda\varepsilon_z \\
\sigma_z &= \lambda\varepsilon_x + \lambda\varepsilon_y + (\lambda+2G)\varepsilon_z \\
\tau_{xy} &= G\gamma_{xy} \\
\tau_{yz} &= G\gamma_{yz} \\
\tau_{zx} &= G\gamma_{zx}
\end{aligned} \tag{A.1}$$

in which

G and λ are the Lamé moduli;
σ_x, σ_y, σ_z are normal stresses;
τ_{xy}, τ_{yz}, τ_{zx} are shear stresses;
ε_x, ε_y, ε_z are normal strains; and
γ_{xy}, γ_{yz}, γ_{zx} are shear strains.

The compatibility conditions for small strain theory can be defined as

$$\varepsilon_x = \frac{\partial u}{\partial x} \qquad \gamma_{xy} = \frac{\partial u}{\partial y} + \frac{\partial v}{\partial x}$$

$$\varepsilon_y = \frac{\partial v}{\partial y} \qquad \gamma_{yz} = \frac{\partial v}{\partial z} + \frac{\partial w}{\partial y} \tag{A.2}$$

$$\varepsilon_z = \frac{\partial w}{\partial z} \qquad \gamma_{zx} = \frac{\partial w}{\partial x} + \frac{\partial u}{\partial z}$$

where u, v, w are the displacements in the x-, y-, and z-directions, respectively. In matrix notation, Eqs. (A.1) and (A.2) can be symbolized as

$$\sigma = \boldsymbol{D}\ \varepsilon \tag{A.3}$$

$$\varepsilon = \boldsymbol{g}\ \boldsymbol{u} \tag{A.4}$$

where

$$\sigma = \begin{Bmatrix} \sigma_x \\ \sigma_y \\ \sigma_z \\ \tau_{xy} \\ \tau_{yz} \\ \tau_{zx} \end{Bmatrix} \tag{A.5}$$

$$\varepsilon = \begin{Bmatrix} \varepsilon_x \\ \varepsilon_y \\ \varepsilon_z \\ \gamma_{xy} \\ \gamma_{yz} \\ \gamma_{zx} \end{Bmatrix} \tag{A.6}$$

$$\boldsymbol{u} = \begin{Bmatrix} u \\ v \\ w \end{Bmatrix} \tag{A.7}$$

$$\boldsymbol{D} = \begin{bmatrix} \lambda+2G & \lambda & \lambda & 0 & 0 & 0 \\ \lambda & \lambda+2G & \lambda & 0 & 0 & 0 \\ \lambda & \lambda & \lambda+2G & 0 & 0 & 0 \\ 0 & 0 & 0 & G & 0 & 0 \\ 0 & 0 & 0 & 0 & G & 0 \\ 0 & 0 & 0 & 0 & 0 & G \end{bmatrix} \tag{A.8}$$

$$\boldsymbol{g} = \begin{bmatrix} \frac{\partial}{\partial x} & 0 & 0 \\ 0 & \frac{\partial}{\partial y} & 0 \\ 0 & 0 & \frac{\partial}{\partial z} \\ \frac{\partial}{\partial y} & \frac{\partial}{\partial x} & 0 \\ 0 & \frac{\partial}{\partial z} & \frac{\partial}{\partial y} \\ \frac{\partial}{\partial z} & 0 & \frac{\partial}{\partial x} \end{bmatrix} \tag{A.9}$$

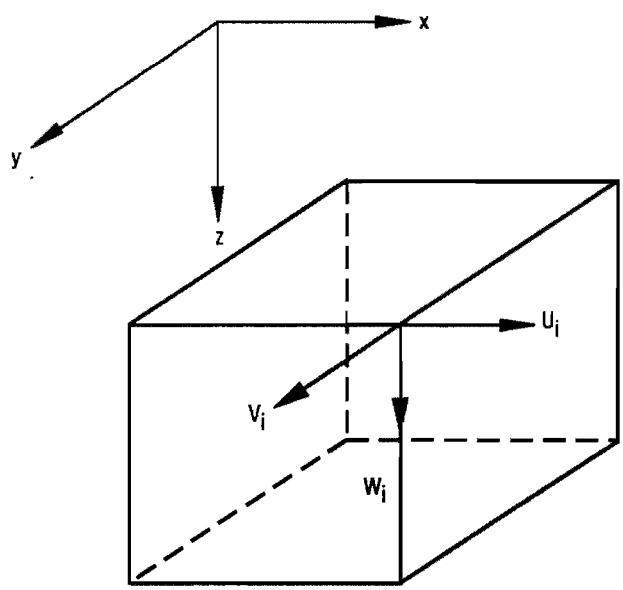

Figure A.1 A general three-dimensional finite element

For a general formulation of the displacement-based finite element method, consider a general three-dimensional finite element with n nodes (Figure A.1). Each node has three degrees of freedom: U_i, V_i, and W_i. Assuming the displacement shape functions, the relationships betweengeneric displacements and nodal displacements can be written as follows

$$\begin{aligned} u &= \sum_i^n f_i U_i \\ v &= \sum_i^n f_i V_i \\ w &= \sum_i^n f_i W_i \end{aligned} \tag{A.10}$$

where f_i is the shape function for node i.

In matrix notation, it can be written as

$$\boldsymbol{u} = \boldsymbol{N}\ \boldsymbol{U} \tag{A.11}$$

where matrix $\boldsymbol{N}$ contains the shape functions with dimension (3x3n) and vector $\boldsymbol{U}$ includes nodal displacements in the element. Substitution of Eq. (A.11) into Eq. (A.4) yields:

$$\varepsilon = \boldsymbol{B}\ \boldsymbol{U} \tag{A.12}$$

where matrix $\boldsymbol{B}$ is obtained by differentiation of the shape functions with respect to spatial variables. Substitution of Eq. (A.12) into Eq. (A.3) produces:

$$\sigma = \boldsymbol{D}\ \boldsymbol{B}\ \boldsymbol{U} \tag{A.13}$$

In this equation the matrix product $\boldsymbol{DB}$ gives stresses at any point due to unit values of nodal displacements.

Assume that small virtual displacements $\delta \boldsymbol{U}$ occur at the nodes. The resulting virtual generic displacements become

$$\delta \boldsymbol{u} = \boldsymbol{N}\ \delta \boldsymbol{U} \tag{A.14}$$

The virtual strains are

$$\delta \varepsilon = \boldsymbol{B}\ \delta \boldsymbol{U} \tag{A.15}$$

The virtual strain energy δU can be written as:

$$\delta U = \int_v \delta \varepsilon^T \sigma \; dv \tag{A.16}$$

where the superscript "T" denotes the transpose operation of a matrix or a vector, and the volume integral is performed over the entire element. The external virtual work done by the nodal forces $\boldsymbol{P}$ and body forces $\boldsymbol{b}$ can be defined as

$$\delta W = \delta \boldsymbol{U}^T \boldsymbol{P} + \int_v \delta \boldsymbol{u}^T \boldsymbol{b} \; dv \tag{A.17}$$

By applying the principle of virtual work, that is, $\delta U = \delta W$

$$\int_v \delta \varepsilon^T \sigma \; dv = \delta \boldsymbol{U}^T \boldsymbol{P} + \int_v \delta \boldsymbol{u}^T \boldsymbol{b} \; dv \tag{A.18}$$

Then, we can substitute Eq. (A.13) and use the transposes of Eqs. (A.14) and (A.15) to obtain

$$\delta \boldsymbol{U}^T \left(\int_v \boldsymbol{B}^T \boldsymbol{D} \boldsymbol{B} \; dv \right) \boldsymbol{U} = \delta \boldsymbol{U}^T \boldsymbol{P} + \delta \boldsymbol{U}^T \int_v \boldsymbol{N}^T \boldsymbol{b} \; dv \tag{A.19}$$

and

$$\left(\int_v \boldsymbol{B}^T \boldsymbol{D} \, \boldsymbol{B} \; dv \right) \boldsymbol{U} = \boldsymbol{P} + \int_v \boldsymbol{N}^T \boldsymbol{b} \; dv \tag{A.20}$$

Assume that the only contribution of the body force is from the inertial force. Using d'Alembert's principle, we can write

$$\boldsymbol{b} = -\rho \ddot{\boldsymbol{u}} \tag{A.21}$$

in which ρ is the mass density and $\ddot{\boldsymbol{u}}$ are the generic accelerations. Substitution of Eq. (A.11) into Eq. (A.21) produces

$$\boldsymbol{b} = -\rho \boldsymbol{N} \ddot{\boldsymbol{U}} \tag{A.22}$$

Now, by substituting Eq. (A.22) into Eq. (A.20), we have

$$\left(\int_v \boldsymbol{B}^T \boldsymbol{D}\, \boldsymbol{B}\ dv\right)\boldsymbol{U} = \boldsymbol{P} - \left(\int_v \rho\, \boldsymbol{N}^T \boldsymbol{N}\ dv\right)\ddot{\boldsymbol{U}} \tag{A.23}$$

Passing the second term of the right hand side to the left, we have

$$\boldsymbol{M}\,\ddot{\boldsymbol{U}} + \boldsymbol{K}\,\boldsymbol{U} = \boldsymbol{P} \tag{A.24}$$

where

$$\boldsymbol{K} = \int_v \boldsymbol{B}^T \boldsymbol{D}\, \boldsymbol{B}\ dv \tag{A.25}$$

and

$$\boldsymbol{M} = \int_v \rho\, \boldsymbol{N}^T \boldsymbol{N}\ dv \tag{A.26}$$

Matrix $\boldsymbol{K}$ in Eq. (A.25) is the static stiffness matrix for the element and matrix $\boldsymbol{M}$ in Eq. (A.26) is the mass matrix.

For a steady-state excitation, the nodal forces can be expressed as

$$\boldsymbol{P} = \overline{\boldsymbol{P}}\ e^{i\omega t} \tag{A.27}$$

Similarly, the nodal displacements can be written as

$$\boldsymbol{U} = \overline{\boldsymbol{U}}\ e^{i\omega t} \tag{A.28}$$

Therefore, the nodal accelerations can be obtained by differentiation of Eq. (A.28) twice, that is

$$\ddot{\boldsymbol{U}} = -\omega^2\, \overline{\boldsymbol{U}}\ e^{i\omega t} \tag{A.29}$$

Next, by substituting Eqs. (A.27), (A.28), and (A.29) into Eq.(A.24) and dropping the term $e^{i\omega t}$ from both sides, we have

$$\overline{\boldsymbol{s}}\ \overline{\boldsymbol{U}} = \overline{\boldsymbol{P}} \tag{A.30}$$

where

$$\overline{\boldsymbol{S}} = \boldsymbol{K} - \omega^2 \boldsymbol{M} \tag{A.31}$$

Matrix $\overline{\boldsymbol{S}}$ in Eq. (A.31) is called the dynamic stiffness matrix of the element.

Conceptually, the integrals in Eqs. (A.25) and (A.26) can be obtained by integrating explicitly over the entire volume. For some cases, however, it is necessary to use a numerical integration technique. An accurate and convenient method for integration is Gaussian quadrature. Generally this method requires transforming the spatial variables (x, y, z) in the Cartesian coordinate system to a natural coordinate system (ξ, η, ζ) which has its origin at the center of the range of integration. The integral is then replaced by summation of the integrand computed at specific points and scaled by corresponding weighting factors. These specific points are called Gaussian quadrature points or integration points. For more details, the reader is referred to Weaver and Johnston (1984).

Thus, using Gaussian quadrature, Eq. (A.25) can be written as follows

$$\boldsymbol{K} = \int\int\int \boldsymbol{B}^T \boldsymbol{D}\, \boldsymbol{B}\ dx\, dy\, dz$$

$$= \int_{-1}^{1}\int_{-1}^{1}\int_{-1}^{1} \boldsymbol{B}^T \boldsymbol{D}\, \boldsymbol{B}\ |\mathbf{J}|\ d\xi\, d\eta\, d\zeta$$

Finally, we can write

$$\boldsymbol{K} = \sum_{i}^{n}\sum_{j}^{n}\sum_{k}^{n} R_i R_j R_k \left\{ \boldsymbol{B}^T \boldsymbol{D}\, \boldsymbol{B}\ |\mathbf{J}| \right\}_{i\,j\,k} \tag{A.31}$$

in which a set of indices (i, j, k) denotes one integration point; R_i, R_j, R_k are the weighting factors, as listed in Table A.1; $|\mathbf{J}|$ is the determinant of the Jacobian matrix, required for correct transformation of coordinates. Notice that the term $\{ \boldsymbol{B}\, \boldsymbol{D}\, \boldsymbol{B}\ |\mathbf{J}| \}$ is evaluated at each integration point. Likewise, Eq. (A.26) can be rewritten as

$$\boldsymbol{M} = \sum_{i}^{n}\sum_{j}^{n}\sum_{k}^{n} R_i R_j R_k \left\{ \rho \boldsymbol{N}^T \boldsymbol{N}\ |\mathbf{J}| \right\}_{i\,j\,k} \tag{A.32}$$

Table A.1 Coefficients for Gaussian quadrature (after Weaver and Johnston, 1984)

n	$\pm \xi, \eta, \zeta$	R
1	0.0	2.0
2	0.5773502692	1.0
3	0.7745966692	0.5555555556
	0.0	0.8888888889
4	0.8611363116	0.3478548451
	0.3399810436	0.6521451549
5	0.9061798459	0.2369268851
	0.5384693101	0.4786286705
	0.0	0.5688888889

In summary, for any finite element, the static stiffness matrix $\boldsymbol{K}$ and the mass matrix $\boldsymbol{M}$ can be obtained by selecting the proper shape functions, determining the integration points required, and performing the summations of Eqs. (A.31) and (A.32).

A.2 Finite Elements Used

Four types of finite elements have been used in the study. They are called "SOLID8", "SOLID12A", "SOLID12B", and "SOLID16". Since they are all rectangular solids with dimensions equal to Δx, Δy, Δz in the x, y, z directions, the Jacobian should be equal to the volume of the element. That is, $|\mathbf{J}|$ is a constant equal to the product of Δx, Δy, and Δz. For compact form, the shape functions are expressed in their natural coordinates (ξ, η, ζ).

In the following, the index i represents the nodal number; a set of (ξ_i, η_i, ζ_i) represents the coordinates of the nodal point; and a set of (ξ, η, ζ) denotes the coordinates of the integration point.

Element SOLID8

Figure A.2 shows a SOLID8 element with 8 nodes where linear shape functions are assumed in all directions. Two integration points are usedin each direction. The shape functions can be written as follows

For i = 1, 2, 3, 4, 5, 6, 7, 8

$$f_i = \frac{1}{8}(1+\xi\xi_i)(1+\eta\eta_i)(1+\zeta\zeta_i) \qquad \text{(A.33)}$$

in which the values of (ξ_i, η_i, ζ_i) are listed in Table A.2.

Element SOLID12A

Figure A.3 shows a SOLID12A element with 12 nodes where the shape functions are assumed to be linear in the y- and z-directions and quadratic in the x-direction. Two integration points are used in each direction. The shape functions can be written as follows

For i = 1, 2, 5, 6, 7, 8, 11, 12

$$f_i = \frac{1}{8} \xi (\xi+\xi_i) (1+\eta\eta_i) (1+\zeta\zeta_i) \tag{A.34}$$

For i = 3, 4, 9, 10

$$f_i = \frac{1}{4} (1-\xi^2) (1+\eta\eta_i) (1+\zeta\zeta_i) \tag{A.35}$$

in which the values of (ξ_i, η_i, ζ_i) are listed in Table A.3.

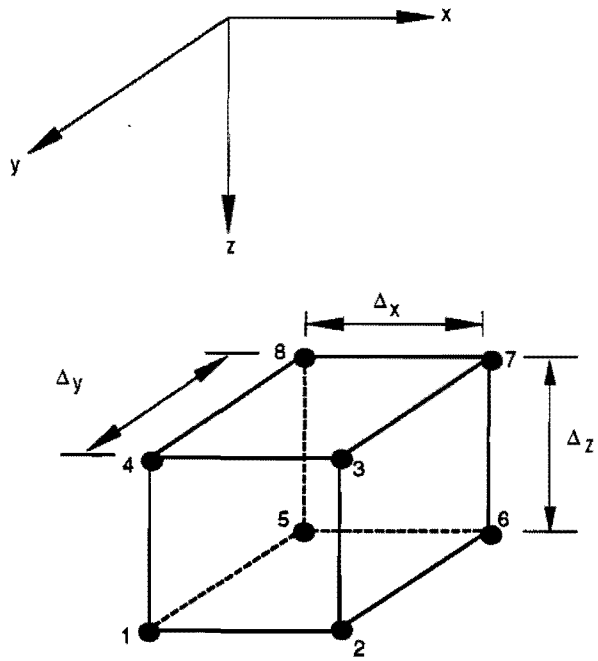

Figure A.2 Element SOLID8

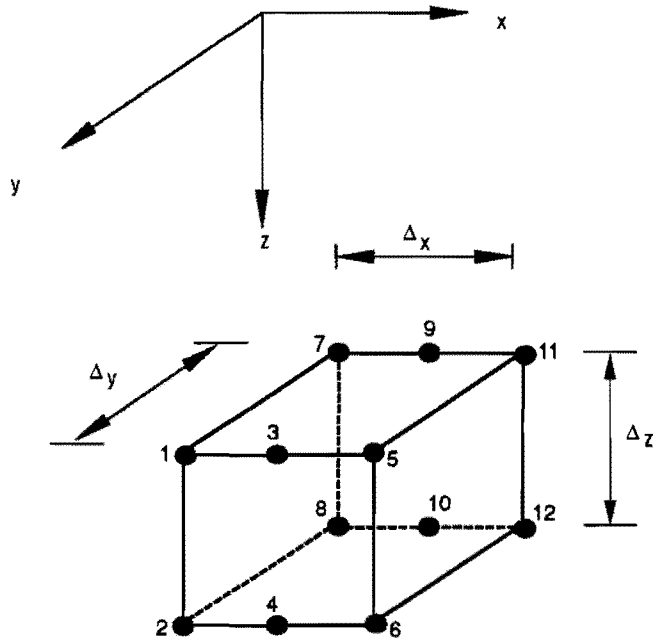

Figure A.3 Element SOLID12A

Table A.2 Nodal Coordinates for Element SOLID8

Nodal Point	ξ_i	η_i	ζ_i
1	-1	1	1
2	1	1	1
3	1	1	-1
4	-1	1	-1
5	-1	-1	1
6	1	-1	1
7	1	-1	-1
8	-1	-1	-1

Table A.3 Nodal Coordinates for Element SOLID12A

Nodal Point	ξ_i	η_i	ζ_i
1	-1	1	-1
2	-1	1	1
3	0	1	-1
4	0	1	1
5	1	1	-1
6	1	1	1
7	-1	-1	-1
8	-1	-1	1
9	0	-1	-1
10	0	-1	1
11	1	-1	-1
12	1	-1	1

Element SOLID12B

Figure A.4 shows a SOLID12B element with 12 nodes where the shape functions are assumed to be linear in the x- and y-directions and quadratic in the z-direction. Two integration points are used in each direction. The shape functions can be written as follows

For i = 1, 3, 4, 6, 7, 9, 10, 12

$$f_i = \frac{1}{8}(1+\xi\xi_i)(1+\eta\eta_i)\,\zeta\,(\zeta+\zeta_i) \tag{A.36}$$

For i = 2, 5, 8, 11

$$f_i = \frac{1}{4}(1+\xi\xi_i)(1+\eta\eta_i)(1-\zeta^2) \tag{A.37}$$

in which the values of (ξ_i, η_i, ζ_i) are listed in Table A.4.

Element SOLID16

Figure A.5 shows a SOLID16 element with 16 nodes where the shape functions are assumed to be linear in the y-direction and quadratic in the x-and z-directions Two integration points are used in each direction. The shape functions can be written as follows

For i = 1,3, 6, 8, 9, 11, 14, 16

$$\begin{aligned} f_i = {} & \frac{1}{8}(1+\xi\xi_i)(1+\eta\eta_i)(1+\zeta\zeta_i) \\ & - \frac{1}{8}(1+\xi\xi_i)(1+\eta\eta_i)(1-\zeta^2) \\ & - \frac{1}{8}(1-\xi^2)(1+\eta\eta_i)(1+\zeta\zeta_i) \end{aligned} \tag{A.38}$$

For i = 2, 7, 10, 15

$$f_i = \frac{1}{4}(1+\xi\xi_i)(1+\eta\eta_i)(1-\zeta^2) \tag{A.39}$$

For i = 4, 5, 12, 13

$$f_i = \frac{1}{4}(1-\xi^2)(1+\eta\eta_i)(1+\zeta\zeta_i) \tag{A.40}$$

in which the values of (ξ_i, η_i, ζ_i) are listed in Table A.5.

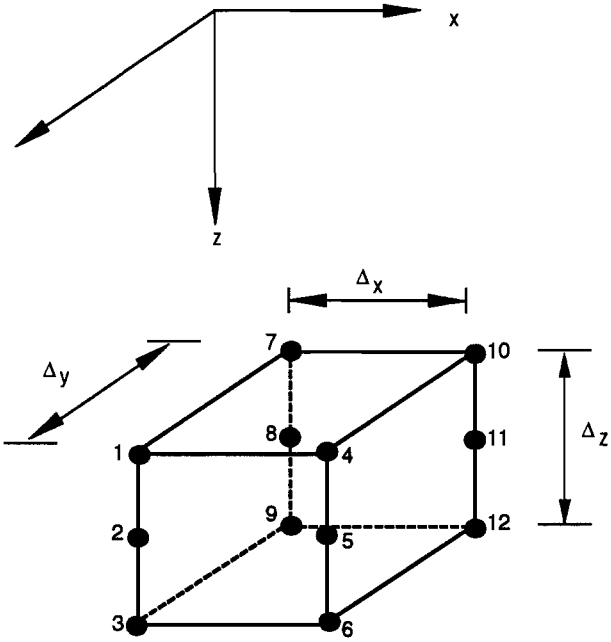

Figure A.4 Element SOLID12B

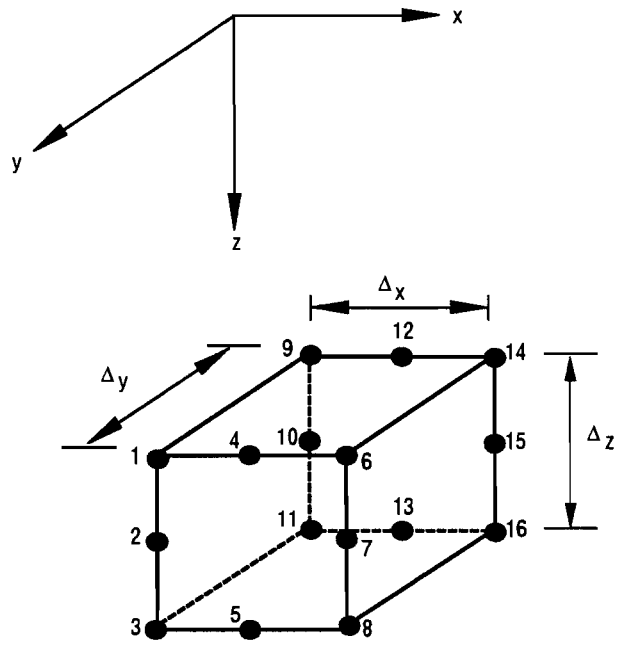

Figure A.5 Element SOLID16

Table A.4 Nodal Coordinates for Element SOLID12B

Nodal Point	ξ_i	η_i	ζ_i
1	-1	1	-1
2	-1	1	0
3	-1	1	1
4	1	1	-1
5	1	1	0
6	1	1	1
7	-1	-1	-1
8	-1	-1	0
9	-1	-1	1
10	1	-1	-1
11	1	-1	0
12	1	-1	1

Table A.5 Nodal Coordinates for Element SOLID16

Nodal Point	ξ_i	η_i	ζ_i
1	-1	1	-1
2	-1	1	0
3	-1	1	1
4	0	1	-1
5	0	1	1
6	1	1	-1
7	1	1	0
8	1	1	1
9	-1	-1	-1
10	-1	-1	0
11	-1	-1	1
12	0	-1	-1
13	0	-1	1
14	1	-1	-1
15	1	-1	0
16	1	-1	1

APPENDIX B TIME RECORDS OF THE FWD TESTS

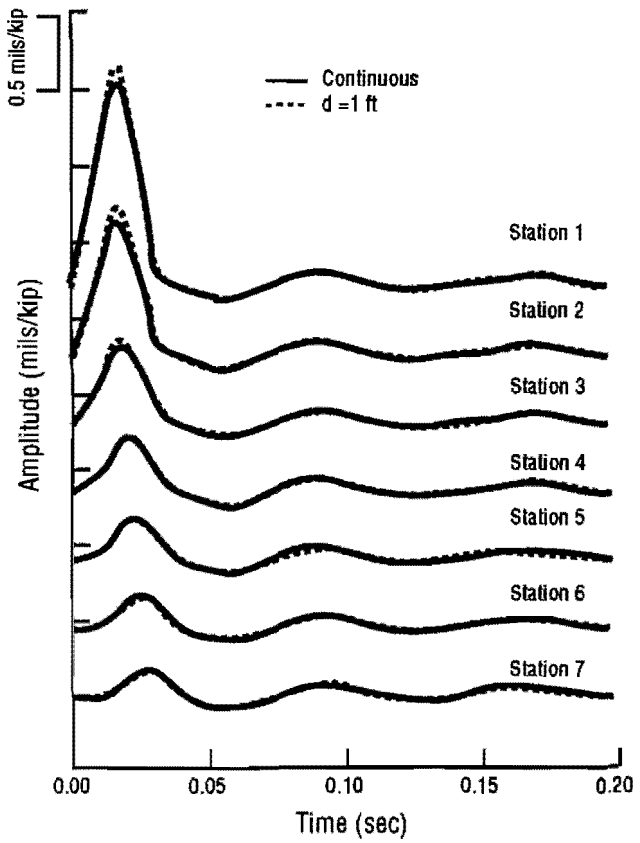

Figure B.1 FWD Time Histories for Seven Stations on Profile 1 with h = 15 ft and Loading Position d = 1 ft

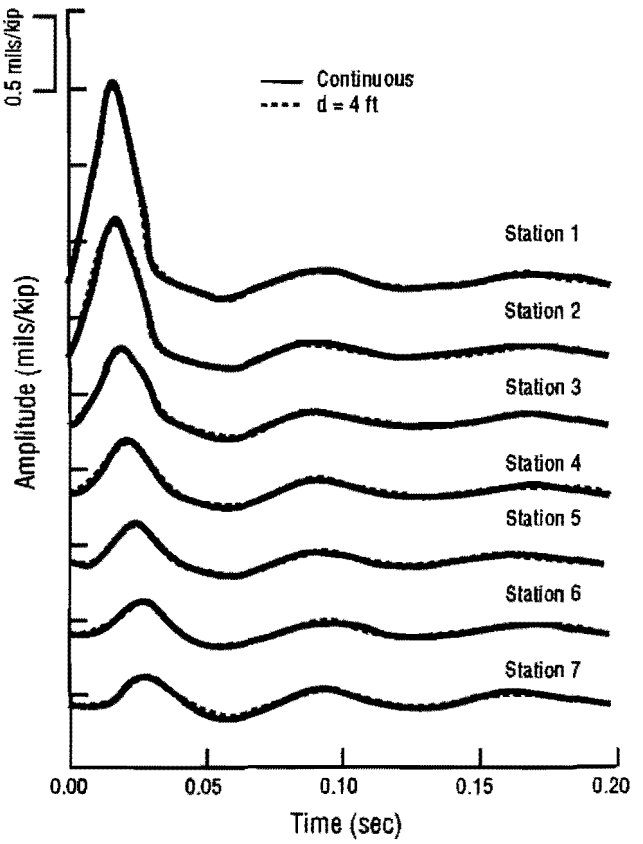

Figure B.2 FWD Time Histories for Seven Stations on Profile 1 with h = 15 ft and Loading Position d = 4 ft

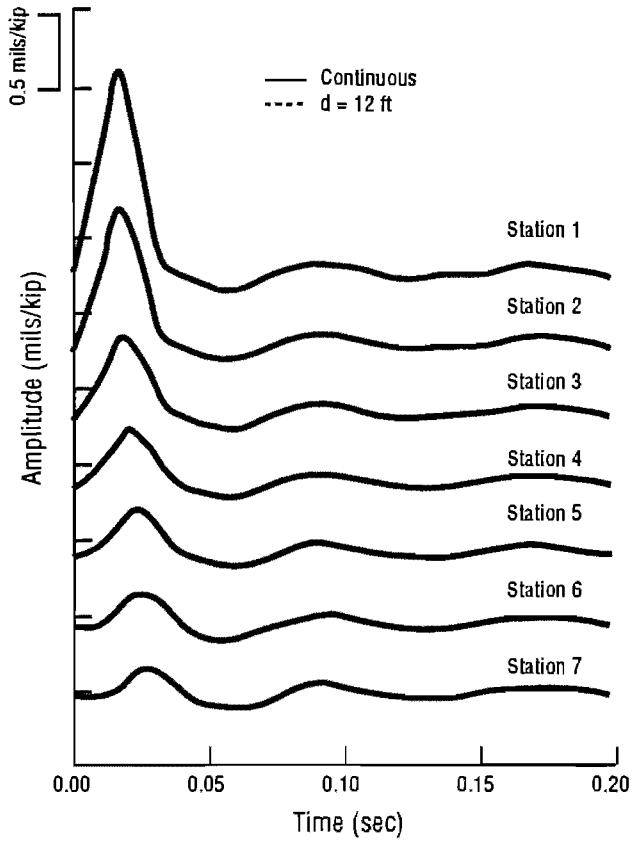

Figure B.3 FWD time histories forseven stations on Profile 1 with h = 15 ft and loading position d = 12 ft

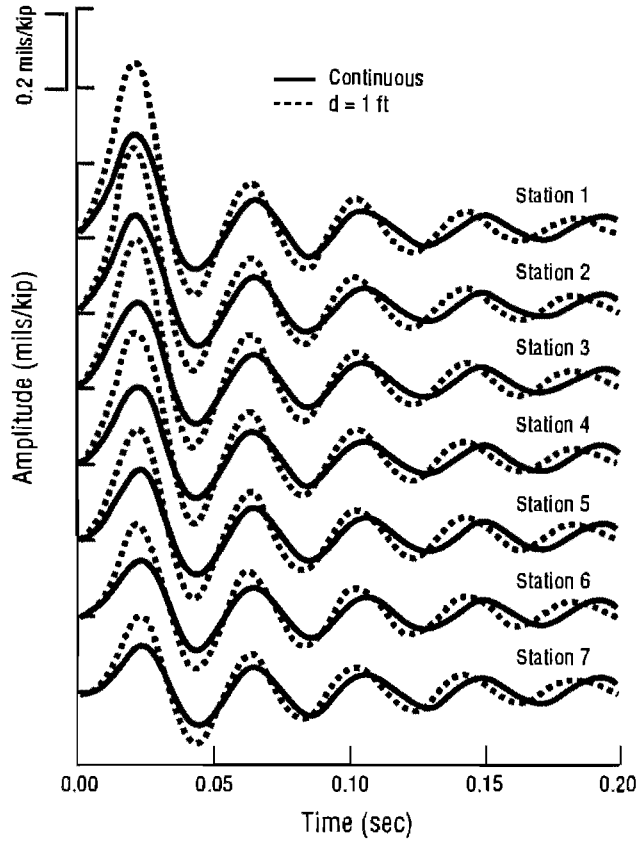

Figure B.4 FWD time histories for seven stations on Profile 2 with h = 15 ft and poading position d = 1 ft

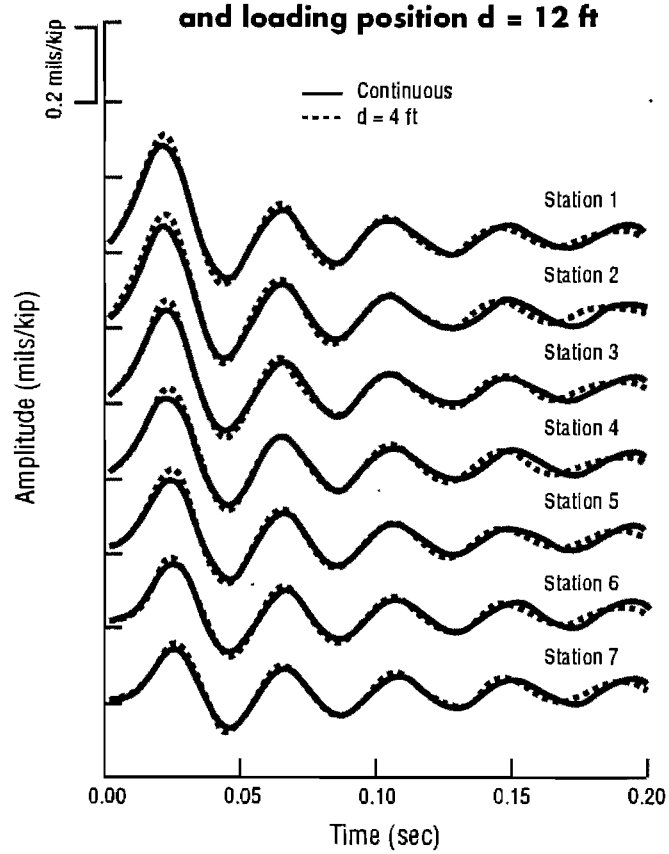

Figure B.5 FWD time histories for seven stations on Profile 2 with h = 15 ft and loading position d = 4 ft

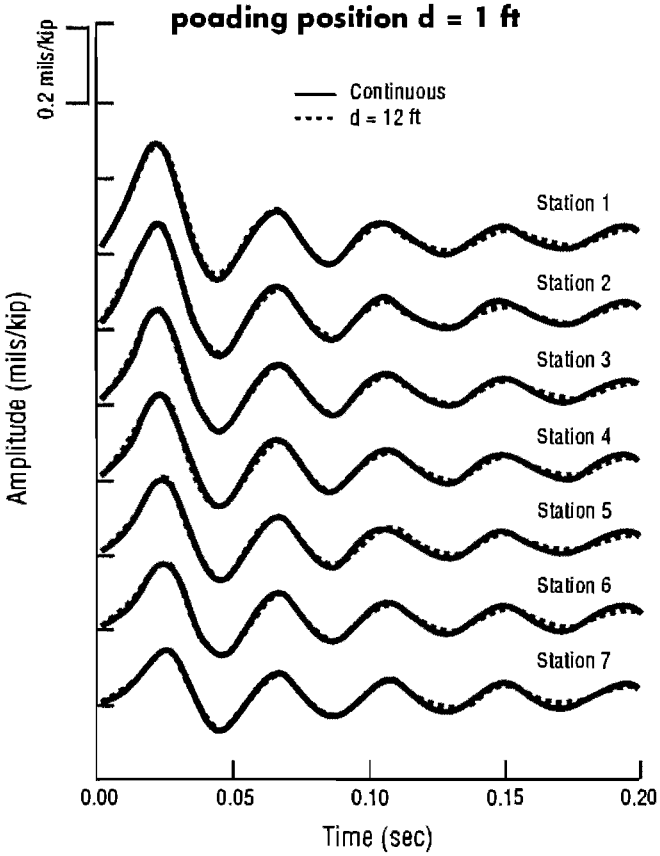

Figure B.6 FWD time histories for seven stations on Profile 2 with h = 15 ft and loading position d = 12 ft

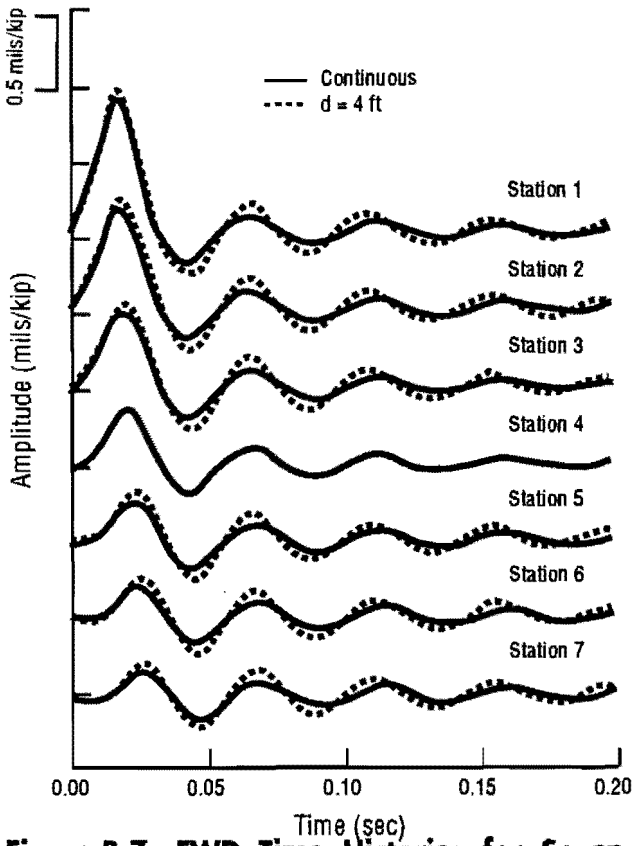

Figure B.7 FWD Time Histories for Seven Stations on Profile 3 with h = 15 ft and Loading Position d = 4 ft

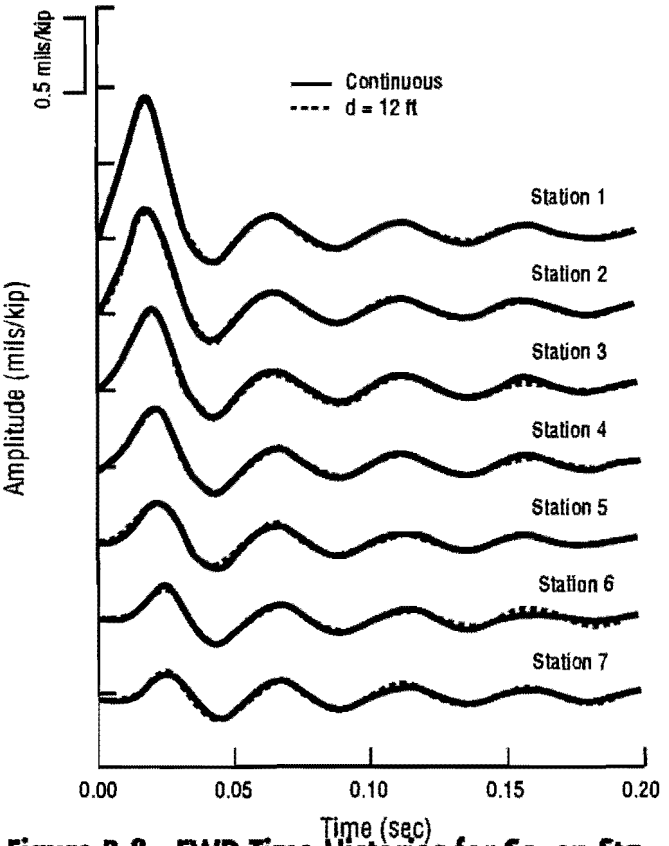

Figure B.8 FWD Time Histories for Seven Stations on Profile 3 with h = 15 ft and Loading Position d = 12 ft

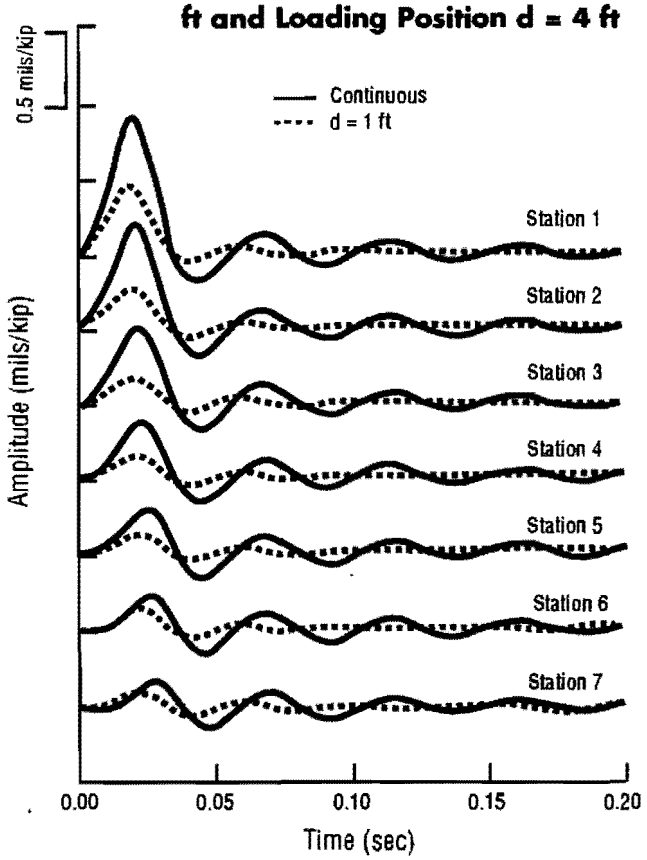

Figure B.9 FWD Time Histories for Seven Stations on Profile 4 with h = 15 ft and Loading Position d = 1 ft

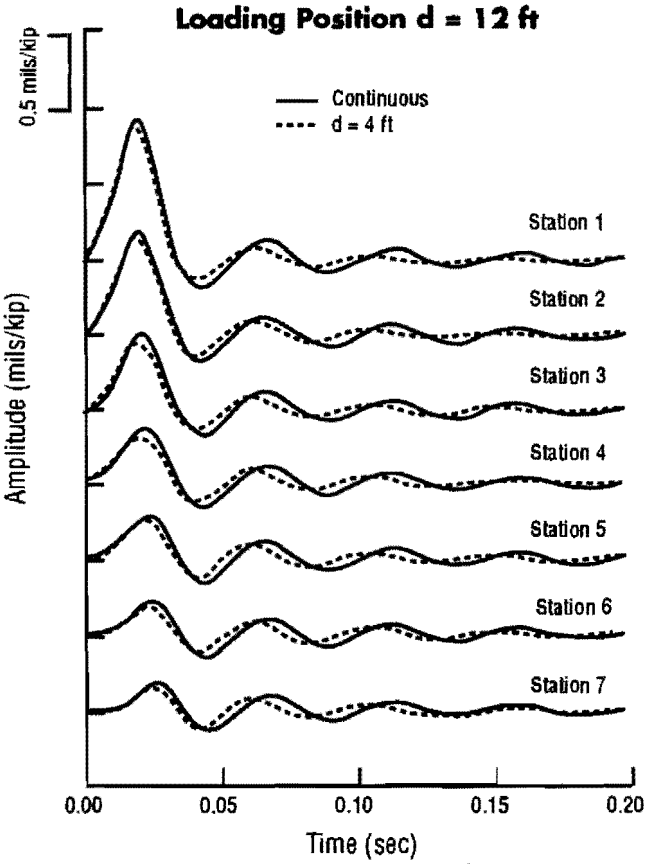

Figure B.10 FWD Time Histories for Seven Stations on Profile 4 with h = 15 ft and Loading Position d = 4 ft

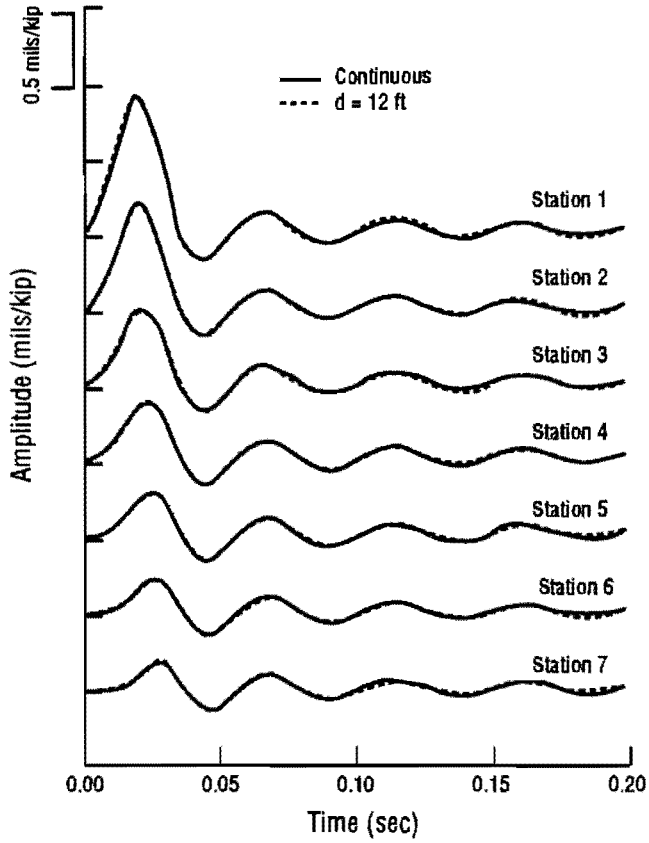

Figure B.11 FWD Time Histories for Seven Stations on Profile 4 with h = 15 ft and Loading Position d = 12 ft

APPENDIX C PHASE DIAGRAMS OF THE SASW TESTS

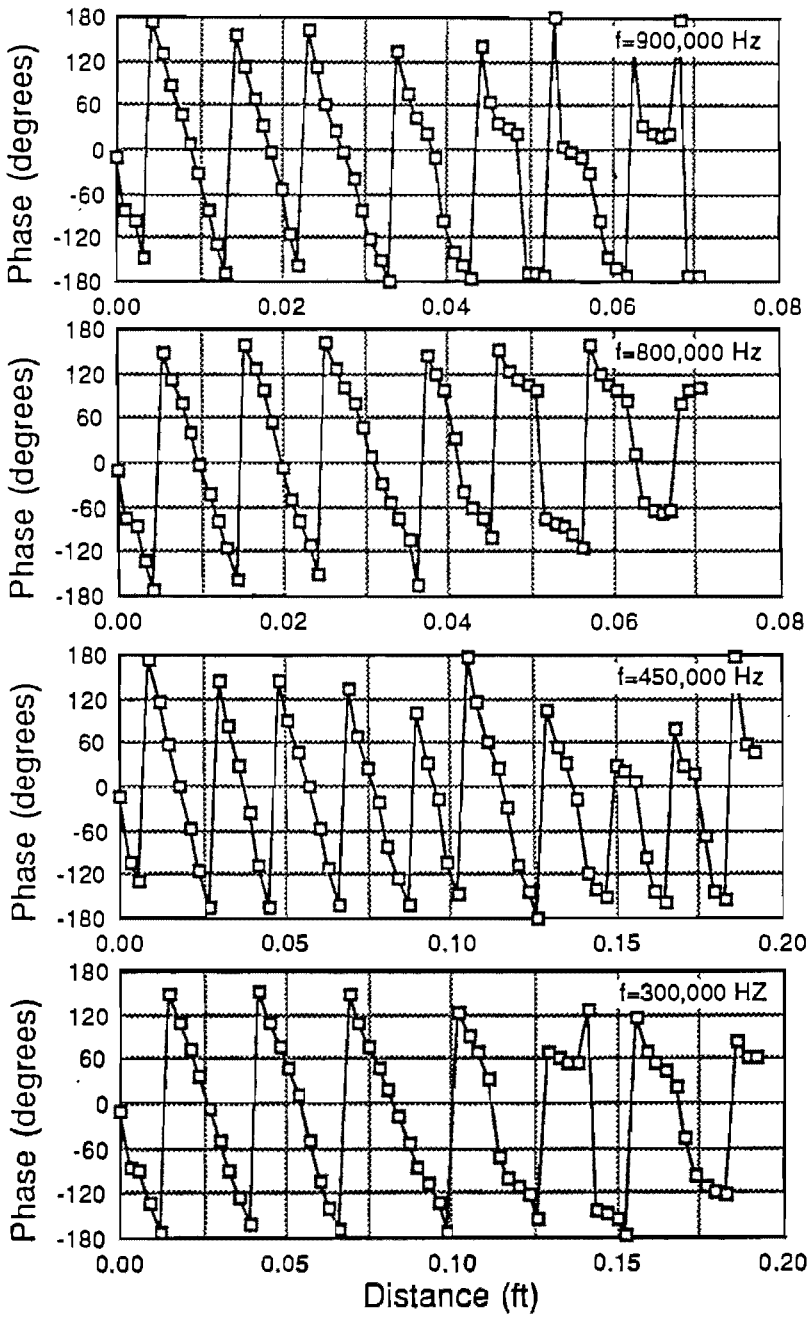

Figure C.1 Phase diagrams of frequencies f = 900,000 to 300,000 Hz for the continuous stratum of Profile 2

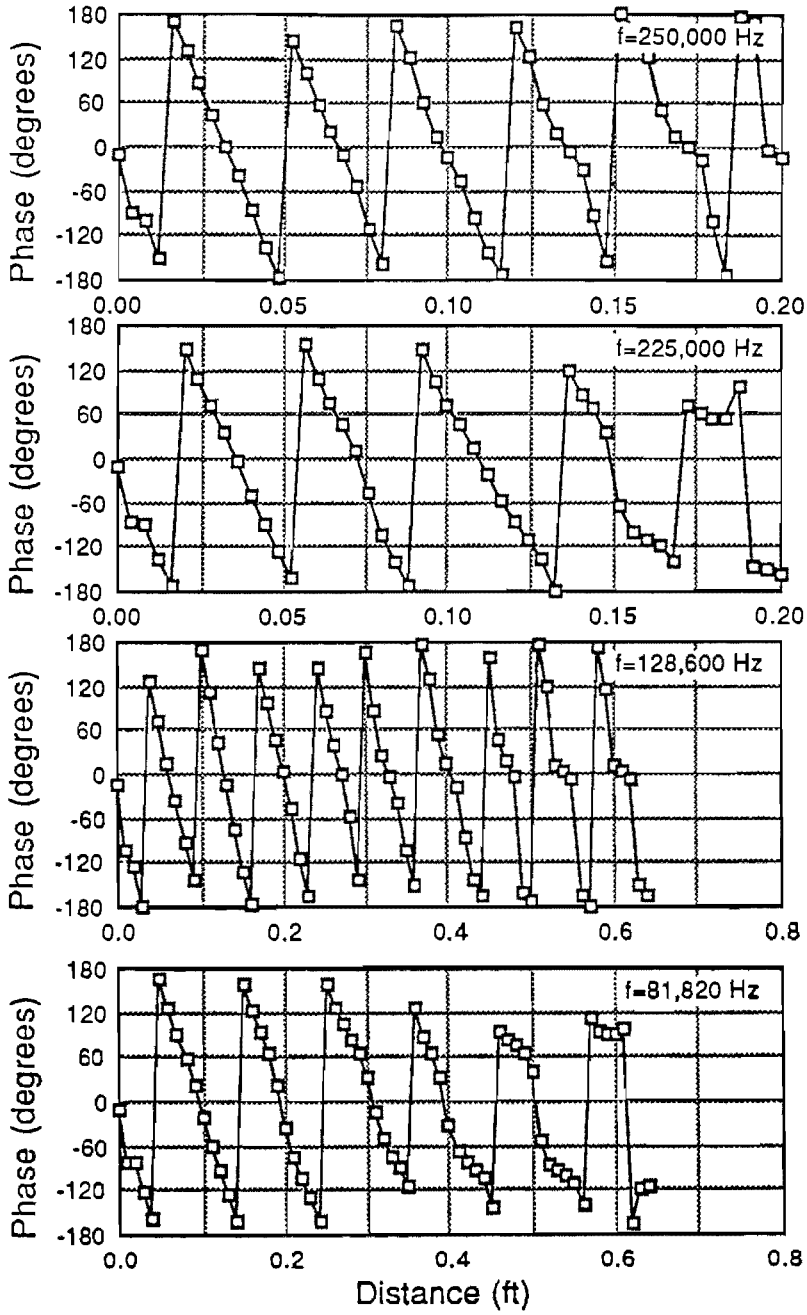

Figure C.2 Phase diagrams of frequencies f = 250,000 to 81,820 Hz for the continuous stratum of Profile 2

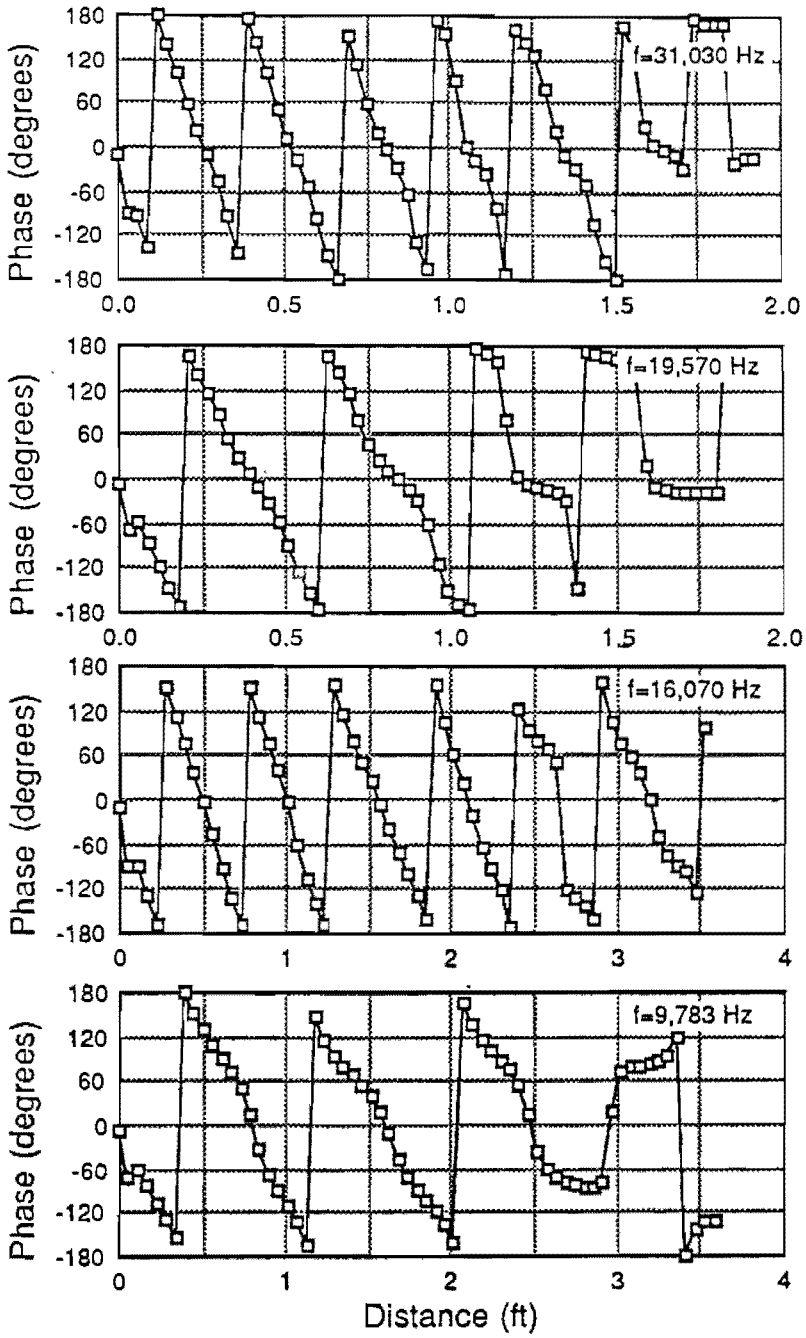

Figure C.3 Phase diagrams of frequencies f = 31,030 to 9,783 Hz for the continuous stratum of Profile 2

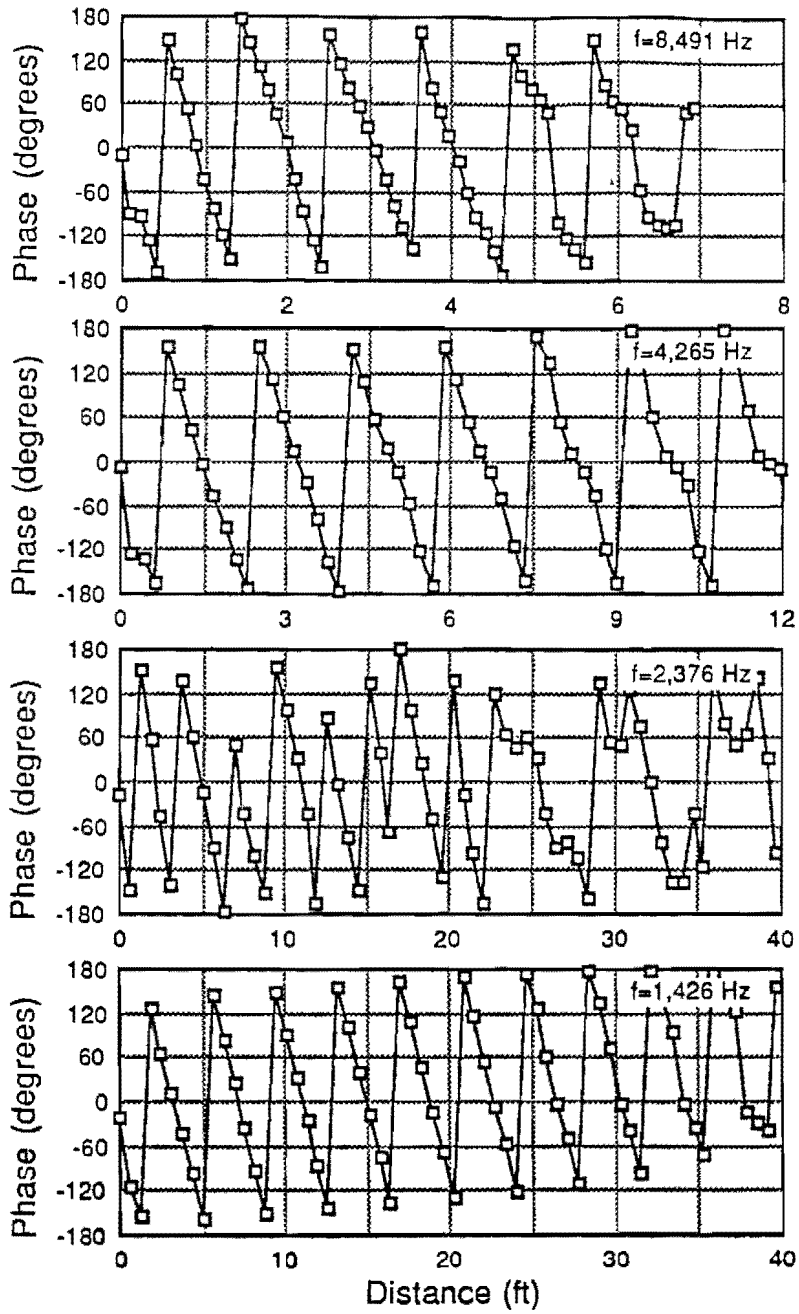

Figure C.4 Phase diagrams of frequencies f = 8,491 to 1,426 Hz for the continuous stratum of Profile 2

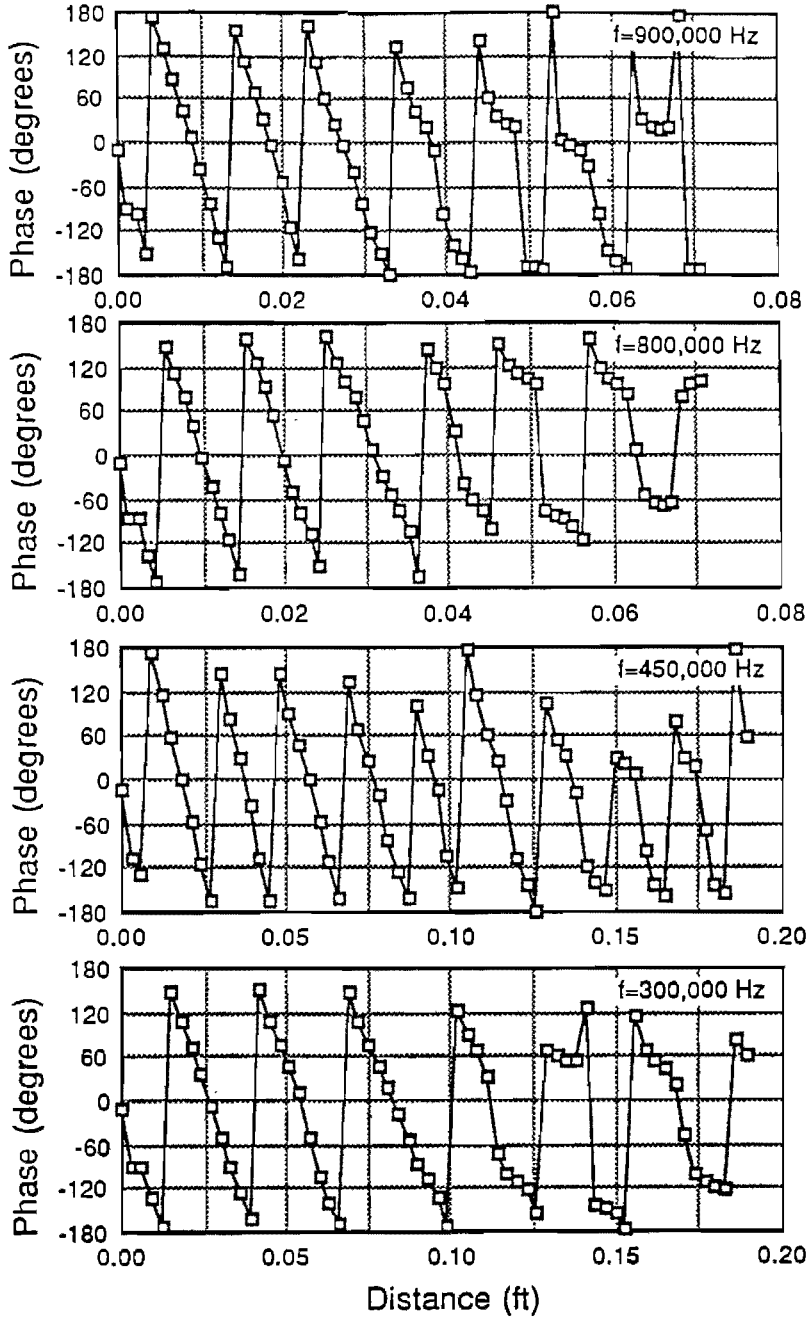

Figure C.5 Phase diagrams of frequencies f = 900,000 to 300,000 Hz for loading position d = 1 ft of Profile 2

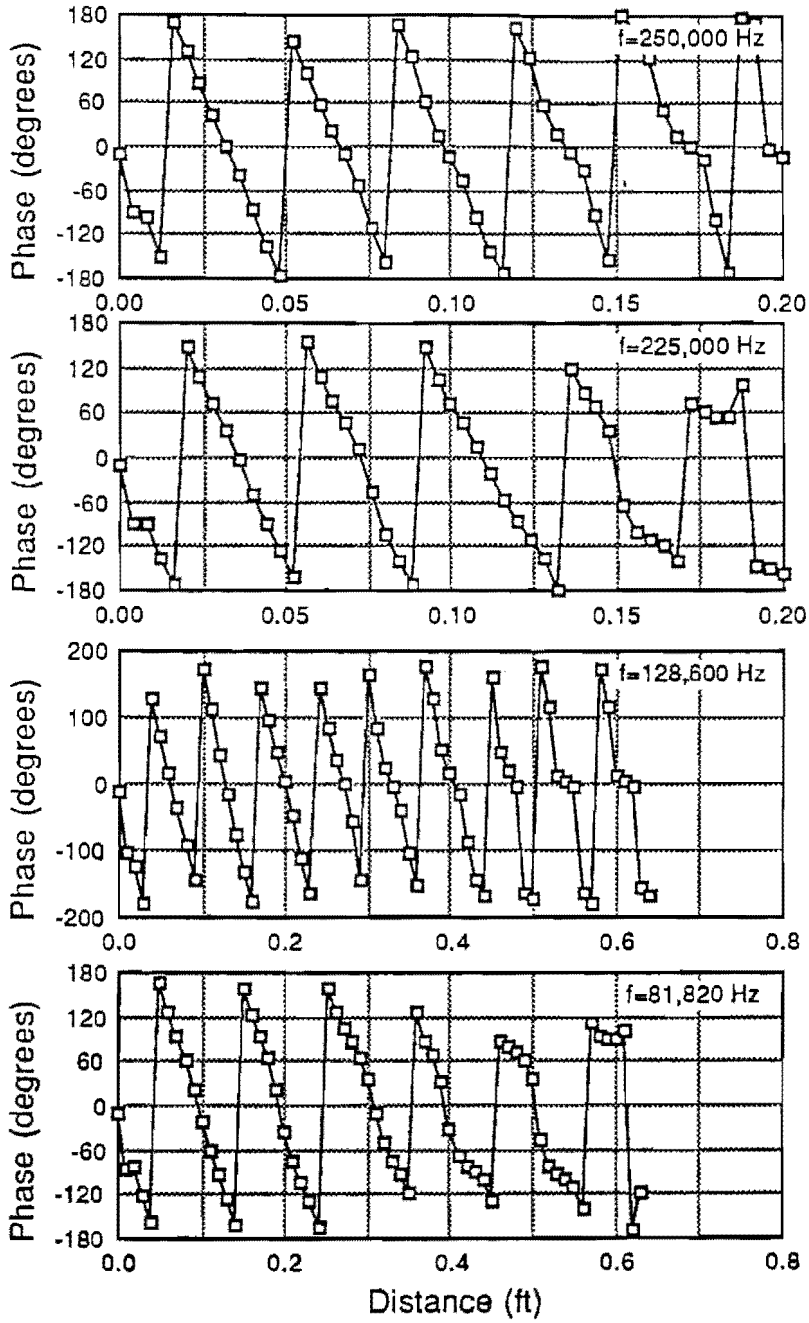

Figure C.6 Phase diagrams of frequencies f = 250,000 to 81,820 Hz for loading position d = 1 ft of Profile 2

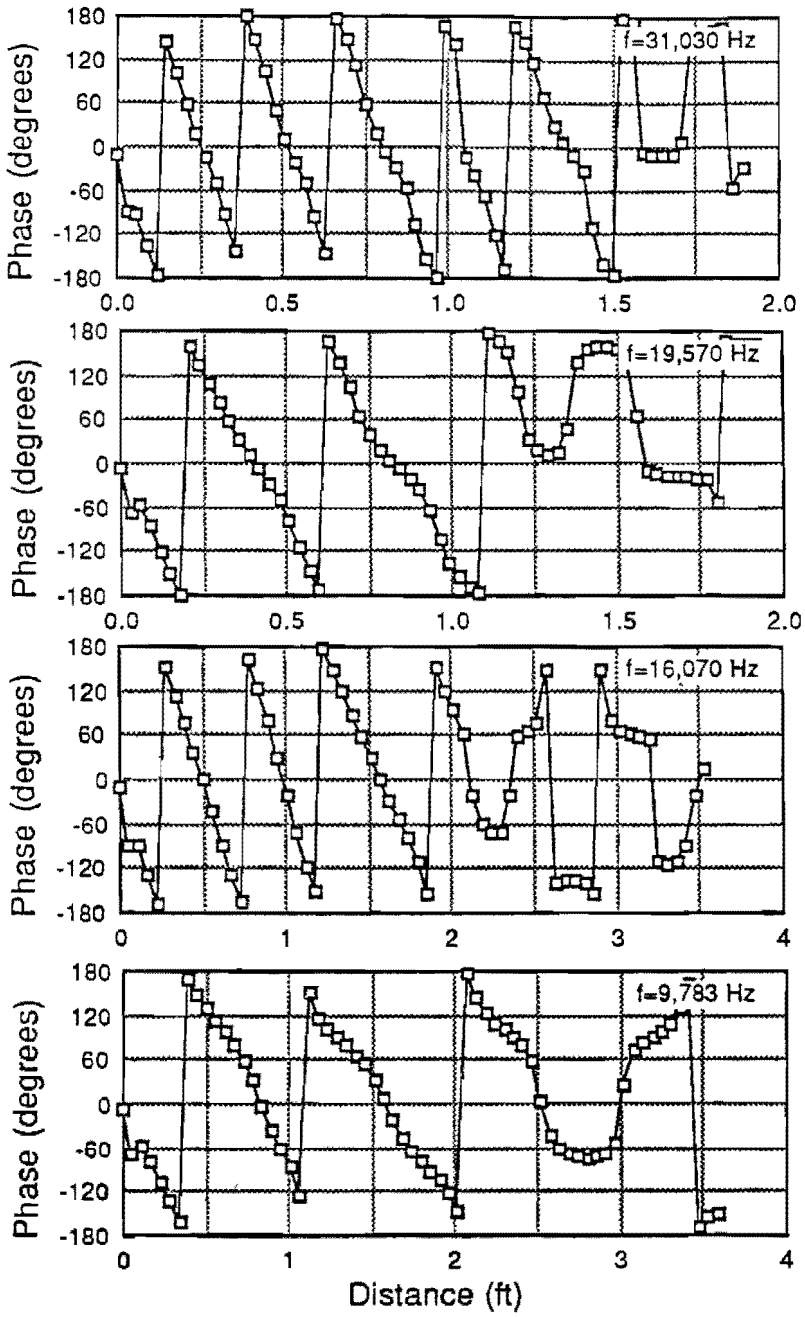

Figure C.7 Phase diagrams of frequencies f = 31,030 to 9,783 Hz for loading position d = 1 ft of Profile 2

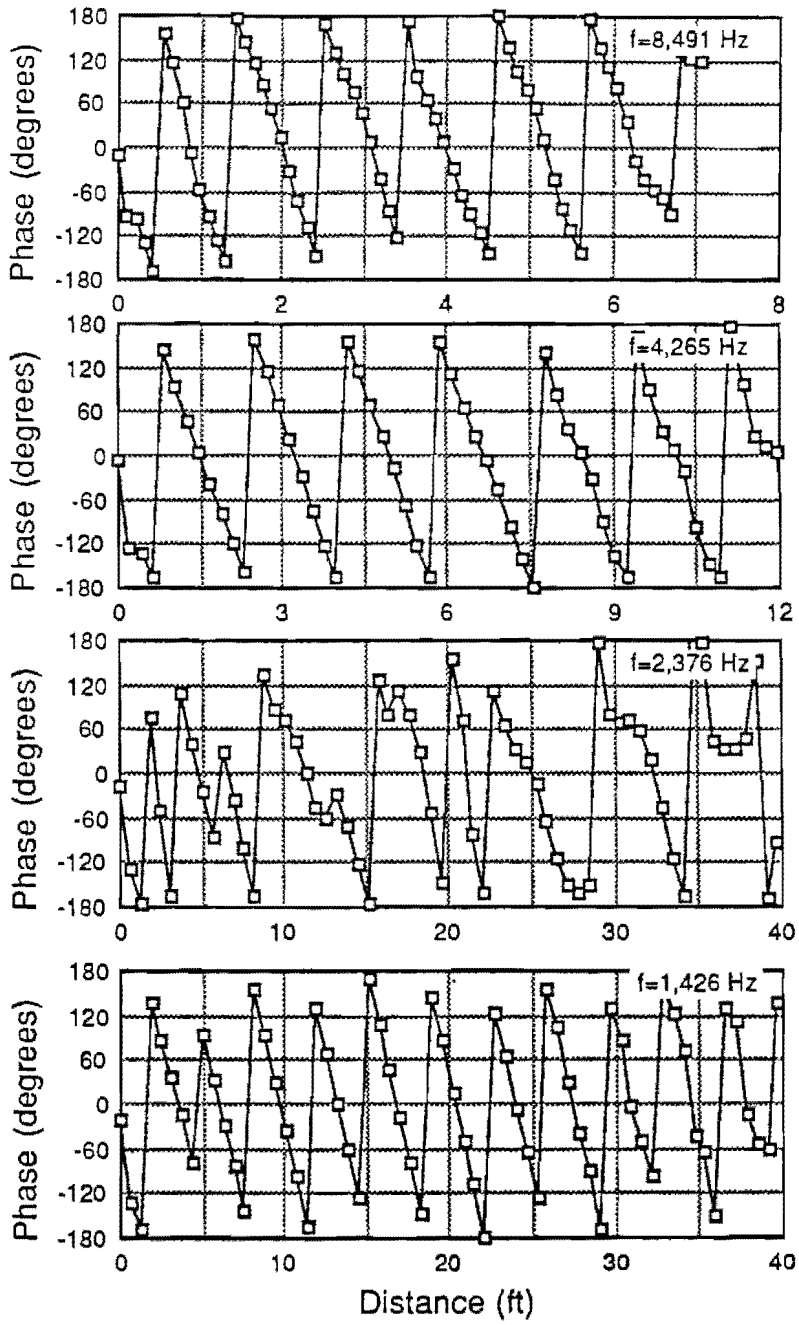

Figure C.8 Phase diagrams of frequencies f = 8,491 to 1,426 Hz for loading position d = 1 ft of Profile 2

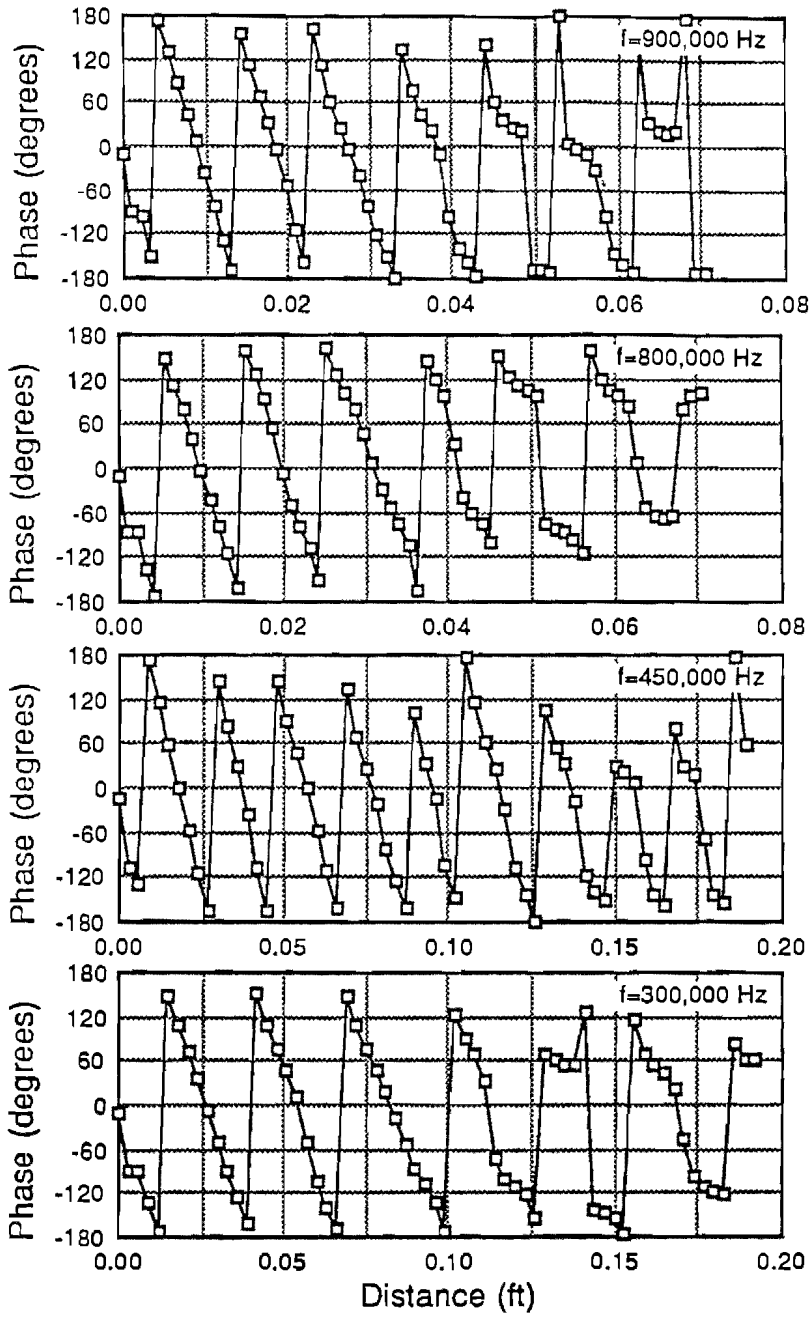

Figure C.9 Phase diagrams of frequencies f = 900,000 to 300,000 Hz for loading position d = 4 ft of Profile 2

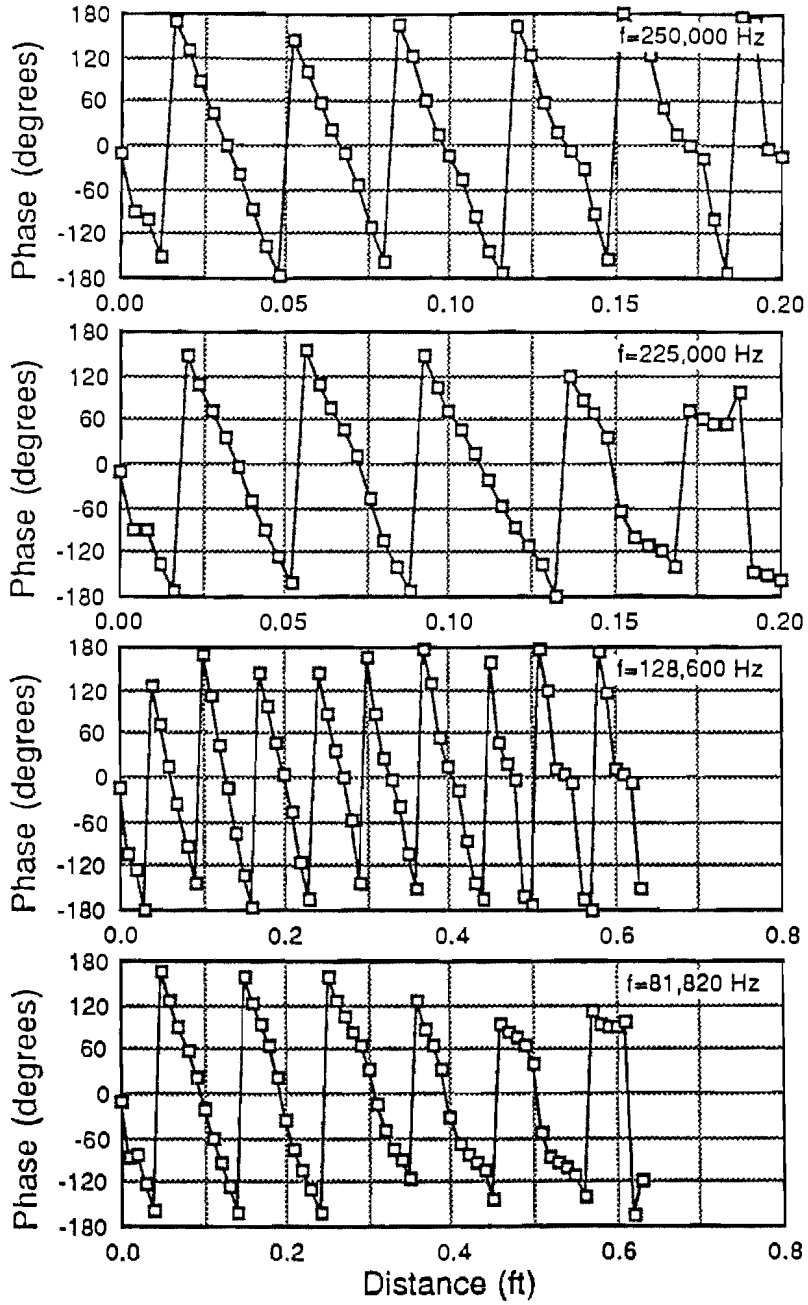

Figure C.10 **Phase diagrams of frequencies f = 250,000 to 81,820 Hz for loading position d = 4 ft of Profile 2**

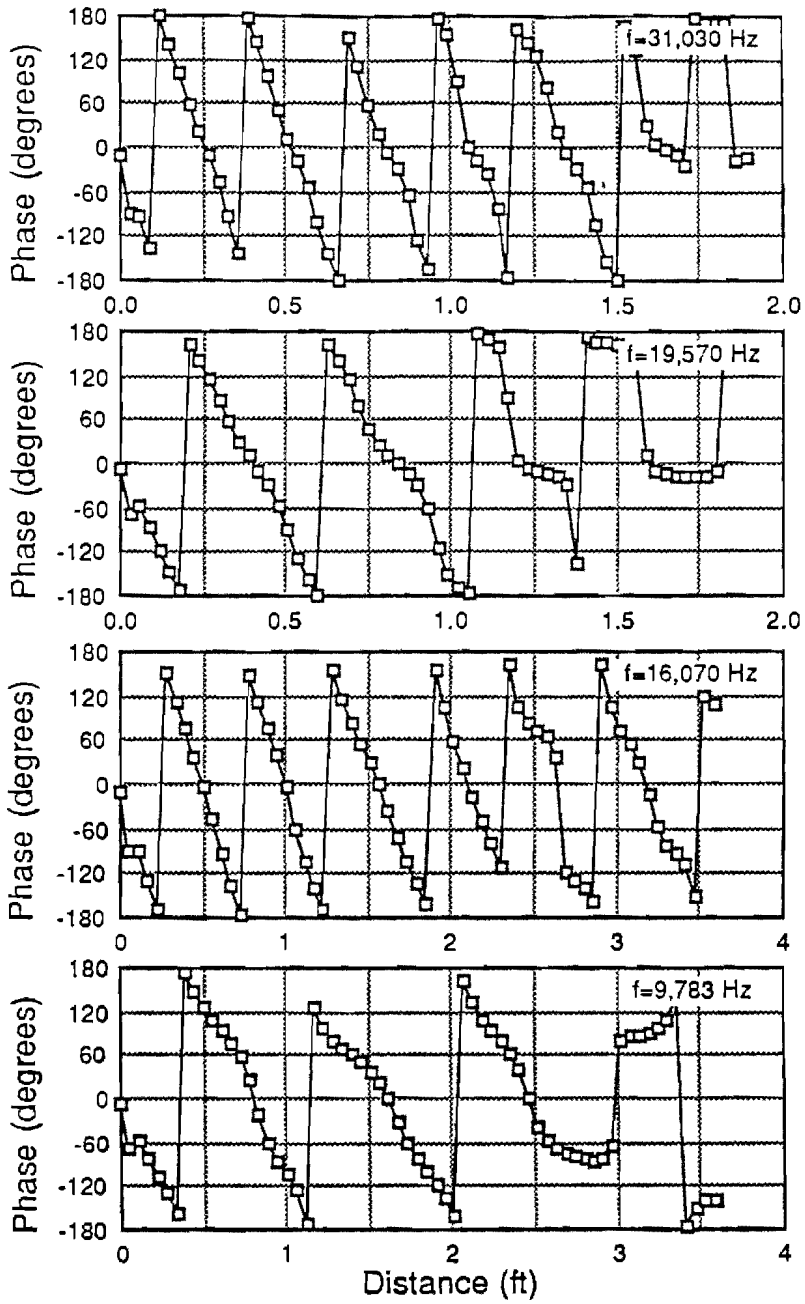

Figure C.11 Phase diagrams of frequencies f = 31,030 to 9,783 Hz for loading position d = 4 ft of Profile 2

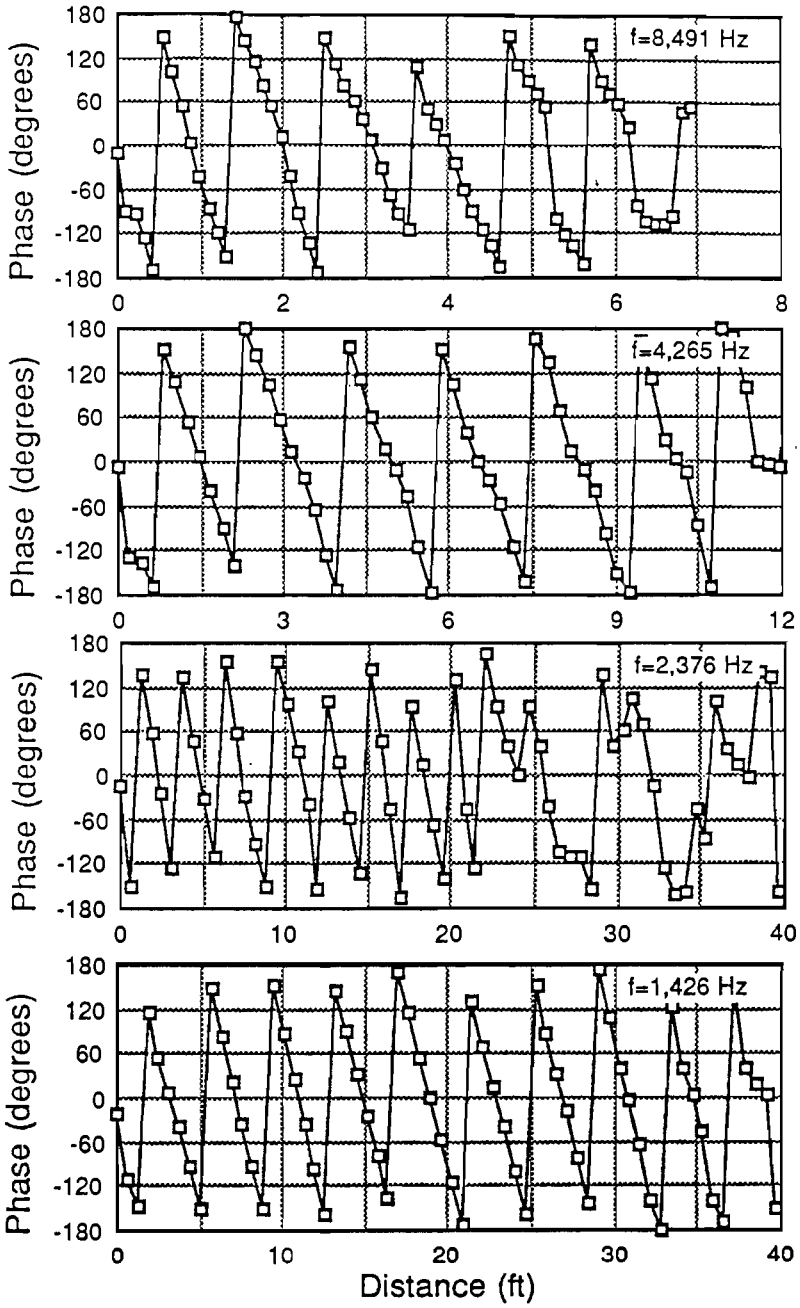

Figure C.12 **Phase diagrams of frequencies f = 8,491 to 1,426 Hz for loading position d = 4 ft of Profile 2**

BIBLIOGRAPHY

The Asphalt Institute, (1977), *Asphalt Overlays and Pavement Rehabilitation*, Manual Series No. 17 (MS-17), 118 pp.

Bracewell, R.N., (1965), *The Fourier Transform and Its Applications*, McGraw-Hill Book Company, New York, 474 pp.

Brigham, E.O., (1974), *The Fast Fourier Transform*, Prentice-Hall Inc., New Jersey, 252 pp.

Burmister, D.M., (1943), "The Theory of Stresses and Displacements in Layered Systems and Applications to the Design of Airport Runways," *Proceedings, Highway Research Board*, Vol. 23, pp. 126-48.

Cooley, J.W., and J.W. Tukey, (1965), "An Algorithm for Machine Calculation of Complex Fourier Series," *Math Computation*, Vol. 19., pp. 297-301.

Epps, J.A., and C.L. Monismith, (1986), "Equipment for Obtaining Pavement Condition and Traffic Loading Data," *NCHRP Report* 126, pp. 10-31.

ERES Consultants, Inc., (1983), *Technique for Pavement Rehabilitation* – Training Course, Prepared for the U.S. Department of Transportation, Federal Highway Administration, National Highway Institute, Contract No. DOT-FH-11-9580, ERES Consultants, Inc., Champaign, Illinois, pp. II-71-99.

Hardin, B.O., and V.P. Drnevich, (1972), "Shear Modulus and Damping in Soils: Measurement and Parameter Effects," *Journal of the Soil Mechanics and Foundations Division*, ASCE, Vol. 98, No. SM6, pp. 603-24.

Heisey, J.S., K.H. Stokoe, II, and A.H. Meyer, (1982), "Moduli of Pavement Systems from Spectral Analysis of Surface Waves," *Transportation Research Record* 852, Washington, D. C, pp. 22-31.

Johnston, D.H., M.N. Toksöz and A. Timur, (1979), "Attenuation of Seismic Waves in Dry and Saturated Rocks: II. Mechanisms," *Geophysics*, Vol. 44, pp. 691-711.

Kausel, E., (1974), "Forced Vibrations of Circular Foundations on Layered Media," M.I.T. Research Report R74-11, Dept. of Civil Engineering, Massachusetts Institute of Technology, Cambridge, Mass.

Kausel, E., (1981), "An Explicit Solution for the Green Functions for Dynamic Loads in Layered Media," M.I.T. Research Report S81-13, Dept. of Civil Engineering, Massachusetts Institute of Technology, Cambridge, Mass.

Kausel, E., and R. Peek, (1982), "Boundary Integral Method for Stratified Soils," Research Report R82-50, Dept. of Civil Engineering, Massachusetts Institute of Technology, Cambridge, Mass.

Kausel, E., (1988), "Local Transmitting Boundaries," *Journal of Engineering Mechanics*, ASCE, Vol. 114, No. 6.

Lay, M.G., (1986), *Handbook of Road Technology*, Volumes 1 and 2, Gordon and Breach Science Publishers, New York, 712 pp.

Lysmer, J., and G. Waas, (1972), "Shear Waves in Plane Infinite Structures," *Journal of the Engineering Mechanics Division*, ASCE, Vol. 98, No. EM1, pp. 85-105.

Moore, W.M., (1978), "An Introduction to Nondestructive Structural Evaluation of Pavements," *Circular* No. 189, Transportation Research Board, Washington, D. C., pp. 1-33.

Nazarian, S., K.H. Stokoe, II, and W.R. Hudson, (1983), "Use of Spectral Analysis of Surface Waves for Determination of Moduli and Thicknesses of Pavement Systems," *Transportation Research Record*, No. 930, Washington, D. C, pp. 38-45.

Nazarian, S., (1984), "In Situ Determination of Elastic Moduli of Soil Deposits and Pavement Systems by Spectral-Analysis-of-Surface-Waves Method," doctoral dissertation, The University of Texas at Austin.

Nazarian, S., and K.H. Stokoe, II, (1985a), "In Situ Determination of Elastic Moduli of Pavement Systems by Spectral-Analysis-of-Surface-Waves Method (Practical Aspects)," Research No. 368-1F, Center for Transportation Research, The University of Texas at Austin.

Nazarian, S., and K.H. Stokoe, II, (1985b), "In Situ Determination of Elastic Moduli of Pavement Systems by Spectral-Analysis-of-Surface-Waves Method (Theoretical Aspects)," Research No. 437-1, Center for Transportation Research, The University of Texas at Austin.

Richart, F.E., Jr., J.R. Hall, Jr., and R.D. Woods, (1970), *Vibration of Soils and Foundations*, Prentice-Hall, Inc., Englewood Cliffs, New Jersey, 414 pp.

Rix, G.J., (1988), "Experimental Study of Factors Affecting the Spectral-Analysis-of-Surface-Waves Method," doctoral dissertation, The University of Texas at Austin.

Roesset, J.M., and K. Shao, (1986), "Dynamic Interpretation of Dynaflect and Falling Weight Deflectometer Tests," *Transportation Research Record* 1022, pp. 7-16.

Sánchez-Salinero, I., (1987), "Analytical Investigation of Seismic Methods Used For Engineering Applications," doctoral dissertation, The University of Texas at Austin.

Stokoe, K.H., II, and G.J. Rix, (1988), "Use of the Spectral-Analysis-of-Surface-Waves Method to Determine In Situ Shear Wave Velocities at Fucino, Italy," Geotechnical Engineering Center Report GR88-5, The University of Texas at Austin.

Toksöz, M.N., D.H. Johnston, and A. Timur, (1979), "Attenuation of Seismic Waves in Dry and Saturated Rocks: II. Laboratory Measurements," *Geophysics*, Vol. 44, pp. 681-690.

Uddin, W., S. Nazarian, W.R. Hudson, A.H. Meyer, and K.H. Stokoe, II, (1983), "Investigations into Dynaflect Deflections in Relation to Location/Temperature Parameters and In Situ Material Characterization of Rigid Pavements," Research No. 256-5, Center for Transportation Research, The University of Texas at Austin.

Uddin, W., A.H. Meyer, W.R. Hudson, and K.H. Stokoe, II, (1985), "A Structural Evaluation Methodology For Pavements Based on Dynamic Deflection," Center for Transportation Research, The University of Texas at Austin.

Waas, G., (1972), "Linear Two-Dimensional Analysis of Soil Dynamics Problems in Semi-Infinite Layered Media," doctoral dissertation, The University of California at Berkeley, California.

Weaver, W., Jr., and P.R. Johnston, (1984), *Finite Elements for Structural Analysis*, Prentice-Hall, Inc., New Jersey, 403 pp.

Westergaard, H.M., (1926), "Stresses in Concrete Pavements Computed by Theoretical Analysis," *Public Roads*, Vol. 7, No. 2, pp. 25-35.

Zienkiewicz, O.C., (1977), *The Finite Element Method*, 3rd ed., McGraw-Hill Book Company, New York, 787 pp.